March 2019

Assessment and Correction of Lidar-derived DEMs in the Coastal Marshes of Louisiana

William M. Lauve
Louisiana State University and Agricultural and Mechanical College, wlauve1@lsu.edu

ASSESSMENT AND CORRECTION OF LIDAR-DERIVED DEMS IN THE COASTAL MARSHES OF LOUISIANA

A Thesis
Submitted to the Gradate Faculty of the
Louisiana State University and
Agricultural and Mechanical College
in partial fulfillment of the
requirements for the degree of
Master of Science

in

The Interdepartmental Program in Coastal and Ecological Engineering

by
William Lauve
B.S., Louisiana State University
May 2019

Acknowledgements

Firstly, I would like to thank Dr. Scott Hagen for providing me with this assistantship and making this opportunity possible. His patience, generosity and high standard have helped me grow personally as well as professionally and have pushed me further than I could have imagined. For a summer, he provided funds for me to explore and expand my research in Australia, a life changing experience. For all these things I am greatly indebted to him.

I would like to thank Dr. Foster-Martinez for dragging me to the finish line. Her positivity, wit and friendship has challenged me on multiple levels and without her influence and help this research would not have been possible.

I would also like to thank Dr. Karim Alizad for teaching me valuable skills and introducing me to RTK and field work. His kindness and patience was much appreciated during my first two years of my master's program, something I will never forget. Thankyou.

I am thankful for my sister, Katie, who helped me jumpstart this quest for a master's degree. Throughout this process she's listened to my triumphs and dark days with equal intensity. She is the light that led me to and out of the tunnel. I love you.

I would like to thank my colleagues, friends and fellow research team members for being my community away from home. I wouldn't be where I am without yall. Also, shout out to Cody J. for challenging me with ideas and sharing knowledge for the good of science. The willingness to help another is a most valued attribute and is present at LSU.

Finally, I would like to thank my parents, Susan and Lewis, for their love, support and encouragement to follow my passion. Thank you to my brother and all the family that resides on the hill for being the joy we all long for. Thank you to my grandparents for being the best friends

and role models a person will ever know by constantly demonstrating compassion for the ones around them. Love all of you. Peace.

TABLE OF CONTENTS

ACKNOWLEDGEMENTS II

LIST OF TABLES VI

LIST OF FIGURES IX

ABSTRACT XIV

1. INTRODUCTION 1
   1.1. OVERVIEW AND MOTIVATION 1
   1.2. RESEARCH OBJECTIVES 3

2. REVIEW OF ELEVATION MEASUREMENTS 5
   2.1. GLOBAL POSITIONING SYSTEM AND REAL TIME KINEMATIC 5
   2.2. LIGHT DETECTING AND RANGING 9

3. DIGITAL ELEVATION MODEL CORRECTION OVERVIEW 21
   3.1. INTRODUCTION 21
   3.2. MINIMUM BINNING 21
   3.3. VEGETATIVE CORRECTION FACTORS 22
   3.4. BIOMASS MODEL 23
   3.5. STATISTICAL CORRECTION 24

4. METHODS 25
   4.1. STUDY AREAS 25
   4.2. IN-SITU DATA 32
   4.3. REMOTE DATA 35
   4.4. DATA ORGANIZATION AND ANALYZATION 41

5. RESULTS 44
   5.1. BIG BRANCH MARSH NATIONAL WILDLIFE REFUGE 44
   5.2. ELMER'S ISLAND 48
   5.3. COCODRIE, LA SURVEY 56
   5.4. PEARL RIVER, LA SURVEY 60

6. DIGITAL ELEVATION MODEL CORRECTION 66
   6.1. OPTIMAL MINIMUM BINNING 66
   6.2. LIDAR ADJUSTMENT USING NDVI 75
   6.3. RANDOM FOREST ERROR PREDICTION MODEL 86

7. DISCUSSION AND RECOMMENDATIONS 92
   7.1. ECOLOGICAL INFLUENCES OF ERROR 92
   7.2. ECOLOGICAL LIMITATION OF ERROR SOLUTIONS 96
   7.3. MODEL PERFORMANCE 99
   7.4. MODEL IMPLICATIONS 101
   7.5. RECOMMENDATIONS 105

8. CONCLUSION 106

VITA.....114

List of Tables

Table 2.1. Summary of lidar error in coastal marshes by author, location, and lidar acquisition details. 18

Table 5.1. Summary of the error found at the Big Branch survey area, calculated as mean error (ME), mean absolute error (MAE) and root mean square error (RMSE). 45

Table 5.2 Summary of the error found at the Elmer's Island survey area, error statistics calculated as mean error (ME), mean absolute error (MAE) and root mean square error (RMSE). 50

Table 5.3. Summary of the error found at the Elmer's Island in the CPRA survey area, calculated as mean error (ME), mean absolute error (MAE) and root mean square error (RMSE). 54

Table 5.4. Summary of the error found at the Elmer's Island survey area by land cover class. Error statistics are calculated as mean error (ME), mean absolute error (MAE) and root mean square error (RMSE). Mean RTK elevation calculated within each individual class. 55

Table 5.5. Summary of the error found at the Cocodrie, LA Island survey area, calculated as mean error (ME), mean absolute error (MAE) and root mean square error (RMSE). 57

Table 5.6. Summary of the error found at the Pearl River, La Island survey. Error statistics are calculated as mean error (ME), mean absolute error (MAE) and root mean square error (RMSE). 61

Table 6.1. Error statistics of the minimum binning derived DEMs at Big Branch, calculated as mean absolute error (MAE), mean error (ME) and root mean square error (RMSE). The optimal bin size is highlighted in red. 67

Table 6.2. Error statistics of the minimum binning derived DEMs at Elmer's Island, LA, calculated as mean absolute error (MAE), mean error (ME) and root mean square error (RMSE). The optimal bin size is highlighted in red. 69

Table 6.3. Error statistics of the minimum binning derived DEMs at Pearl River, LA calculated as mean absolute error (MAE), mean error (ME) and root mean square error (RMSE). The optimal bin size is highlighted in red. 71

Table 6.4. Error statistics of the minimum binning derived DEMs at Cocodrie, LA calculated as mean absolute error (MAE), mean error (ME) and root mean square error (RMSE). The optimal bin size is highlighted in red. 72

Table 6.5. A regression summary of the LEAN model. The independent variables are labeled as coefficients with corresponding estimates, standard error, t value, and the probability of finding any value larger or smaller than t. 76

Table 6.6. Overall error statistics of the new DEM at the CPRA RTK survey area. Statistics calculated as mean error (ME), mean absolute error (MAE) and root mean square error (RMSE). 78

Table 6.7. Errors statistics based on the classes distinguished by the NAIP imagery, calculated as mean error (ME), mean absolute error (MAE) and root mean square error (RMSE). The percent improvement for each statistic of each class is highlighted in red. 79

Table 6.8. A regression summary of the LEAN model. The independent variables are labeled as coefficients with corresponding estimates, standard error, t value, and the probability of finding any value larger or smaller than t. 80

Table 6.9. Overall error statistics of the new DEM at the two southern grids located at the Big Branch survey area. Statistics calculated as mean error (ME), mean absolute error (MAE) and root 82

Table 6.10. A regression summary of the 2017 LEAN model at Pearl River, LA. The independent variables are labeled as coefficients with corresponding estimates, standard error, t. 84

Table 6.11. A regression summary of the 2017 LEAN model at Cocodrie, LA. The independent variables are labeled as coefficients with corresponding estimates, standard error, t value, and the probability of finding any value larger or smaller than t. 85

Table 6.12. A list of independent variables used in a random forest model build at Elmer's Island survey 1. The performance of the build is based on the mean square error (MSE) and the percentage of.....87

Table 6.13. Errors statistics based on the classes distinguished by the NAIP imagery, calculated as mean error (ME), mean absolute error (MAE) and root mean square error (RMSE).....88

Table 6.14. A list of independent variables used in a random forest model build at Big Branch's north survey grid. The performance of the build is based on the mean square error (MSE) and the percentage 89

Table 6.15. Overall error statistics of the new DEM at the two southern grids located at the Big Branch survey area using random forest model #6. Statistics are calculated as mean error (ME),.....90

Table 6.16. A comparison of the LEAN method and optimal random forest (RF) model extrapolated to the CPRA RTK survey area. The statistics are broken down by the cover classes. The percent improve for each statistics is colored red. 91

Table 7.1. Summary of the statistics and improvements of different methods at the survey sites. * Indicates model was trained and tested with the exact same dataset. 99

List of Figures

Figure 2.1. A schematic demonstrating the intersection of spheres. The gray represents the plane of intersection for two spheres. Two black dots are the solutions when a third sphere is introduced. (Kaplan & Hegarty, 2005) 6

Figure 2.2. The cross-track scan view of typical lidar scanners. The footprint of the lidar beam can also be seen as it impacts the ground. (Shan & Toth, 2018) 10

Figure 2.3. Plot of the return pulses by power and time. The first, second and last return of discrete lidar can be seen in the last column. (Shan & Toth, 2018) 11

Figure 2.4. Plot of estimated vertical (z) and horizontal (xy) accuracy at one standard deviation with respect to flying height for multi pulse in air (MPiA) and single pulse in air (SPiA). 13

Figure 2.5. Schematic waveforms depicting returns from (a) highly reflective flat ground, (b) less reflective flat ground, (c) flat ground with low vegetation cover such as tall gras 17

Figure 4.1. Map of coastal Louisiana showing the four RTK survey locations: Big Branch Marsh Wildlife Refuge, Pearl River, Cocodrie, and Elmer's Island. Base map source: Esri's DigitalGlobe Geoeye Earthstar Geographics. 25

Figure 4.2. Imagery of the Cocodrie survey area. Multiple survey grids can be seen in (A) and the individual RTK survey points are in green. Map of coastal of Louisiana showing RTK location (B). Figure (A) is the portion of Figure (B) contained in the orange box. 26

Figure 4.3. Imagery of the Elmer's Island survey area. The survey grids can be seen in (A) and the individual RTK points are colored green. Map of coastal of Louisiana showing RTK location (B). Figure (A) is the portion of Figure (B) contained in the orange box. 28

Figure 4.4. Imagery of the Pearl River survey area. The survey grids can be seen in (A) and the individual RTK points are colored 29

Figure 4.5. Seasonal salinity (blue) of CRMS station 3784 from January 2011 to December 2018. The average salinity during the growing season is plotted in green. 30

Figure 4.6. Images of the Big Branch survey area. The survey grids can be seen in (A) and the individual RTK points are colored green. Map o 31

Figure 4.7. RTK survey at Big Branch survey site. Photo: M. Foster-Martinez 34

Figure 4.8. Schematic of the Dark Object Subtraction technique performed on the NAIP imagery. 39

Figure 5.1. RTK elevation (A) and error (B) visualization of the Big Branch RTK survey. Error is calculated by subtracting the RTK el 44

Figure 5.2. Plot showing DEM error (m) versus measured RTK elevation at Big Branch (most northern grid (Figure 5-1A), fitted with a linear least squares (LLS) trend line and sloped 1:-1 line (green). 46

Figure 5.3. DEM error (m) versus NAIP NDVI at Big Branch, fitted with a linear least squares (LLS) trend line. 47

Figure 5.4. NAIP 2017 NDVI versus measured RTK elevation (m, NAVD88) at Big Branch, fitted with a linear least squares (LLS) trend line. 48

Figure 5.5. Visualization of RTK elevation (m) (A) and DEM error (B) at Elmer's Island survey 1. Color codes distinguish six natural breaks in the data. 49

Figure 5.6. Plot showing DEM error (m) versus NAIP NDVI at the Elmer's Island survey, fitted with a linear least squares (LLS) trend line. 50

Figure 5.7. NAIP 2013 NDVI versus measured RTK elevation (m NAVD88) at Elmer's Island, fitted with a linear least squares (LLS) trend line for all points. Points are color coded based on the range of error associated with the RTK point. 51

Figure 5.8. Plot showing DEM error (m) versus measured RTK elevation at Elmer's Island, fitted with a linear least squares (LLS) trend line. 52

Figure 5.9. RTK elevation (A) and error (B) visualization of a part of the 2017 CPRA RTK survey at Elmer's Island. Error is calculated by subtracting the RTK elevation value from the DEM. Color codes distinguish seven natural breaks in the data. 53

Figure 5.10. A 10 class land cover classification map of the 2017 CPRA RTK survey area. The marsh and mangrove classes are associated with classes 1, 2, 3, 5 and 8. 55

Figure 5.11. RTK elevation (A) and error (B) visualization of the 2017 RTK survey near Cocodrie, La. Error is calculated by subtracting the RTK elevation value from the DEM (2015 USGS: LA South Terrebonne, LA). Color codes distinguish six natural breaks in the data....57

Figure 5.12. DEM error (m) versus 2011 and 2015 NAIP NDVI at the Cocodrie, LA survey site, fitted with a linear least squares (LLS) trend line. 58

Figure 5.13. DEM error (m) versus measured 2015 RTK elevation at Cocodrie, La. Data is fitted with a linear least squares (LLS) trend line. 59

Figure 5.14. Plot showing 2015 DEM error (m) versus 2015 NAIP NDVI at the Cocodrie, La survey, fitted with a linear least squares (LLS) trend line.....60

Figure 5.15. RTK elevation (left) and error (right) visualization of the 2018 RTK survey near Pearl River, La. Error is calculated by subtracting the RTK elevation value from the DEM. Color codes distinguish six natural breaks in the data. 61

Figure 5.16. Scatter plot showing DEM error (m) at the Pearl River, La survey area versus 2016 NAIP NDVI. Data is fitted with a linear least squares (LLS) trend line. 62

Figure 5.17. Scatter plot showing DEM error (m) at the Pearl River, La survey area versus 2017 NAIP NDVI. Data is fitted with a linear least squares (LLS) trend line. 63

Figure 5.18. Scatter plot demonstrating the relation between 2016 NAIP NDVI (m) and measured RTK elevation (m) referencing NAVD 88 at the Pearl River survey site. Data is fitted with a linear least squares (LLS) trend line.....64

Figure 5.19. Scatter plot showing DEM error (m) versus measured RTK elevation at Pearl River, La. Data is fitted with a linear least squares (LLS) trend line. 65

Figure 6.1. Box and whiskers plots of error at Big Branch when deriving the DEM using the minimum binning technique at resolutions of 68

Figure 6.2. Box and whiskers plots of error at Elmer's Island when deriving the DEM using the minimum binning technique at resolutions of 2.5, 5.0, 7.0, and 10 m. The box represents the 25^{t}.....69

Figure 6.3. Box and whiskers plots of error at Pearl River, LA when deriving the DEM using the minimum binning technique at resolutions of 2.5, 5.0, 7.0, and 10 m. The box represents the 25th, 5.....71

Figure 6.4. Box and whiskers plots of error at Pearl River, LA when deriving the DEM using the minimum binning technique at resolutions of 2.5, 5.0, 7.0, and 10 m. The box represents the 25th, 50th a 73

Figure 6.5. Error histograms of the unadjusted DEMs at the Cocodrie, LA, Elmer's, LA, Pearl River, LA and Big Branch survey sites. 74

Figure 6.6. Error histograms of the optimal minimum binning DEMs at the Cocodrie, LA, Elmer's, LA, Pearl River, LA and Big Branch, LA survey sites. 75

Figure 6.7. Plot of the original DEM and New DEM vs RTK values. The New DEM is the theoretical DEM produced by the correction method. A 1:1 line is indicated in black. 77

Figure 6.8. Plot of the original DEM and New DEM vs RTK values at the CPRA survey site. A 1:1 line is indicated in black. 78

Figure 6.9. Plot of the original DEM and New DEM vs RTK values for Big Branch. A 1:1 line is indicated in black. 81

Figure 6.10. Plot of the original DEM and New DEM vs RTK values at the two southern grids located at Big Branch survey site. A 1:1 line is indicated in black. 82

Figure 6.11. Plot of the original DEM and new 2016 derived DEM vs RTK values for Pearl River, LA. A 1:1 line is indicated in black. 83

Figure 6.12. Plot of the original DEM and new 2017 derived DEM vs RTK values for Pearl River, LA. A 1:1 line is indicated in black. 84

Figure 6.13. Plot of the original DEM and new derived DEM vs RTK values for Cocodrie, LA. A 1:1 line is indicated in black. 86

Figure 7.1. Image of dense matted Spartina patens approximately 15-20 cm above the ground surface at the Big Branch site. Photo: M. Foster-Martinez 94

Figure 7.2. 2015(A) and 2017 (B) NAIP images of the Big Branch survey area. Both images were photographed in September. 98

Abstract

The onset of airborne light detection and ranging (lidar) has resulted in expansive, precise digital elevation models (DEMs). DEMs are essential for modeling complex systems, such as the coastal land margin of Louisiana. They are used for many applications (*e.g.* tide, storm surge, and ecological modeling) and by diverse groups (*e.g.* state and federal agencies, NGOs, and academia). However, in a marsh environment, it is difficult for airborne lidar to produce accurate bare-earth measurements and even accurate elevations are rarely verified by ground truth data. The accuracy of lidar in marshes is limited by the sensor's resolution and by the laser's ability to penetrate dense vegetation. The first objective of this work is to measure elevation using Real Time Kinematic (RTK) instruments and compare them to elevations from lidar-derived DEMs. This error evaluation ($elevation_{DEM} - elevation_{RTK} = error$) will be performed in a variety of marsh types with differing vegetation. This evaluation shows that the surveyed marshes produce minimal DEM error in relation to other published work but are still likely to result in misleading hydrodynamic and wetland modeling outcomes. The second objective is to correct lidar-derived DEMs by applying and improving upon previously published methods. The techniques will be improved through the use of additional remote sensing inputs and by understanding the ecological factors that influence the spatial and temporal distribution, composition and productivity of marsh plant species.

1. Introduction

1.1. Overview and Motivation

Due to anthropogenically-derived greenhouse emissions, the level of atmospheric carbon dioxide has not been beyond the level of the mid-20th and 21st centuries (post 400,00 years ago) and is considered the most significant source of rapid climate change (Wuebbles, Fahey, & Hibbard, 2017). The evidence of this change is compelling: global temperature rise, warming oceans, shrinking ice sheets, glacial retreat, ocean acidification, decreased snow cover and sea level rise. This associated sea level rise has commenced a variety of worldwide coastal landscape responses that will continue throughout the 21st century (Mengel, Nauels, Rogelj, & Schleussner, 2018). In low-gradient coastal landscapes, major changes include: the increased inundation of wetlands, increased shoreline erosion, and increased flooding during storm events (Passeri et al., 2015). In fact, the Louisiana coastline undergoes the highest rates of relative sea level rise (i.e. subsidence plus sea level rise) and land loss in North America (Couvillion et al., 2011; Penland & Ramsey, 1990). Major landscape changes threaten the fisheries, coastal communities and industry and have caused engineers and ecologists to find solutions. In the last 30 years, geomorphologic, hydrodynamic, storm surge and ecological models have been developed to efficiently investigate and mitigate coastal changes.

Arguably the most critical input for these models is the bare earth elevation. Relative elevation controls the abiotic features of marshes such as: accretion rates (Butzeck et al., 2015; Morris et al., 2016), soil characteristics (Cahoon & Reed, 1995), pore water salinity and oxygen availability (Hackney et al., 1996). From a hydrodynamic point of view, coastal landforms influence water circulation patterns, sediment transport, the size of tidal prisms, and the

propagation and attenuation of storm surge and wind driven waves (Passeri et al., 2015). All of these factors determine the evolution and sustainability of marshes and affect the magnitude of ecosystem services certain coastal systems can provide. In this sense, the interrelationships between physics and biology are what shape the coastal landscape, generate intrinsic value, and decide if engineering solutions are cost effective (Zedler & Kercher, 2005). Therefore, the spatial distribution of relative elevation is an essential component that will dictate the outcomes of coastal evolution during this new age of climate change.

The importance of elevation is not exclusive to sea level rise or coastal modeling but has historically impacted many other areas of study. The most commonly used forms of elevation data are digital elevation models (DEMs). DEMs are currently used in variety of different fields and a suite of applications, ranging from precision farming and archaeology to flight simulation and terrain analysis. One of the most common uses of DEMs is the modeling of water flow for hydrology and hydrodynamics. Due to improvements in computation efficiencies, robust, high resolution models can be achieved for expansive areas, creating a powerful tool. In the last two decades, light detecting and ranging (lidar) has become the main source of DEM generation. The benefit of this technology is it can provide sub-meter resolution of large areas with relative ease, at vertical accuracies of less than 0.05 m in opportune circumstances. However, in coastal marshes, the accuracy of bare earth elevations is challenged leading to inaccurate DEMs. It has been shown that a mean positive bias exists between lidar-derived DEMs and ground surfaces, and multiple methods have been proposed and implemented to increase the accuracy of lidar-derived DEMs. Considering nearly 1,500,000 hectares of marsh covers the Louisiana coast (C. Sasser, Visser, Mouton, Linscombe, & Hartley, 2014), expansive modeling errors are likely.

Previous work shows that systematic error in the DEM can and must be reduced to achieve accurate modeling results.

1.2. Research Objectives

The goal of this research is to assess and correct lidar-derived DEMs of the coastal marshes of Louisiana. This goal has been accomplished by determining the DEM error in a variety of marsh types, identifying correlations between DEM error and remote sensing parameters, and applying three correction techniques: minimum binning, described in section 3.2; lidar elevation adjustment with normalized difference vegetative index (NDVI) or (LEAN), described in section 3.5; and a random forest model consisting of imagery and lidar metrics, described in section 6.3. Specifically the following research questions are addressed:

- What is the error in lidar-derived DEMs of coastal marshes in Louisiana?
- What is the optimal minimum binning resolution for each marsh type?
- Can the LEAN method reduce error in all marsh types?
- Can the LEAN method in concert with a National Agriculture Imagery Program (NAIP) image classification scheme further reduce error in an intermediate and saline marsh?
- Will the use of lidar-derived metrics help reduce the error in an intermediate marsh?
- How does a random forest correction model perform compared to a linear regression correction model?
- What are the limitations of previously published corrections in the marshes of Louisiana?

This thesis contains eight chapters. Chapter 1 provides a general overview of the research motivation and objectives. Chapter 2 presents a literature review of the technology and associated accuracies of relevant elevation measurements. Chapter 3 gives a review of the previously published correction techniques. Chapter 4 describes the methodology of the study and details regarding the independent data used for correction. Results from the Real Time Kinematic Global Positioning System (RTK-GPS) survey and associated DEM errors, as well as the relationships between the survey data and independent parameters, are presented in Chapter 5. Chapter 6 includes the three DEM correction techniques and the associated improvements of the DEM. Chapter 7 interprets the sources and patterns of error, justifies correction model results and details the significance of the correction. Chapter 8 highlights the knowledge gained from this work and discusses possible future work.

2. Review of Elevation Measurements

This project relies on the relative accuracy of elevation measurements performed by both RTK-GPS and airborne lidar. It is important that the data produced by these two methods are comparable. This chapter will give an overview of these methods and their associated accuracies and will show that these two types of measurements are closely linked.

2.1. Global Positioning System and Real Time Kinematic

The marshes of Louisiana are usually a remote, harsh environment that disfavors typical surveying methods. Methods, such as leveling, are time consuming, and the equipment is not particularly mobile. Favorably, the invention of RTK-GPS devices has made surveying more efficient and precise; accurate elevation data can be captured with less effort. In this work, Trimble R8 receivers are used in conjunction with the Continuously Operating Reference Stations (CORS) to calculate position with centimeter-level accuracy in the coastal marshes of Louisiana via Real Time Kinematic (RTK). This procedure is described in 4.2.1.

2.1.1. Global Positioning System

Global Positioning Systems (GPS) or more broadly Global Navigation Satellite System (GNSS) started in the 1960's as a military instrument and has become an indispensable tool in the civilian world (Ogaja, 2011). Present day GPS technology has advanced resulting in higher accuracies, but it is still based on the same simple principles. In theory, using satellites to determine position requires four things: an accurate time piece, a sensor to detect incoming signals, a map showing the locations of communicating satellites, and the knowledge of the speed of a signal (Kaplan & Hegarty, 2005). This concept is known as Time of Arrival (TOA). By knowing the location of multiple emitters and the propagation time of an emitted signal, a

receiver location can be found by the mathematical process of trilateration (Ogaja, 2011). While this calculation is simple, errors arise due to the uncertainty of these four required variables. The next sections will discuss the basic process of three-dimensional position location via the intersection of multiple spheres, the errors, and improvements used to reduce this uncertainty.

2.1.1.1. Determining Location

Using the concept of TOA, three dimensional position can be found with the use of

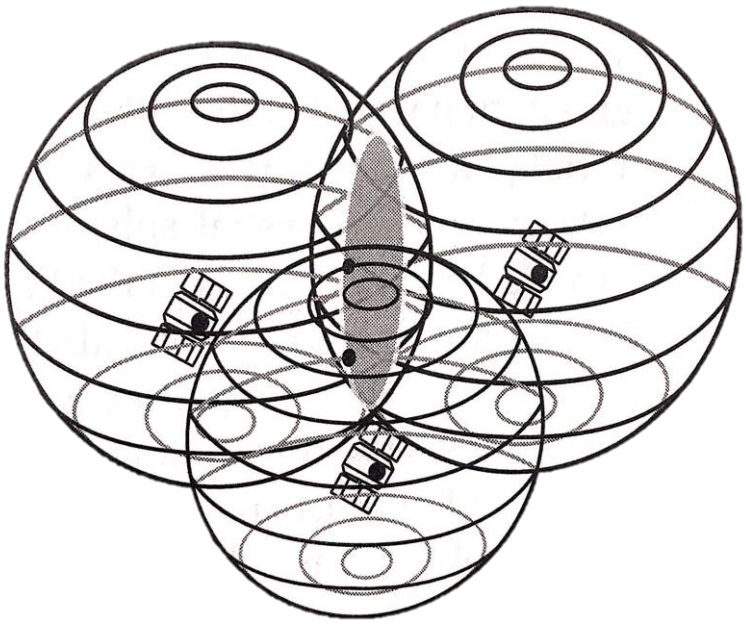

Figure 2.1. A schematic demonstrating the intersection of spheres. The gray represents the plane of intersection for two spheres. Two black dots are the solutions when a third sphere is introduced. (Kaplan & Hegarty, 2005)

satellite ranging signals. The ranging signals are controlled by an internal clock that are ideally in synchronization with the other satellites in the constellation. This is known as GPS system time. Timing information is embedded within the ranging signals, which allows a receiver to calculate the moment in time the signal left the satellite. Time elapsed is calculated from the differential in time (received minus emitted). Using the speed of the signal, which is an electromagnetic wave,

a range can be determined. However, one satellite does not shed enough information to determine an exact location but only produces a sphere in which the receiver location may be (Figure 2.1). At least four satellites must be used to determine a three dimensional position. Using two spheres a three-dimensional area is the solution (gray shaded area in Figure 2.1). When a third sphere is introduced, the solution goes from being a three-dimensional space to two discrete points. Without additional knowledge, the incorrect location may be assumed. Introducing a fourth sphere eliminates the additional solution yielding the exact location.

In the previous explanation, the calculated range is exact, and a level was of uncertainty is not included in the ranging calculation. In actuality each independent measurement is subjected to some type of error. Instead of having a calculated position located on the edge of sphere, an extra radii of uncertainty is added; this means each sphere is not completely defined. When combining all four measurements and performing the trilateration calculation, a three-dimensional zone is produced in which a receiver position could be. This ranging uncertainty has been reduced with advancements in technology and using clever methods to estimate error in the ranging (section 2.1.1.2).

2.1.1.2. GPS with a base station

There are a number of sources that lead to error in GPS measurements: satellite clock error, ephemeris error, relativistic effects, receiver noise, multipath effects and hardware bias. Most of which obscure the range calculation used for position. According to (Datta-Barua, Doherty, Delay, Dehel, & Klobuchar, 2003), the largest source error is from ionospheric delays which can be up to 5 meters. Introduction of carrier phase signals, such as L1C and L2C, have been used to mitigate these errors (Coco, Coker, Dahlke, & Clynch, 1991). Another clever technique to reduce error is the use of a base station. These are advantageous for adjusting the

tropospheric delay (Vollath, Buecherl, Landau, Pagels, & Wagner, 2000). The troposphere consists of the atmosphere that is closest to the Earth and tends to bend the signal due to its high refraction index (Kursinski, Hajj, Schofield, Linfield, & Hardy, 1997). These atmospheric conditions are very similar locally; therefore, the base station and the differential GPS receiver are experiencing very similar delays. The base station provides the offset it is experiencing to the GPS device. However, corrections are less accurate with increasing distance from the base station (Kim Sun & Gibbings, 2005).

The introduction of base station networks such as the Continuously Operating Reference Stations (CORS) can provide an even higher levels of accuracy. Trimble developed a method of RTK surveying called Virtual Reference Station (VRS). This concept utilizes a network of correction information and calculates corrections as if a base station is located near the RTK device (Ogaja, 2011). Since the accuracy of corrections are not as limited by the distance to the real base station, expansive areas can be surveyed with high accuracy as long as the surveyor remains in the network.

One of the main advantages of RTK from a surveying perspective is the ease in which the user can locate a predefined point. Unlike typical GPS, that uses post processed information to correct the measurement, RTK offers and even more efficient form. The correction can be applied in real time, and therefore, predefined points can be navigated to with high accuracy. For example, the accuracy of the Trimble R8 using the RTK network is plus or minus 1.5 cm vertically and plus or minus 0.8 cm horizontally at the 68^{th} percent confidence level (Trimble, 2013). Fortunately, the Louisiana coastline is populated by CORS, which creates an extensive coverage of correction data for determining positions even in remote marshes. However, clear communications with the correction server is not always possible due to the lack of internet

coverage. Radio waves and microwaves have been known to reflect off the marsh canopy resulting in multipath errors. Also, the humidity usually present in coastal areas can cause delays in the radio signal that the base stations are not experiencing, producing another level of uncertainty.

2.2. Light detecting and ranging

Light detecting and ranging (lidar), is an active remote sensing method that uses intense focused beams of light to produce three dimensional characterizations of a surface (Carter et al., 2012). Using infrared pulses to collect high density ranging data, lidar can be used as source data in the creation of digital elevation models (DEMs). In recent years, this has become the standard for DEM generation and is used for a suite of applications: inundation, storm surge, hydrodynamic and morphologic modeling (Liu, 2008). However, unfavorable issues arrise when using airborne lidar for DEM generation in the coastal enviroment. In principle, lidar is a system that uses TOA to determine ranging information of a targeted surface. The fundamental measurement is the amount of time elapsed from the emittance of a laser pulse to the time of return of the same pulse (Lefsky, Cohen, Parker, & Harding, 2002). Using this timing and multiplying by the speed of light, a round trip distance can be determined. Dividing this number by two produces a distance to a targeted surface. Lidar instruments can perform these measurments at rates of 150,000 pules per second, generating a dense network of precise georeferenced elevation data known as a point cloud (Carter et al., 2012). Even though this process may appear straighforward, it is complicated by both the mode of the altimetry measurement and the surface of the intended target area.

2.2.1. Airborne light detecting and ranging

Airborne lidar is a system that uses a laser scanner unit, a Global Positioning System (GPS) and an Inertial Measuring Unit (IMU) to measure three-dimensional positions of surfaces from an elevated, dynamic point of view. Many different types of airborne laser scanners exist inlcuding: single pulse, multi pulse, full waveform, multispectral and single photon scanners. The common ones used for DEM generation and vegetative studies are discrete, waveform and mutlispectal lidar (Lohani & Ghosh, 2017). Pulse laser scanners emit an amplified pulse of light at wavelengths of 0.8 to 1.6 µm. Topographic lidar uses wavlengths in the near infrared spectrum (~1045 nm) which are reflected by terrestrial objects, and bathymetic lidar applies wavelengths

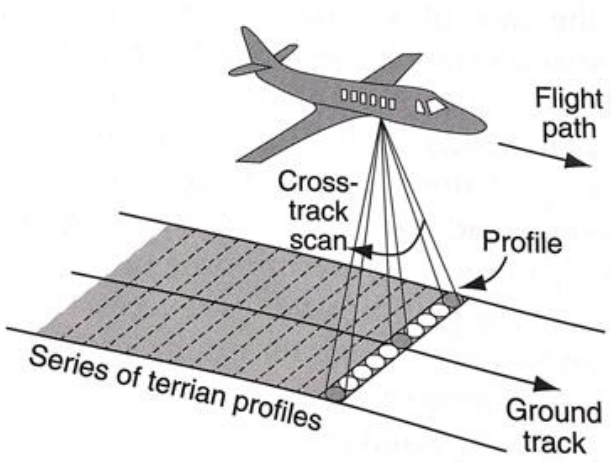

Figure 2.2. The cross-track scan view of typical lidar scanners. The footprint of the lidar beam can also be seen as it impacts the ground. (Shan & Toth, 2018)

in the green spectrum due to its ability to penetrate water (Campbell, 1996). Most laser scanner units use a mirror to direct and redirect the laser pulses beneath the aircraft creating an image swath. The field of view (FOV) depends on the scan angle and altitude of the airplane. A typcial cross-track scanning view can be seen in Figure 2.2 but others are commonly used, such as linear scanner (sinusoidal patterns), rotatating polygon mirrors (curved parrellel lines), palmer scanner and a fiber scanners. For all scanner types, due to beam divulgence from the laser to the intended

surface, the footprint of the beam at a flying height of 1000 m can be the size of 30-50 cm. (Shan & Toth, 2018).

2.2.1.1. Discrete Returns

Unlike other lidar methods, discrete return identifies specifc peaks in the power of the pulse return (Shan & Toth, 2018). On reflection of the laser pulse various amounts of energy make it to the sensor at different times. Once an energy peak is identified, a constant fraction dicriminator (typically around 50%) is used to determine the return time of the pulse. This location is usually defined as the leading edge of the full-width at the half maximum (FWHM), as seen in Figure 2.3. If the waveform is highly seperable, multiple returns can be recorded. The pulsewidth for most discrete lidar during the 2000s was approximatley 7 ns.

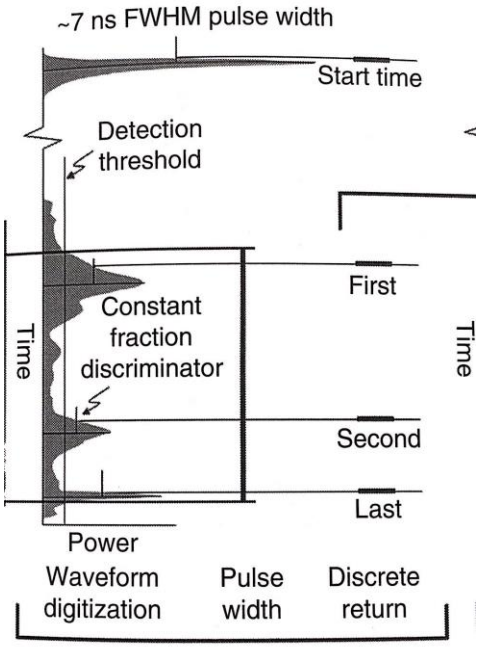

Figure 2.3. Plot of the return pulses by power and time. The first, second and last return of discrete lidar can be seen in the last column. (Shan & Toth, 2018)

2.2.1.2. Accuracy Improvements

The positional accuracy of airborne lidar depends on three components: the IMU, GPS and the lidar sensor. Before 2007, most of the inaccuracy of airborne lidar was due to the GPS, which independently produced an accuracy of 5 cm horizontally and 10 cm vertically (Liu, 2008). At that time, the inertial measuring unit (IMU), which meaures the attitude, roll, pitch and heading of the platform, had an accuracy of a few centimeters (Webster & Dias, 2006) and the lidar sensor was as accurate as 2-3 cm (Lemmens, 2007). Combining all of these components airborne lidar can yield accuracies of 15 cm root mean square error (RSME) vertically and 20 cm RMSE horizontally (CARMS, 2006). However, in the last 10 years lidar technology has seen a noticeable increase in these accuracies. 2017 USGS lidar (Riegl LMS-Q680i laser via polygonal mirror) has provided vertical accuracies with RMSE and fundamental vertical accuracy (FVA) values of 4.9 cm and 9.7 cm respectivley. Since 2011, vertical accurcies have improved by 30%, and horizontal accurcies have improved by 71%, comparing 2011 and 2017 USGS lidar metatdata. This improvement is in part due to lower flying altitudes (smaller footprint size), increasing the density of the pulse fequencies (nominal point spacing) and increases in GPS accuracies, which can now be less than 2 cm (Lohani & Ghosh, 2017). The errors in the laser scanning can come from individual sensor calibration (~50 mm), lack of synchronization, and misalingment between the sensors (Shan & Toth, 2018). Miscalibrations such as bore-site offset, bore-sighting anglar bias and laser beam angular bias cause errors to increase with increased elevation and increased look angle. This means the relative accuracy of lidar can be spatially dependent and improves with decreases in flying altitude (Figure 2.4). The graph shows that single pulse is overall more accurate than multi pulse and that lower altitudes produce better lidar

accuracies. The spatial variability of accuracies in the vegetative realm are further discussed in section 2.2.1.3 and 2.2.1.3.1.

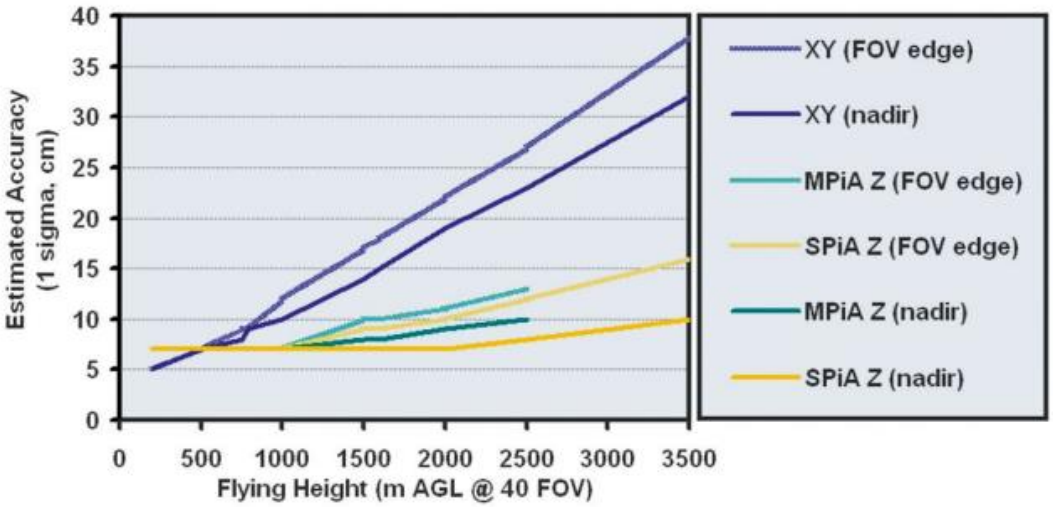

Figure 2.4. Plot of estimated vertical (z) and horizontal (xy) accuracy at one standard deviation with respect to flying height for multi pulse in air (MPiA) and single pulse in air (SPiA) for the Leica ALS70 airborne lidar scanner. Nadir represents a scan angle of 0 degrees and field of view (FOV) edge refers to highest viewing angle. Based on a nominal GNSS error of 5 cm (Geosystems, 2011).

Another important aspect of lidar is the vertical discrimination, which refers to the ability to separate vertical features of individual pulse peaks for multiple returns. The pulse width of many discrete-return lidar systems is approximately 7 ns (Shan & Toth, 2018) which corresponds to a distance of 2.12 m. Therefore, it is difficult for most lidar scanners to distinguish returns less than 2.12 meters apart (Schmid, Hadley, & Wijekoon, 2011). Referring to Optech's ALTM 1020, 1210, and 1225 models manufactured from 1993 to 1998, these scanners only had the ability to capture two returns. From 2004 to 2006 Optech introduced the ALTM 3100 and Gemini which could capture four intensity values and four range returns. These newer generation scanners could discriminate returns in the range of 1.5-2.2 m. In 2012 Optech designed the ALTM-Orion which could discrminate vertical features at a smaller scale, approximatley 0.8 m

(Ussyshkin & Theriault, 2011). To put this into perspective, the Leica ALS50 (2003), ALS60 (2008), and ALS70 (2011) have have vertical discriminations of approximatley 3.5 m. The Optech Galaxy leads the industy for minimum target seperation of less than 0.7 m with up to 8 returns per pulse. The only other way to achieve finer resolution is to record the full waveform.

2.2.1.3. Accuracy Assessments

Ground control points (GCPs) usually measured with RTK-GPS are used to test the accuracy of the lidar elevations for a variety of ground cover types. This includes: bare earth, forest, shrub, urban and weeds or crops (Carter et al., 2012). Due to the horizontal uncertainty of lidar, a triangulated irregular network (TIN) is usually generated using the bare earth point cloud. In this case, the interpolated surface of the three lidar points best represents the elevation and is tested against the GCPs. The vertical error is calculated as:

$$Vertical\ Error = Z_{data(i)} - Z_{check(i)} \qquad \text{Eq. 2.1}$$

where $Z_{data(i)}$ is the vertical coordinate of it the i^{th} checkpoint in the dataset; $Z_{check(i)}$ is the vertical coordinate of the i^{th} checkpoint in the independent source of higher accuracy; and i is an integer from 1 to n: $n =$ the number of points being checked (Commitee, 2004).

According to the American Society for Photogrammetry and Remote Sensing (ASPRS), there are three types of errors associated with lidar measurements: blunders, systematic error and random error. Random errors are produced by no known source and cannot be corrected by use of standardized adjustments. This type of error is typically normally distributed. On the other hand, systematic error follows some sort of pattern and in theory is predictable and can be eliminated or reduced. Generally, random error is associated with open terrain, and systematic error is generated by the laser's inability to penetrate vegetation, miscalibrations of equipment or

other misinterpretations of terrain surfaces. Blunders are considered an error of huge proportions. Statistically, any error greater than three times the standard deviation of the RMSE is considered a blunder and should be further analyzed and possibly removed from the dataset.

When reporting accuracies of lidar datasets, the fundamental vertical accuracy (FVA), or non-vegetated accuracies (NVA), and supplemental accurcies are both assessed. FVA represents the error in open terrains with clean surfaces, where there is a high probability that returns have hit the ground. This means FVA and NVA are comparable to other datasets. The other acccuracy assessment is supplemental, or consolidated, vertical accuracies. They represent error in a variety of ground cover types. The supplemental accuracy assessment is highly variable and is not comparable to other datasets due to local variations in ground cover. However in the event that the FVA test cannot be completed due to the lack of open terrain, a supplemental accuracy report must be completed. Both the FVA and supplemental accuracy assessment follow the 95th percentile method. This method evaluates RMSE at the 95th percentile, meaning 95 percent of the error will less than the calculated value and 5 percent above the specified amount (Flood, 2004). It is calculated as follows:

Compute the RMSE:

$$RMSE_z = \sqrt{\frac{\sum(Z_{data(i)} - Z_{check(i)})^2}{n}} \qquad \text{Eq. 2.2}$$

Compute the 95th percentile of accuracy:

$$Accuracy_{(z)} = 1.9600 * RMSE_{(z)} \qquad \text{Eq. 2.3}$$

For this equation to be true, it is expected that the NVA and FVA error assesments are normally distributed because this error should be random. However, the vegetated accuracy (VA) or

supplemental accruacy is less likely to be normally distributed, and Equation 2 may not represent the expected error at the 95th percentile.

2.2.1.3.1. Accuracy in intertidal marshes

Many times lidar DEMs of tidal marsh platforms are mischaracterized as being above the mean high water (MHW), which is infeasible for these systems (Kidwell, Dietrich, Hagen, & Medeiros, 2017). According to (C. Wang et al., 2009), there are three main challenges for the effective use of lidar in the tidal enviroment:

1) Marsh areas are covered by dense vegetation, leading of a relatively low chance of laser penetration through the canopy to the ground.
2) The relatively few ground returns cannot be easily separated from vegetation returns by sampling the return waveform or by using first and last returns because of the low height of the vegetation. As a consequence, the first and last returns of lidar data are practically identical (Figure 2.5c).
3) The inaccuracy introduced by uncertain separation of ground and vegetation returns plus the intrinsic instrument inaccuracies may lead to unacceptably large estimation errors compared with the typically small topographic relief of intertidal marshes.

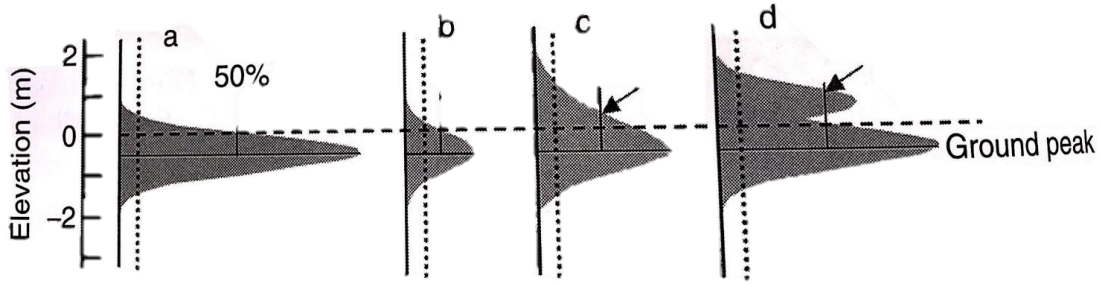

Figure 2.5. Schematic waveforms depicting returns from (a) highly reflective flat ground, (b) less reflective flat ground, (c) flat ground with low vegetation cover such as tall grass, and (d) flat ground with a low but distinct vegetation layer such as a forest under-story. The detection threshold is dotted, leading edge timing for the ground peak using 50% constant fraction discrimination is dashed, and arrows mark the height of upward biased returns for the vegetated areas. (Shan & Toth, 2018)

A summary of documented marsh error can be seen in Table 2.1. J*uncus roemerianus* and tall *Spartina alterniflora* had some of the highest errors. It's hard to justify error trends based on sensor type, flying altitude and point spacing because the vegetation structures and lidar acquisition attributes vary across the studies. The Optech Gemini, the newest lidar system of the group, had some of the lower error values (Hladik 2012).

Table 2.1. Summary of lidar error in coastal marshes by author, location, and lidar acquisition details.

Schmid et al. 2011	RMSE (cm)	Location	Sensor	Altitude (m)	Pt. Spacing (m)
Open Terrain	**9.3**	South Carolina	ALS50	1400	1.4
Navy Base	21.6				
Folly Beach	4.2				
Palmetto Island	25.7				
Sullivan's Island	14.8				
Belle Hall	45.3				
OVERALL	**23.2**				
Species					
S. alterniflora	15.6				
Juncus roemerianus	36.6				
Borrichia frustescens	14.8				
Salicornia virginica	11.5				

Fernandez et al. 2017	RMSE (cm)	Location	Sensor	Altitude (m)	Pt. Spacing (m)
Open Terrain	**4**	Odiel-Tinto Marsh	ALS 50 II	1450	1
Low Marsh	2	Gulf of Cadiz, SW	Multi pulse		
Mid Marsh	8	Spain			
High Marsh	15				
Spartina Marsh	29				
Overall Site 1	**7**				
Overall Site 2	**24**				

Hladik et al. 2012	RMSE (cm)	Location	Sensor	Altitude (m)	Pt. Spacing (m)
Open Terrain	10	Sapelo Island, Georgia	Optech Gemini	800	1
Tall S. alterniflora	31				
Medium S. alternifora	11				
Short S. alterniflora	5				
S. virginica	7				
D. spicata	6				
B. maritima	5				
Salt Pan	4				
J. roemerianus	13				
B. frutescens	15				
Overall	**16**				

NOAA 2011	RMSE (cm)	Location	Sensor	Altitude (m)	Pt. Spacing (m)
Open Terrain	9.21				
Marsh	23.3				

(table cont'd.)

Medieros 2015		RMSE (cm)	Location	Sensor	Altitude (m)	Pt. Spacing (m)
Open Terrain			Apalachicola River Marsh			
Marsh 5-m min		65				

Buffington 2017	Open Terrain	RMSE (cm)	Sensor	Altitude (m)	Pt. Spacing (m)
San Francisco Bay	2.6	14.5	Leica ALS60 MPiA	2000	1
CA State Coastal Conservancy	4.4	28.5	Leica ALS50 Phase II	900	1
DOGAMI	4.8	25.4	Leica ALS60 MPiA	1900	8.6

(table cont'd.)

3. Digital Elevation Model Correction Overview

3.1. Introduction

High frequency lidar beams lack the ability to penetrate the marsh canopy and capture the returns of the bare-earth of the marsh platform. As a result, returns of the canopy and ground surface foliage inaccurately represent bare-earth, resulting in a positive bias of DEMs. DEM error in coastal marshes is typically spatially variable and is dependent on ecological factors (*e.g.* vegetation type). The following studies all show a mean, positive bias exists between lidar-derived DEMs and ground surfaces: Montané & Torres, 2006; Liu, 2008; Schmid et al. 2011; Hladik & Alber, 2012; Medeiros et al., 2015. Multiple methods have been engineered and implemented to successfully minimize this complication, resulting in lower root mean squared error (RMSE) values and a reduction of the positive bias in the DEM. These methods can be organized into four categories: vegetation correction factors (Hladik & Alber, 2012), minimum bin gridding (Schmid et al., 2011), a biomass model (Medeiros et al., 2015) and a statistical correction, otherwise known as Lidar Elevation Adjustment with NDVI (LEAN) (Buffington, Dugger, Thorne, & Takekawa, 2016).

3.2. Minimum Binning

Minimum binning is a simple technique that reduces the error due to the misclassification of bare-earth ground points, which translates to a reduction of DEM error. However, this option is only feasible when the lidar point cloud is available. This technique extracts the lowest lidar elevation value within a user defined window (*i.e.* bin resolution) and assigns that value to the suitable grid cell (Schmid et al., 2011). Error reduction can be seen in studies by NOAA (2011) and (Schmid et al., 2011), which had a RMSE reduction of 10 cm and 8 cm at bin resolutions of

4 m and 6 m, respectively. Note there was a difference in bin resolution for each study. The optimal bin size that reduces the most error is not universal and can depend on the point density of the lidar and on the structure and density of vegetation. In fact, NOAA suggests using a different bin size for different vegetation types, densities, and heights, but this information is not easily obtained. Ideally, the user should determine the optimal size with ground truth data. Furthermore, while this technique is a sufficient way to reduce error, it comes at the cost of resolution. By assigning one lidar return to a larger grid area (*i.e.* the bin resolution), the nominal point spacing of the lidar point cloud is effectively reduced, and the spatial resolution at which the bare-earth can be accurately represented is lowered. Depending on the intended model application and available source data, minimum binning may be a good fit for reducing lidar error.

3.3. Vegetative Correction Factors

Since lidar error is a function of vegetation type and structure, it is logical to individually correct error based on vegetation species. In this process, a mean error for different cover types is determined from ground truth elevations. The mean error is then subtracted from the DEM in areas where the cover type has been identified, producing a corrected DEM. Positive results can be seen from (Hladik & Alber, 2012; McClure, Liu, Hines, & Ferner, 2016) who reduced the RMSE by 6 cm and 11 cm, respectively, and eliminated the mean error (ME) or positive bias. The primary complication for this type of adjustment is mapping the species and defining cover classes. Accurate species mapping can be accomplished in the field as well as through remote sensing (typically supported by in-situ observations). In-situ observations are not only time consuming but also require expertise in vegetation species identification. Since vegetative characteristics are a function of edaphic factors it is very unlikely one species can be uniformly

correct with one adjustment. In the work by Hladik and Alber (2012), they found it necessary to use three different height classes for one species, *Spartina alterniflora*, to achieve an accurate elevation adjustment. Meaning even within a defined species, associated error can be spatially dependent because the structure and productivity of the species is also spatially dependent. Further error can be introduced by the misclassification of species. In the work by (McClure et al., 2016) there was an inability to differentiate certain species remotely whose adjustment factor differed significantly. This mistake resulted in incorrect elevation adjustments, producing further error in the modified DEM.

3.4. Biomass Model

Unlike the previous methods, the biomass model developed by (Medeiros et al., 2015) is independent of vegetation species. Since this technique is not limited to specific vegetation species, errors are not generated from cover misclassifications and corrections may be more suitable for areas with complex species compositions and distributions. This independence is accomplished by relating estimated aboveground biomass to lidar DEM correction values. A variety of remote sensing parameters are tested to derive aboveground biomass values. Ultimately, lidar-derived canopy heights, Advance Spaceborne Thermal Emission and Reflection Radiometer (ASTER) (Red) and Interferometric synthetic aperture radar (Ifsar) are used as independent variables in a multiple variable regression to determine a relationship between remote sensing data and log-transformed aboveground biomass sampled in-situ. The estimated aboveground biomass, derived from the remote sensing parameters, is used to independently predict lidar-derived DEM error. A relationship between log-transformed aboveground biomass and DEM error (verified by RTK-GPS) was also determined. It was found that separating biomass estimates into High and Low classes and then using a quartile error adjustment within

the classes was best for adjusting the DEM. This adjustment reduced overall RMSE from 0.65 m to 0.40 m. It should be noted this error in the original DEM is by far the greatest of published error data. The original DEM was derived using the minimum binning technique with a bin resolution of 5 m. The amount of time in the field collecting RTK measurements and obtaining biomass samples for density analysis are limitations of this method.

3.5. Statistical Correction

(Buffington et al., 2016) developed the "Lidar Elevation Adjustment with NDVI" (LEAN) which statistically corrects lidar error using multispectral imagery. This approach uses high resolution normalized difference vegetation index (NDVI) and DEM elevations as independent variables in a multiple variable linear equation to predict DEM error (verified by RTK-GPS). This approach was applied along the west coast of the United States in 17 different marshes with varying vegetation species and tidal conditions. The developed model reduced RMSE values from 0.23 to 0.07 m on average for all study sites. Of the techniques to correct DEMs without the source data, this is the simplest to apply; the only fieldwork necessary is the RTK survey. However, one of the limitations of this method is it does not account for the variability of species other than the ones specific to the survey grid. Therefore, extrapolating derived relations to an expansive area may challenge this solution. Also, derived error relationships could become weak in marshes where the NDVI is not a strong function of elevation (Couvillion & Beck, 2013) or error. To apply this method to a wider area with multiple species, multiple surveys must be performed for site-specific calibration.

4. Methods

4.1. Study Areas

RTK surveys were performed in four different micro-tidal marshes on the Louisiana coast. A total of 1331 RTK points were collected: 169 points southeast of Cocodrie; 155 points near the mouth of the Pearl River; 624 points in the Big Branch Marsh Wildlife Refuge ("Big Branch"); and 463 points on the north side of Elmer's Island. The surveys consisted of a range of geographic locations, salinities, and intertidal elevations. A variety of different marsh types were analyzed, including intermediate, brackish and saline. A map of the survey locations can be seen below in Figure 4.1.

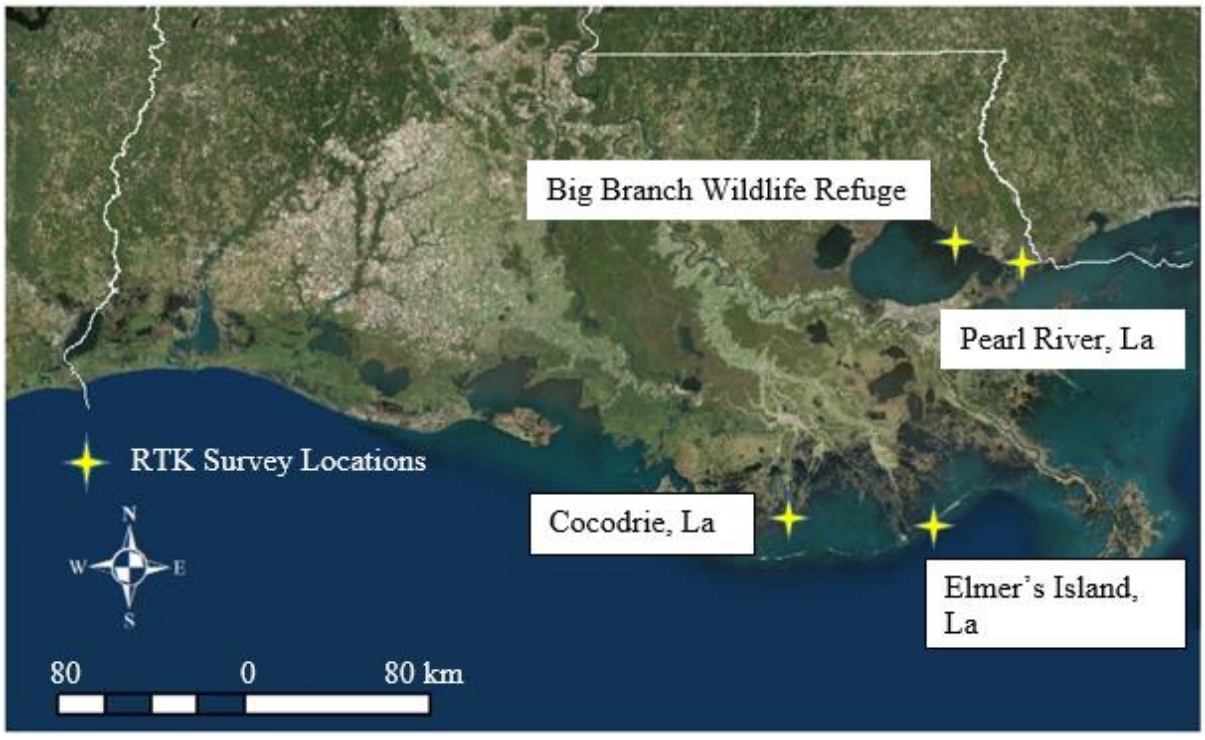

Figure 4.1. Map of coastal Louisiana showing the four RTK survey locations: Big Branch Marsh Wildlife Refuge, Pearl River, Cocodrie, and Elmer's Island. Base map source: Esri's DigitalGlobe Geoeye Earthstar Geographics.

4.1.1. Cocodrie, La Survey

Known as the “Claw” (Figure 4.2A), this salt marsh is located west of Lake Barre in the Terrebonne Basin. Terrebonne Basin is an abandoned deltaic lobe of the Teche and

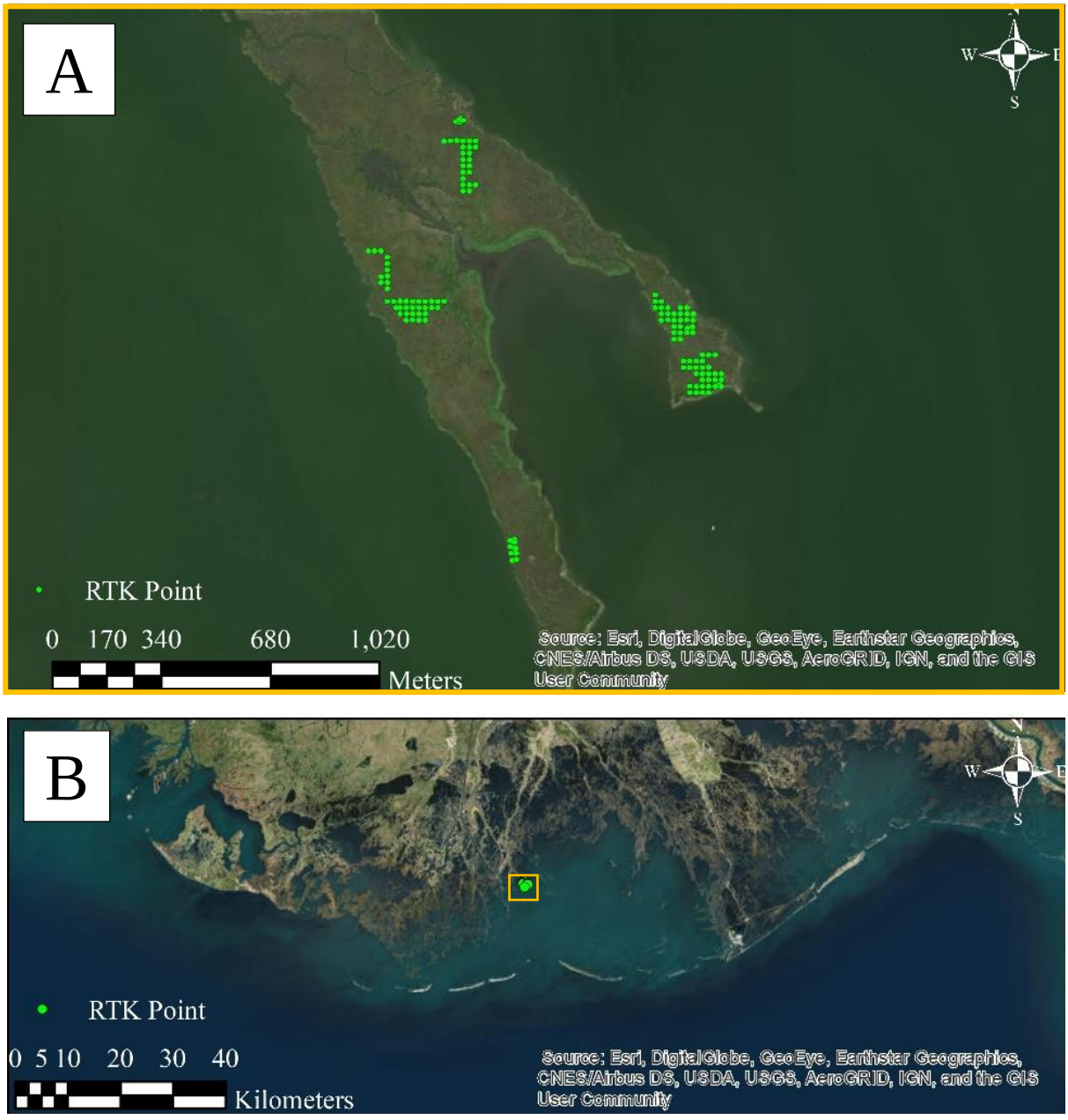

Figure 4.2. Imagery of the Cocodrie survey area. Multiple survey grids can be seen in (A) and the individual RTK survey points are in green. Map of coastal of Louisiana showing RTK location (B). Figure (A) is the portion of Figure (B) contained in the orange box.

Mississippi River deltaic plain that was active 3000 to 4000 years ago (F. C. Wang, Lu, & Sikora, 1993). This basin experiences some of the highest rates of deterioration in coastal Louisiana (Barras et al., 2003). The water levels in this area fluctuate diurnally with mean tide range of approximately 35 cm (NOAA, Station ID: 8762075). From 2013 to 2018 the mean water level was approximately 0.12 m with respect to NAVD 88, Geoid 12a (CMRS 0335). This station is approximately 7 km from the survey site. The dominant vegetation at the specific survey locations is *Spartina alterniflora*, which is known to be prominent in the lower intertidal zone of salt marshes in the Northern Gulf of Mexico (Mckee & Patrick, 1988). The mean growing season salinity is approximately 16.40 ppt (CRMS 0355). The elevation of this area is spatially dependent, and the slope is very low in the marsh interior, only 0.02 m of rise every 100 meters. RTK points are oriented north/south and spaced at 20 meter intervals, as seen in Figure 4.2A. The measured survey elevations, min, max and mean are 0.05 m, 0.59 m and 0.22 m, respectively, using NAVD 88 (Geoid 12A) as the reference system.

4.1.2. Elmer's Island Survey

Due to the higher salinities, this area is classified as a saline marsh and the dominant vegetation is *S. alterniflora* (Sasser, Visser et al. 2014) with a mean growing season salinity of 19.43 ppt (CMRS 0164). However, in recent years with the onset of warmer winters, *Avicennia germinans* (black mangrove) continues to expand throughout this region (Alleman and Hester 2011). Black mangroves can be seen in the most southeast portion of the RTK survey in Figure 4.3A. The dominant vegetation slowly transitions from *S. alterniflora* to black mangroves from the northwest to southeast direction. RTK points are spaced approximately 7.5 meters apart as seen in Figure 4.3A.

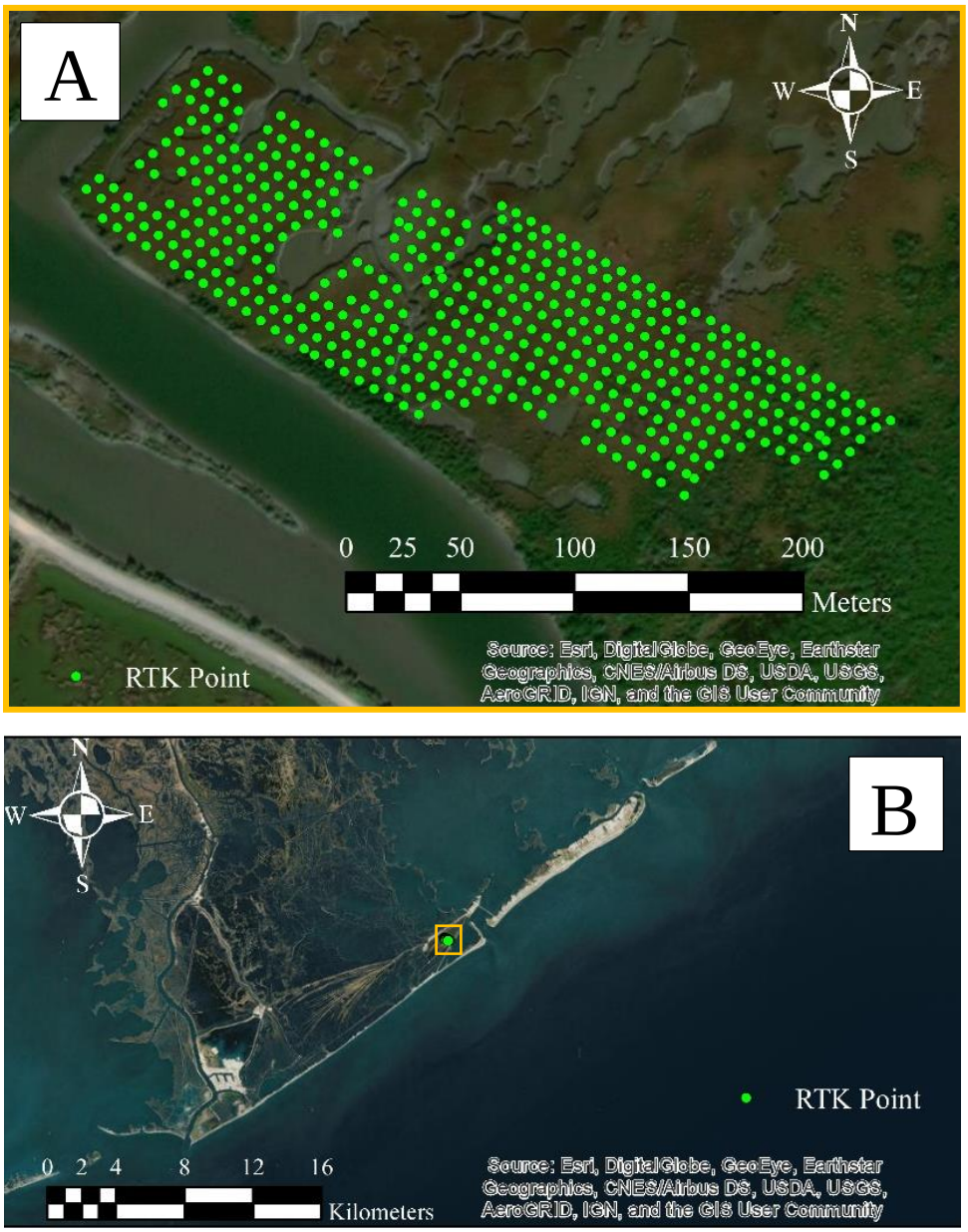

Figure 4.3. Imagery of the Elmer's Island survey area. The survey grids can be seen in (A) and the individual RTK points are colored green. Map of coastal of Louisiana showing RTK location (B). Figure (A) is the portion of Figure (B) contained in the orange box.

4.1.3. Pearl River Survey

This study area is located in the Lower Pearl River Basin between the East Pearl and West Pearl Rivers Figure 4.4B. Seasonal freshwater input from the

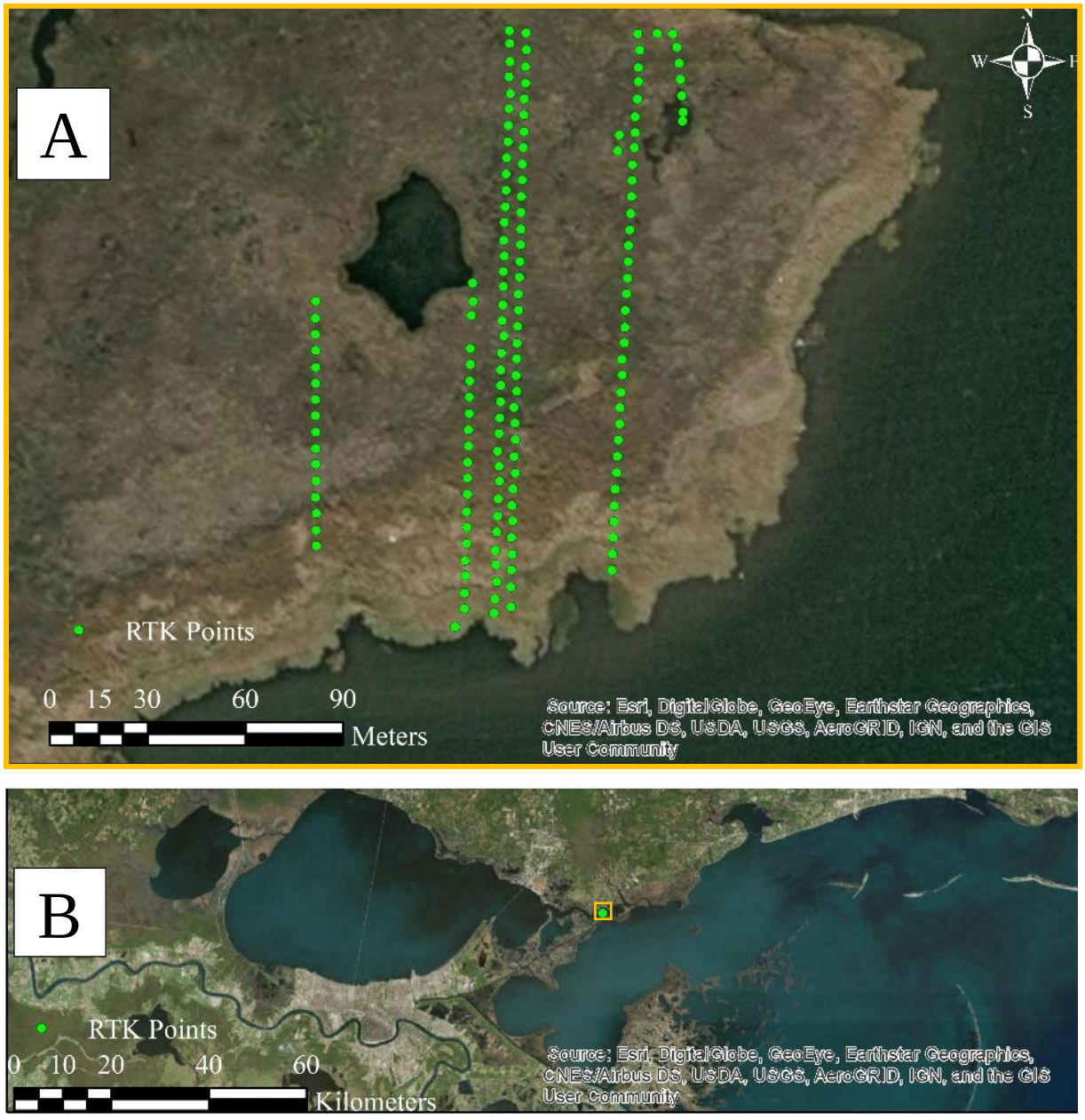

Figure 4.4. Imagery of the Pearl River survey area. The survey grids can be seen in (A) and the individual RTK points are colored green. Figure (A) is the portion of Figure (B) contained in the orange box.

Pearl Rivers highly diversifies vegetation even within a relatively small area. This basin

contains every type of marsh ranging from fresh to saline (C. Sasser et al., 2014). The particular area surveyed is classified as saline marsh by the USGS in 2013, but the species present during the survey (August 2018) suggest that it has since transitioned to a brackish marsh. The dominant species at the time of the survey was the European variety of Roseau cane (*Phragmites australis*) at the marsh edge and *Bolboschoenus robustus* towards the interior. The mean tidal range for this area is approximately 0.35-0.40 m (NOAA, Station ID: 8749704 and 8761305). From October 2013 to October 2018 the mean water level was approximately 0.17 m with respect to NAVD 88 (CRMS 3784). This station is approximately 1 km from the survey area. The mean salinity during the growing season is 5.57 ppt (CMRS 3784) but can vary seasonally and bi-monthly depending on the outflow of the Pearl Rivers (Figure 4.7) and on the tidal influx from Lake Borgne.

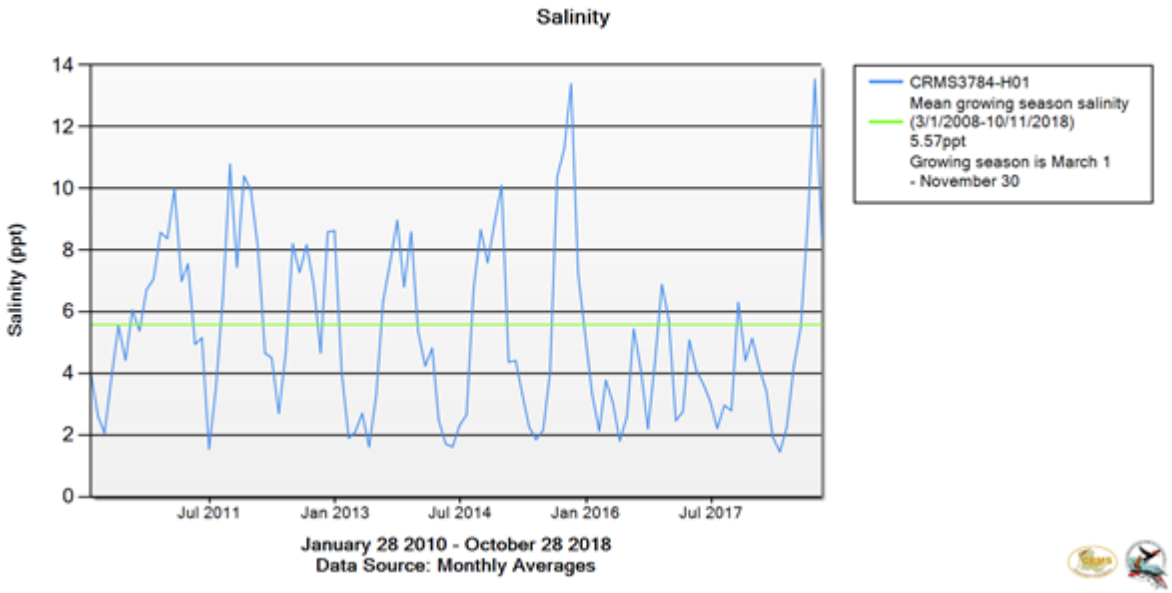

Figure 4.5. Seasonal salinity (blue) of CRMS station 3784 from January 2011 to December 2018. The average salinity during the growing season is plotted in green.

4.1.4. Big Branch Survey

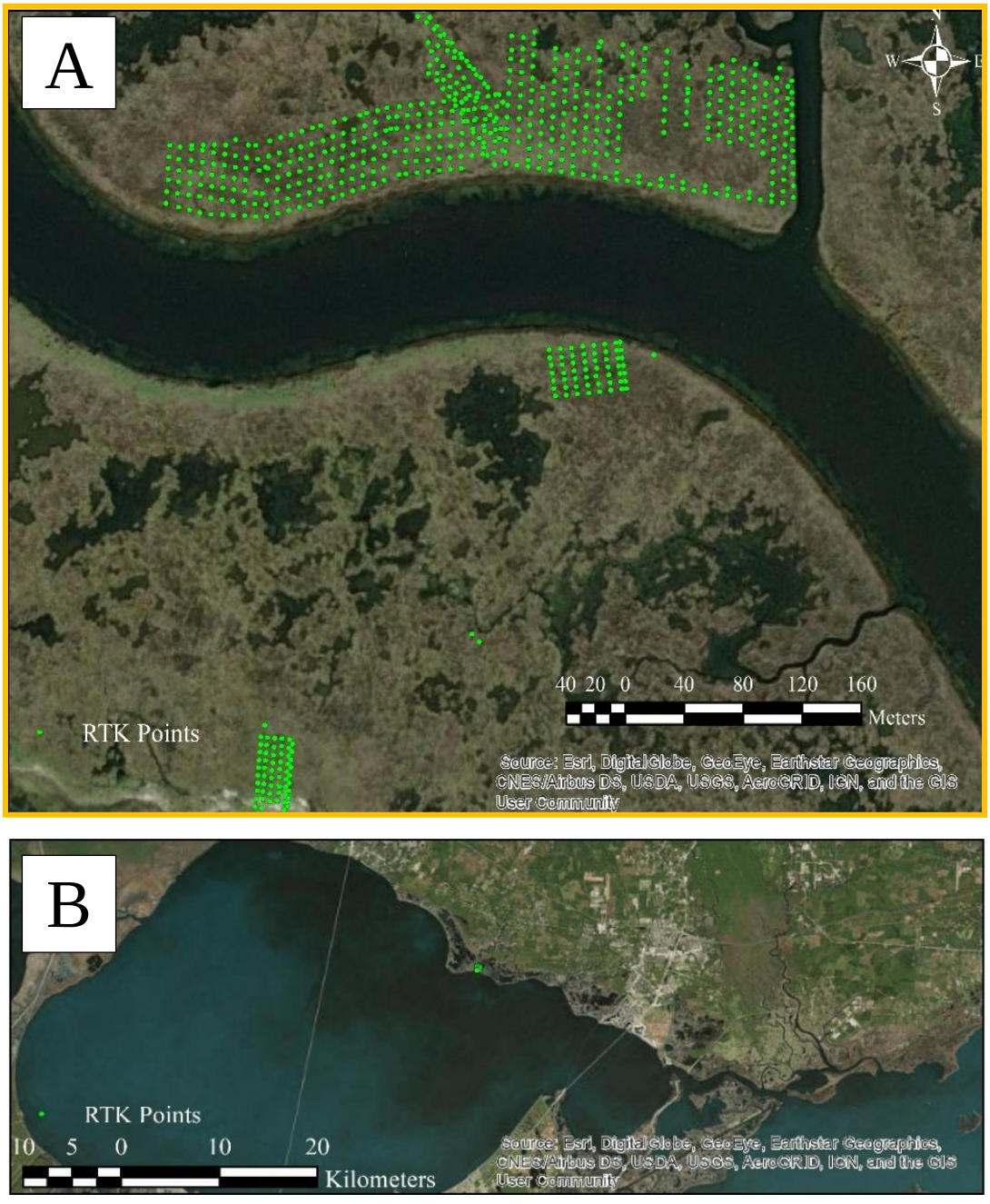

Figure 4.6. Images of the Big Branch survey area. The survey grids can be seen in (A) and the individual RTK points are colored green. Map of the east coast of Louisiana near Lake Ponchartrain with RTK location (B). Figure (A) is the portion of Figure (B) contained in the orange box.

The Big Branch Marsh National Wildlife Refuge is considered an intermediate marsh community dominated by *Spartina patens* and *Schoenoplectus americanus* (Figure 4.6A).

The Big Branch Marsh National Wildlife Refuge is considered an intermediate marsh community dominated by *Spartina patens* and *Schoenoplectus americanus*. The RTK survey roughly follows the northern edge of Bayou Lacombe and grid points are spaced every 7.5 meters (Figure 4.6.) Two smaller grids are located between Bayou Lacombe and Lake Ponchartrain and were spaced every 5 meters. The elevations of the survey points range from -0.093 m to 0.309 m and the average elevation of the entire data set is 0.154 m, referencing NAVD 88. The site is hydrologically connected to Lake Pontchartrain via bayous and tidal creeks. Publicly-accessible gauges could not be found within the marsh, but the tides in Lake Pontchartrain are diurnal with a mean range of approximately 15 cm. According to the (CRMS 0006), the mean water level is approximately 0.19 to 0.24 meters with respect to NAVD 88. Meteorological activities such as strong, persistent winds blowing across Lake Ponchartrain can create large setups and set downs along the shorelines. Further, big rain events can influence the water levels and salinities via Bayou Lacombe. For this area the mean salinity during the growing season is 3.05 ppt, measured from 2007 to 2018.

4.2. In-situ data

The following sections present the methods used for all data acquired at the study sites.

4.2.1. Real Time Kinematic Survey

RTK surveys were performed using a Trimble R8 rover provided by LSU's Center for Geoinformatics (C4G). Real time corrections were provided by the Continuously Operating Reference Stations (CORS). Uncertainties are in the range of 1.6 cm horizontally and 3.0 cm vertically at the 95th percent confidence level (Trimble, 2013). Survey grids were positioned manually in Arc Map version 10.5. To create the grids, georeferenced lines were drawn in the

preferred location and points were created along those lines at a specified spacing using the Arc Map tool “Generate points along lines”. Once saved, the individual points could be viewed, and new fields of “Easting” and “Northing” were generated in the attribute table. The x and y coordinate of each point was added to the proper field by using the “Calculate Geometry” tool, in which the user then has the option to add the coordinate of the dataframe or the source data. All RTK points were projected in Louisiana State Plane South FIPS 1702 referencing North American Datum 1983 (NAD 83). Once the attribute table contained the necessary data, it was exported using the tool “Table to Excel” in Arc Map. In Excel 2013, attributes were aligned in tabular form including: ID, Easting, Northing and elevation but lacked the heading. The Excel 2013 document was saved in CSV format and uploaded to the Trimble controller. In the field, survey points could be viewed on the controller with centimeter accuracy and elevations were recorded using the “stake point” option. This option directs the operator to the desired point until a certain level of horizontal accuracy is obtained. All RTK points were traversed to on foot as seen in Figure 4.7. In order to assure accurate elevation measurements, the “fixed position” status was obtained and a 5 second countdown timer was used during the measurement to assure steadiness. The elevation measurement was abandoned if the device moved significantly during this time period. RTK points were then stored and exported in CSV format. The CSV file was uploaded into Arc Map using the “Add XY data” option, where other data could be assessed at the individual point’s geolocation.

Figure 4.7. RTK survey at Big Branch survey site. Photo: M. Foster-Martinez

4.2.2. Vegetation Survey

At one point during the research efforts for this thesis there was desire to perform an in-depth vegetation survey to assess the accuracy of a remote sensing classification (described in Section 4.3.6). Due to an unfavorable temporal alignment between the remote sensing data and the time period in which a vegetation survey could be performed, this idea was abandoned. However, the dominant vegetation types were identified during the RTK survey. Images of the vegetation were captured using an iPhone 6. The possible species list was narrowed using the U.S. Geological Survey's (USGS's) Vegetation types in coastal Louisiana 2013 map (C. Sasser et al., 2014) , which breaks down the Louisiana coastline by marsh type and identifies which vegetation species are likely to dominate the area. Using USGS's list, species were searched

using (Allain) and compared to the images captured. Vertical measurements of vegetation were also obtained in-situ by photographing vegetation referencing marks on the RTK pole. The photographs were later analyzed in the lab to determine the vertical measurement. It should be noted, the species type, composition, and distribution of macrophytes present during the RTK survey may not represent the same circumstance at the time of the lidar acquisition.

4.3. Remote Data

4.3.1. Digital elevation models and lidar point clouds (LPCs)

A multitude of DEMs and various lidar point cloud metrics (i.e. minimum and maximum points) were used for assessing DEM error and correction. Three lidar datasets are used in this study: 2017 USGS Lidar: Upper Delta Plain, LA; 2013 USGS Lidar: Jean Lafitte, LA; and 2015 USGS South Terrebonne, LA. These correspond with the Big Branch and Pearl River sites, Elmer's Island sites, and the Cocodrie site, respectively. All point clouds and DEM data were gathered using the NOAA: Data Access Viewer, except for the 2015 USGS: South Terrebonne, LA, which was found on an USGS affiliated website. NOAA conveniently provides an option to download the published DEM or derive rasters using other LPC metrics or other interpolation techniques. Further, the user can define the data class in which the raster is generated, "all points", "ground points" etc. The final product is then emailed to the user.

The National Map Data viewer (similar to USGS's Earth Explorer) is a service provided by the 3D Elevation Program (3DEP). The USGS manages the 3DEP program with the intent to gather and provide high quality topographic data across the United States. This program is the source for future elevation data, such as LPCs and Ifsar, and incorporates the derived DEM into

the National Elevation Dataset (NED). The USGS also provides a website map interface for data downloading the lidar-derived DEMs and source data (*i.e.* LPCs).

4.3.2. 2017 USGS Lidar and DEM: Upper Delta Plain, La

This airborne lidar was flown between January 2017 and April 2017 using a Riegl LMS-Q680i lidar system at documented low water level, no snow conditions. The relative accuracy of the lidar acquisition was ≤ 6 cm within individual swaths and ≤ 8 cm RMSE within swath overlap with a maximum difference of ± 16 cm. The LPC was shot with a nominal point spacing of 0.7 meters. To meet the requirements of the ASPRS, a total of 63 ground control points were used to calibrate the elevations in areas where ground elevations were known. A total of 179 independent accuracy checkpoints, 101 Bare Ground/Low Grass land covers (101 Non-vegetated area points), 67 in Tall Weeds/Brush categories, and 11 in Woods category (78 VVA points) were used to test the accuracy of the lidar dataset. The reported vertical accuracy of the lidar data is approximately 4.9 cm RMSE with a 95th percent confidence level of 9.7 cm for non-vegetated areas. The horizontal accuracy was untested, but a theoretical horizontal accuracy of 26 cm was provided in the metadata (Partners, 2017).

The 2017 USGS Lidar DEM: Upper Delta Plain, LA was derived using the Triangulated Irregular Network (TIN) technique. This technique creates a mathematical triangulated surface between lidar points in which a z value for all (x, y) values is known. The conversion of the TIN to grid format was not specified but was resampled into 1 meter cells. When converting the surface to a grid, the vertical RMSE in open terrain increased to 5.5 cm, and the horizontal RMSE increased to approximately 26 cm.

4.3.3. 2013 USGS Lidar and DEM: Jean Lafitte and Barataria

Aerial lidar data was collected using an ALS60 Sensor. ALS60 is a discrete return topographic lidar mapping system manufactured by Leica Geosystems. Lidar data collected for the Jean Lafitte survey area has a nominal pulse spacing of 1 meter. The processed data includes up to 4 discrete returns per pulse, along with intensity values for each return. Collection began on March 5, 2013, and was completed on March 8, 2013. The tested vertical accuracy after creating the TIN was 6.2 cm RMSE and 12.2 cm at the 95th percent confidence level for non-vegetated areas. The horizontal accuracy is estimated to be 42 cm RMSE but was not tested. In order to have consistent DEMs throughout this study, the Jean Lafitte LPC was filtered for bare-earth points and surfaced using the TIN technique. The TIN was then converted to 1 meter grid DEM. Other rasters were created using average, minimum and maximum binning techniques at resolutions of 2.5, 5.0, 7.5 and 10 m. All data was processed using the NOAA Data Access Viewer (Partners, 2013).

4.3.4. 2015 USGS lidar: South Terrebonne, LA

Airborne lidar was collected using a Leica ALS70-HP. Similar to the ALS50, ALS70-HP is produced by Leica Geosystems and is also a discrete return topographic lidar system. The acquisition mission began February 13, 2015 at normal water levels, no snow, and leaf off conditions. The lidar was shot at a flying altitude of approximately 1600 meters with a nominal point spacing of 0.5 m. The tested vertical accuracy is 7.2 cm RMSE and 15.2 cm at the 95th percent confidence level for non-vegetated areas. The horizontal accuracy was untested. The LPC was downloaded from USGS's NED viewer. A LAS dataset was created in Arc Map using the "Create LAS Dataset" tool. The "LAS Dataset to TIN" tool was then used to convert the point file into a surface. The TIN was converted to a raster using the "TIN to Raster" tool using linear interpolation at a grid size 1 m. Other rasters were created using the "LAS to Raster" tool

by implementing average, minimum and maximum binning techniques at resolutions of 2.5, 5.0, 7.5 and 10 meters (USGS, 2016).

4.3.5. National Agriculture Imagery Program

The National Agriculture Imagery Program (NAIP) acquires aerial imagery during the agricultural growing seasons in the continental US. NAIP is administered by the USDA's Farm Service Agency (FSA) through the Aerial Photography Field Office in Salt Lake City. NAIP imagery is acquired at a one-meter ground sample distance with a horizontal accuracy that matches within six meters of photo-identifiable ground control points. These ground control points are used to inspect the image. Additionally, tiles are inspected for horizontal accuracy and tonal quality. Since 2007, a near infrared option has been offered in addition to the red, blue, and green bands. Four band imagery is available in Louisiana for the years: 2010, 2013, 2015, and 2017, which can be downloaded via the USGS's Earth Explorer (USGS).

The NAIP imagery is atmospherically corrected using the dark object subtraction (DOS) method. The goal of this method is to eliminate background noise the sensor encounters by scaling digital number to a no return value (Gilmore, Saleem, & Dewan, 2015). This technique subtracts the minimum reflection value of each band for all pixels, therefore all minimum pixel values are equal to zero. A schematic of the DOS technique can be seen in Figure 4.8 and was implemented using ERDAS Imagine 2018. The initial file is the JPEG 2000 file downloaded from Earth Explorer. The original image is split into the four band components, and a subtraction function is implemented to reduce the minimum value of the pixels for each band to zero. The third line is the calculated image of each band and is stored as temporary file. A stack layer function is performed on the set of temporary files. The stack layers function combines all the bands into the new image, similar to the original JPEG 2000 file.

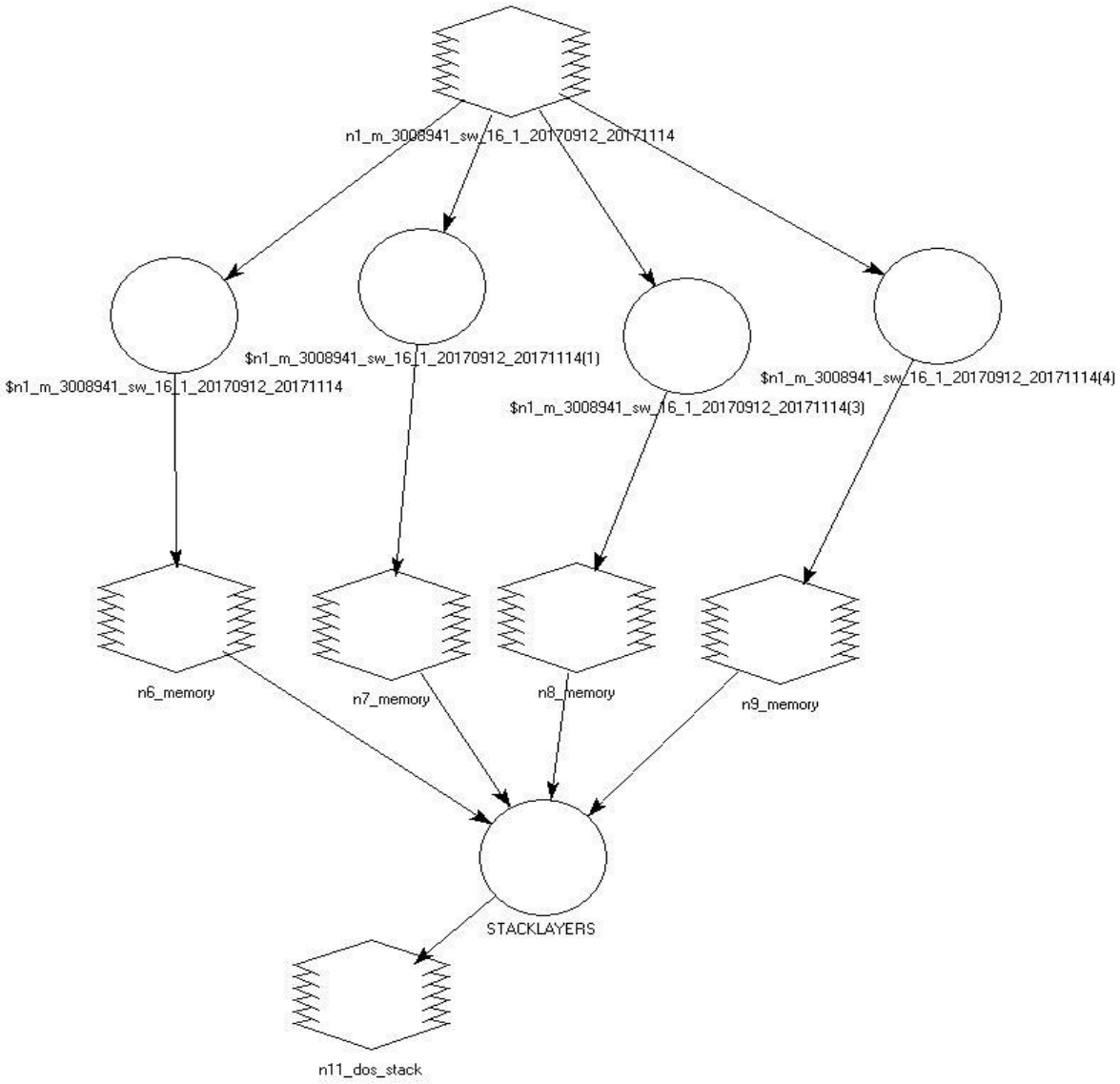

Figure 4.8. Schematic of the Dark Object Subtraction technique performed on the NAIP imagery.

The produced file is used to calculate NDVI. The NDVI raster is created using the NDVI function in ERDAS Imagine 2018, which uses the general formula:

$$NDVI = \frac{Near\ Infrared - RED}{Near\ Infrared + RED} \quad \text{Eq. 4.1}$$

Where *Near Infrared* and *RED* refer to the band of the image. The raster is then reprojected to Louisiana State Plane South FIPS 1702 using the "Reproject" tool in ERDAS Imagine and

exported to Arc Map.

4.3.6. National Agriculture Imagery Program Object Based Classification

An object based unsupervised classification was performed in ERDAS Imagine 2018 using the k-means approach. This is a clustering algorithm that needs no training data and finds an underlying structure between pixels by organizing image pixels into classes with spectrally similar characteristics (Duda & Canty, 2002). All four NAIP spectral bands were used as inputs for the clustering algorithm, and the number of clusters was set to 10. The classification was calculated for 10 iterations to determine a final grouping. Once the raster was created it was re-projected to Louisiana State Plane South FIPS 1702 and exported to Arc Map. NAIP imagery is captured at different times of the day, causing there to be different levels of illumination between tiles. This difference results in varying digital number or spectral responses between images. In order to expand classification beyond tiles, DNs must be comparable. This is a major complication for image classification. In this work, classification remained within the tile so adjusting or matching image's histograms was not necessary.

4.3.7. European Space Agency Sentinel 2 Imagery

Sentinel 2 is a European, wide-swath, high-resolution, multi-spectral imaging mission. Sentinel 2 consists of twin satellites flying in the same orbit but phased at 180 degrees. This was designed with the intent to provide a high revisit frequency of 5 days at the equator. Utilizing a push broom design, Sentinel 2a and 2b carry a multispectral optical sensor that samples 13 spectral bands: four bands at 10 m, six bands at 20 m, and three bands at 60 m spatial resolution at swath width of 290 km. One of the unique advantages of Sentinel 2 is the three vegetation red edge bands. These bands aid the overall goal of Sentinel 2 like many of the other Copernicus

missions, which is to provide timely information for land cover/change classification, atmospheric correction and cloud/snow separation (Martimor et al., 2007).

Sentinel 2 level 1C data is available on USGS's Earth Explorer. Level 1C data includes the top of atmosphere (TOA) reflections with applied radiometric and geometric corrections. (Drusch, Del Bello et al. 2012). Sen2Cor is applied to all images for atmospheric correction. Sen2Cor is an image based atmospheric correction approach that uses a semi-empirical algorithm that integrates image-based retrievals with Look-Up tables from the library of radiation transfer (LibRadtran) model to remove atmospheric effects from multi spectral images (Martins, Barbosa et al. 2017). The correction is performed using the ESA provided Sentinel toolbox which includes the Sen2Cor processor for level 1C data. Once corrected, the individual bands were imported into ERDAS Imagine, where a "Stack Layer" function combines all bands into one image of multiple layers. NDVI was calculated using the NDVI function in ERDAS Imagine. The imagery was then reprojected to Louisiana State Plane South FIPS 1702 using the "Reproject" tool.

4.4. Data Organization and Analyzation

All imagery derived files, DEMs, and LPC derived metrics were delivered in raster format and uploaded to Arc Map. Vector sets were created using the "Extract multi values to points" tool using the RTK shapefile. This tool extracts pixel values from the raster in the exact location of the point. The "Table to Excel" tool was used to export the vectors. Once the vectors were in ".xlsx" format the shapefiles and their attributes could be viewed, inspected and edited to delete incorrect or erroneous data points caused by RTK user error. RTK values beyond the 95^{th} percentile were inspected and located in Arc Map to justify deletion. A new column named "DEM error" was calculated by subtracting the RTK elevation value from the extracted DEM

value. Other relations between independent variables were plotted and coefficients of determinations were calculated in Excel 2013.

The vector sets were imported into R-Studio Version 3.4.1, where error prediction models could trained and tested. Two regression types were used to create error prediction models: multi variable linear regression and random forest regression. The linear regression model, which was used for the LEAN method (section 3.5), was built using 100% of the vector set. Model coefficients were calculated by calling the linear model function "lm ()" in R-Studio Version 3.4.0. The regression summary report shows which independent variables are deemed significant. However, similar to the published study (Buffington 2017) all coefficients were copied back into Excel 2013 to predict error for a separate subset of data near the survey location. Most of time variables were deemed insignificant due to multicollinearity, but still produced a significant model.

Random forest regression is an ensemble learning method in which decision trees are grown and bagged to determine an average prediction value (Liaw & Wiener, 2002). Each individual tree decision is grown using a randomly selected subset of the dataset. The individual nodes are then split based on the best split between a random subset of independent variables (Breiman, 2001). This approach is advantageous because it's not typically susceptible to overfitting. In order to use random forest functions in R-studio, two packages were downloaded, "Random Forest" and "caret". The random forest model was built using the "randomforest ()" function in R-studio. This function allows the user to tune the model using a variety of advanced options. However, the only adjustment implemented was changing the number of trees. This number can be optimized by simply plotting the random forest model, "plot(model)". When building the model the "set.seed()" function was used to ensure the same random numbers

selected for each training, making the models comparable. Many different combinations of independent variables were used to build a model that explains the highest percentage of variance. The importance of each variable in the regression was assessed using the “ImpVar ()” function. Once the model was trained it was applied to a separate dataset using the “predict ()" function, in which the random forest model predicts error based on the combination of decision trees created from the training.

To determine the performance and transferability of the error calculation, a theoretical DEM at each RTK point was created by subtracting the predicted error from the original DEM. A second DEM error was computed by subtracting the RTK elevation from the new DEM. New error statistics were calculated using the new DEM error which was then compared to the original DEM error to determine a percent improvement.

5. Results

5.1. Big Branch Marsh National Wildlife Refuge

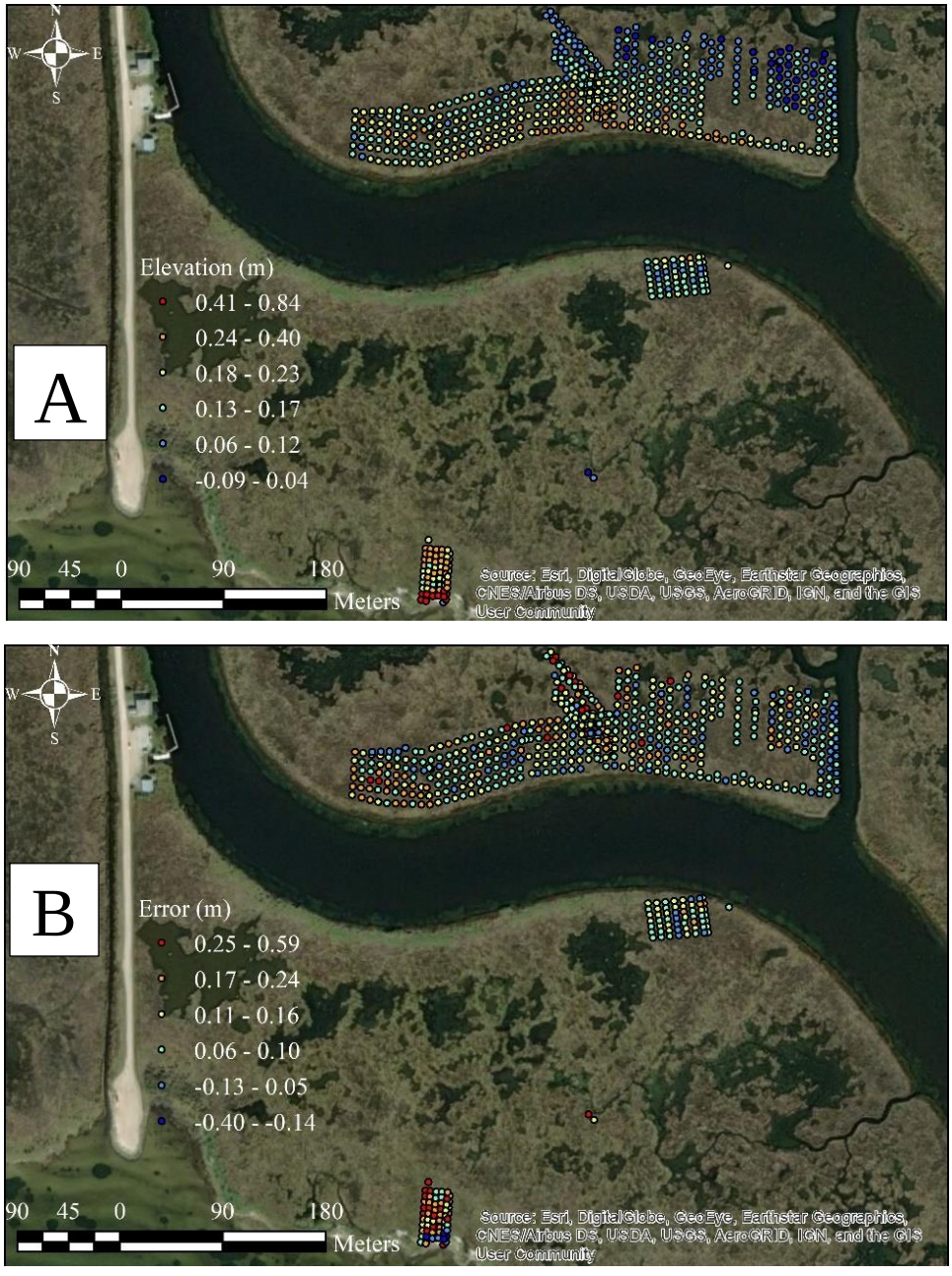

Figure 5.1. RTK elevation (A) and error (B) visualization of the Big Branch RTK survey. Error is calculated by subtracting the RTK elevation value from the DEM. Color codes distinguish six natural breaks in the data.

At Big Branch Marsh Wildlife Refuge (referred to as "Big Branch" herein), an intermediate marsh, the RTK measurements of elevation ranged from -0.09 to 0.14 m (NAVD88) (Figure 5.1A). The DEM error ranges from -0.39 to 0.59 meters (NAVD88) with a few DEM elevations below the RTK measurements (B). However, the error statistics (Table 5.1), specifically the mean error of 0.11 cm, indicate that the majority of the DEM is positively biased. This positive bias is further confirmed by comparing the MAE to the ME (both 11 cm). The RMSE of the entire survey is 0.13 m, which is 0.08 m greater than the documented RMSE of the entire lidar dataset.

Table 5.1. Summary of the error found at the Big Branch survey area, calculated as mean error (ME), mean absolute error (MAE) and root mean square error (RMSE).

DEM	ME (m)	MAE (m)	RMSE (m)	1st Quart.	3rd Quart.
2017 USGS: Upper Delta Plain, LA	0.11	0.11	0.13	0.06	0.14

The error patterns are spatially variable, but there are certain zones of the survey in which error is beyond the 3rd quartile of the error distribution. Errors of these magnitudes can be found in the southwest portion of the grid that's north of Bayou Lacombe. This pattern is also found in the most southern survey section just north of the beach area (warmer colors in Figure 5.1B). In order to quantify spatial relations of error with respect to relative elevation, error is plotted with respect to RTK elevation (Figure 5.2). Overall, there is an inverse relation between error and RTK elevation; the R-squared value is 0.1045 using a linear least squares regression (LLS). Upon further inspection, there seem to be two patterns in the scatter plot. Particularly between the lower elevations in the range of 0.0 m to 0.15 m, the higher-error data roughly follows a slope of a -1:1 line with respect to elevation.

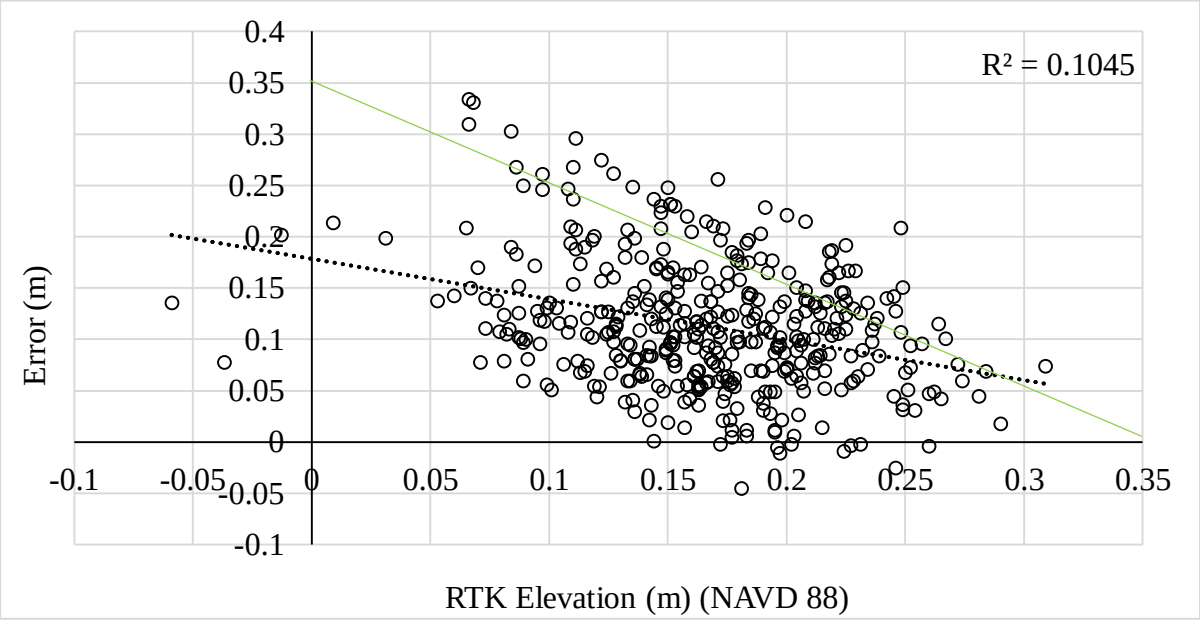

Figure 5.2. Plot showing DEM error (m) versus measured RTK elevation at Big Branch (most northern grid (Figure 5.2A), fitted with a linear least squares (LLS) trend line and sloped 1:-1 line (green).

In Figure 5.3 error is plotted with respect to NDVI. On the whole, there is no correlation between NDVI and error at this site, receiving an R-squared value of 0.00005 (LLS) with a slightly positive relation. The bulk of the RTK data points are in the NDVI value range from 0.3 to 0.4. Peak error occurs at an NDVI value of 0.34, and errors decrease in the positive and negative directions from the peak value. The lowest (i.e. most negative) error corresponds with an NDVI value of 0.425.

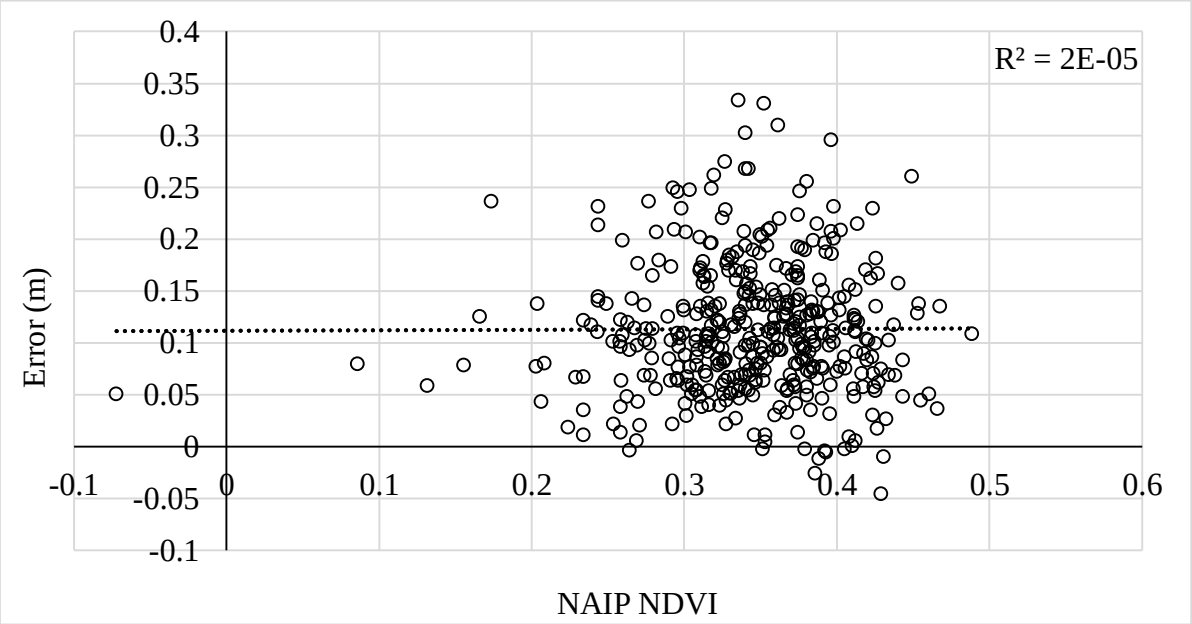

Figure 5.3. DEM error (m) versus NAIP NDVI at Big Branch, fitted with a linear least squares (LLS) trend line.

In order to understand the distribution of biomass with respect to relative elevation, NDVI is plotted against RTK elevation (Figure 5.4). There is a positive relation between RTK elevation and NDVI, receiving an R-squared value of 0.1118 (LLS). Since NDVI roughly corresponds to chlorophyll levels, chlorophyll increases with increased relative elevation. Two NDVI values are below 0 with respect to RTK elevation. These pixels were examined and the low NDVI values are due to spectral mixing between the water and vegetative edge.

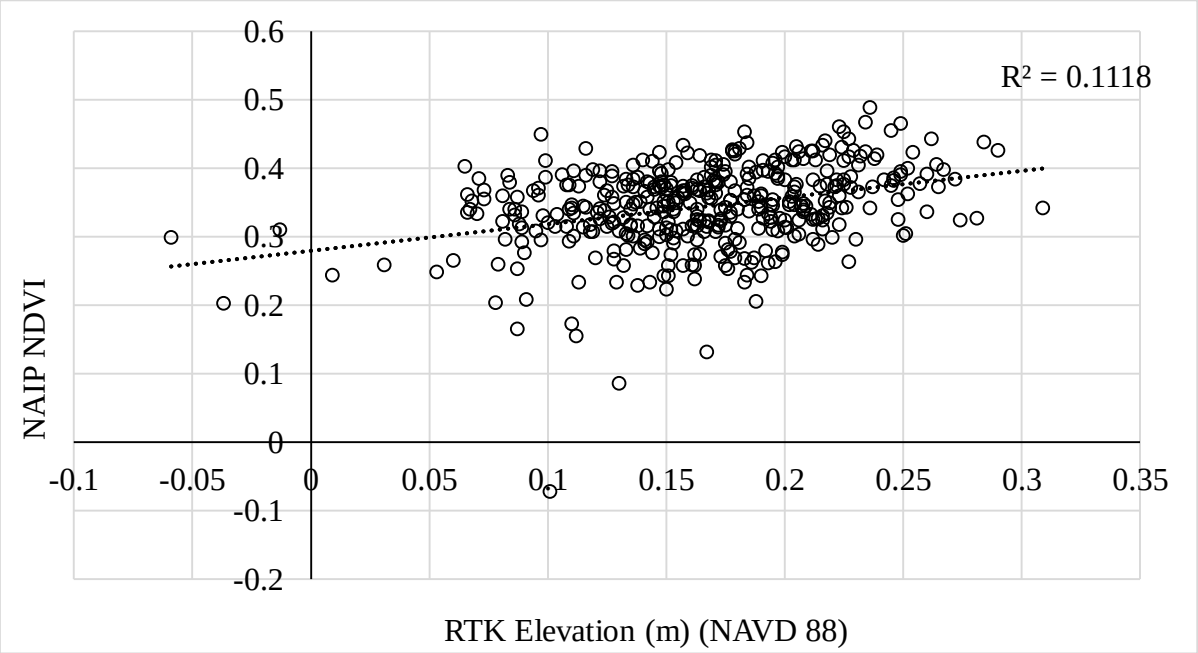

Figure 5.4. NAIP 2017 NDVI versus measured RTK elevation (m, NAVD88) at Big Branch, fitted with a linear least squares (LLS) trend line.

5.2. Elmer's Island

5.2.1. Elmer's Island Survey 1

The measured RTK elevations taken at Elmer's Island were compared to the 2013 USGS: Barataria, LA lidar-derived DEM (Figure 5.5). The DEM errors in this saline marsh are spatially variable ranging from -0.08 to 0.33 m. Errors beyond the 3rd quartile are located along the southwest edge, near the large canal, and in the north portion of the south east edge. This latter zone is a transition between *Spartina alternifora* and *Avicenna germinans*. Smaller systematic errors and errors within the random range can be found in the interior sections between the ridges found at the water's edge. The mean error and mean absolute error are both approximately 0.10 cm (Table 5.2), meaning most of the error is greater than zero. The RMSE for this dataset is 12 cm, nearly double the given RMSE of the lidar dataset, a value of 0.062 m. Unlike the

intermediate marsh, a relation between NDVI and error exists, receiving an R-squared value of 0.2856 (Figure 5.6). NDVI values range from -0.58 to 0.48, and the highest errors are associated

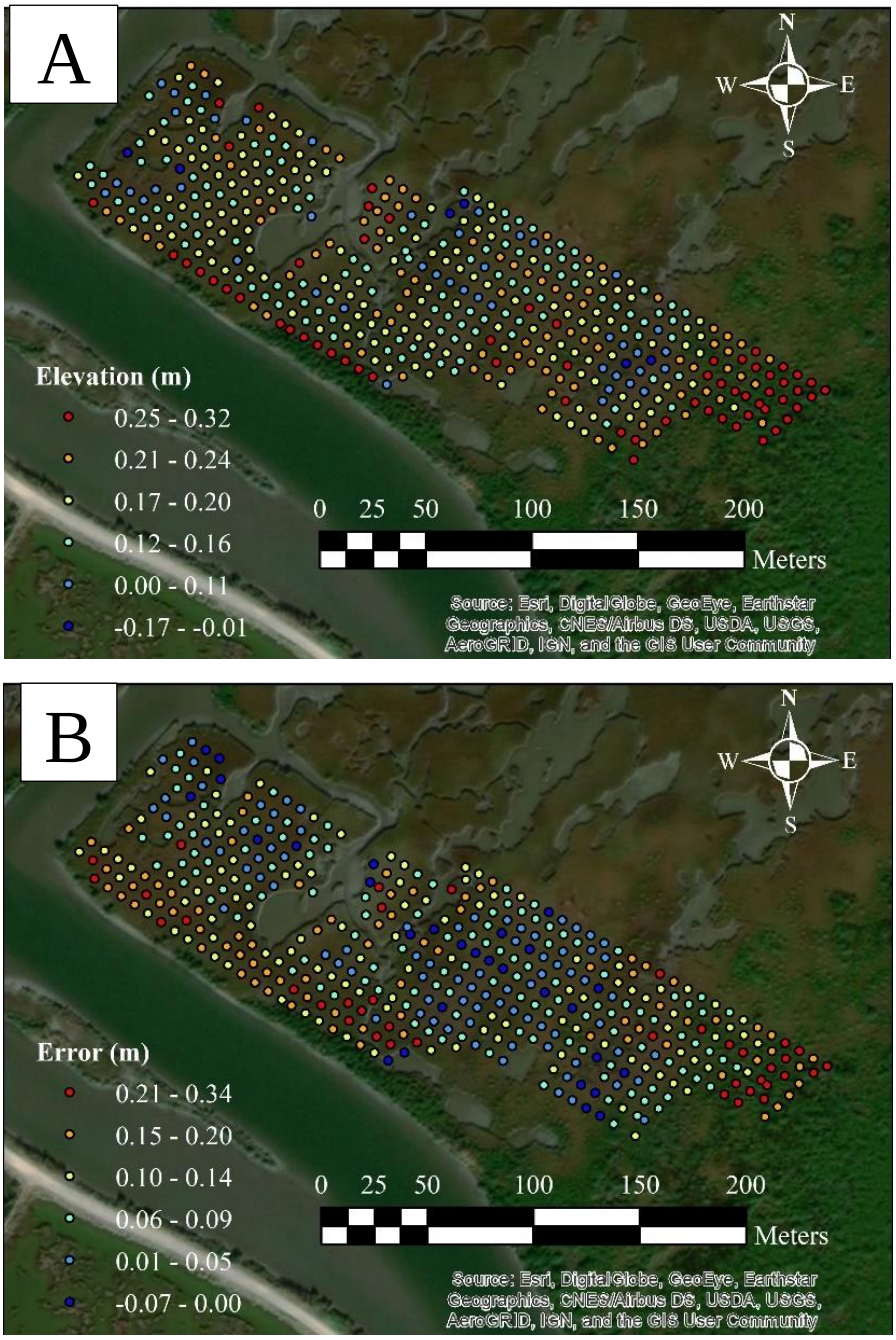

Figure 5.5. Visualization of RTK elevation (m) (A) and DEM error (B) at Elmer's Island survey 1. Color codes distinguish six natural breaks in the data.

with high NDVI values, giving a positive relation. A large bulk of NDVI values are negative,

which roughly correspond to lower errors. Low NDVI values are abnormal for vegetation. The low NDVI values are found in areas of sparse vegetation where mud is exposed and also in areas

Table 5.2 Summary of the error found at the Elmer's Island survey area, error statistics calculated as mean error (ME), mean absolute error (MAE) and root mean square error (RMSE).

DEM	ME (m)	MAE (m)	RMSE (m)	1st Quart. (m)	3rd Quart. (m)
2013 USGS: Barataria, LA	0.1	0.1	0.12	0.05	0.14

near the vegetation edge and water where spectral mixing has occurred. Overall, the relationship between these two variables supports the use of NDVI as a predictor variable with the addition of other independent variables to calculate error in this marsh type.

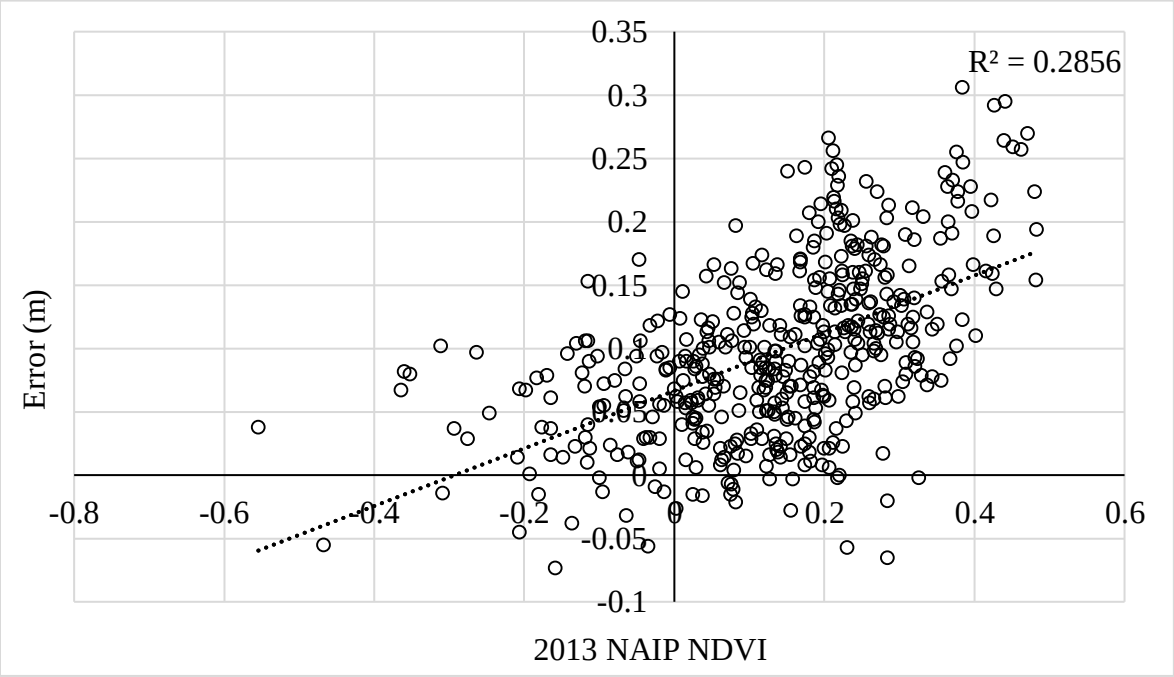

Figure 5.6. Plot showing DEM error (m) versus NAIP NDVI at the Elmer's Island survey, fitted with a linear least squares (LLS) trend line.

A strong relation between NDVI and RTK elevation also exists, receiving a coefficient of determination of 0.3179 (Figure 5.7). The positive relationship inherently shows low NDVI

values corresponding to lower elevations and high NDVI values corresponding to higher elevations. As one approaches the higher elevations from 0.2 to 0.3 meters, the relation between NDVI and elevation becomes even tighter. It's interesting to note that the NDVI values of *Spartina alterniflora* and *Avincennia germinans*, as a whole, respond linearly with respect to elevation versus a piecewise response as one might have expected. Further, below the elevation of 0.07 meters where the NDVI values are equally positive and negative, errors approach the 75th percentile, averaging 0.138 m.

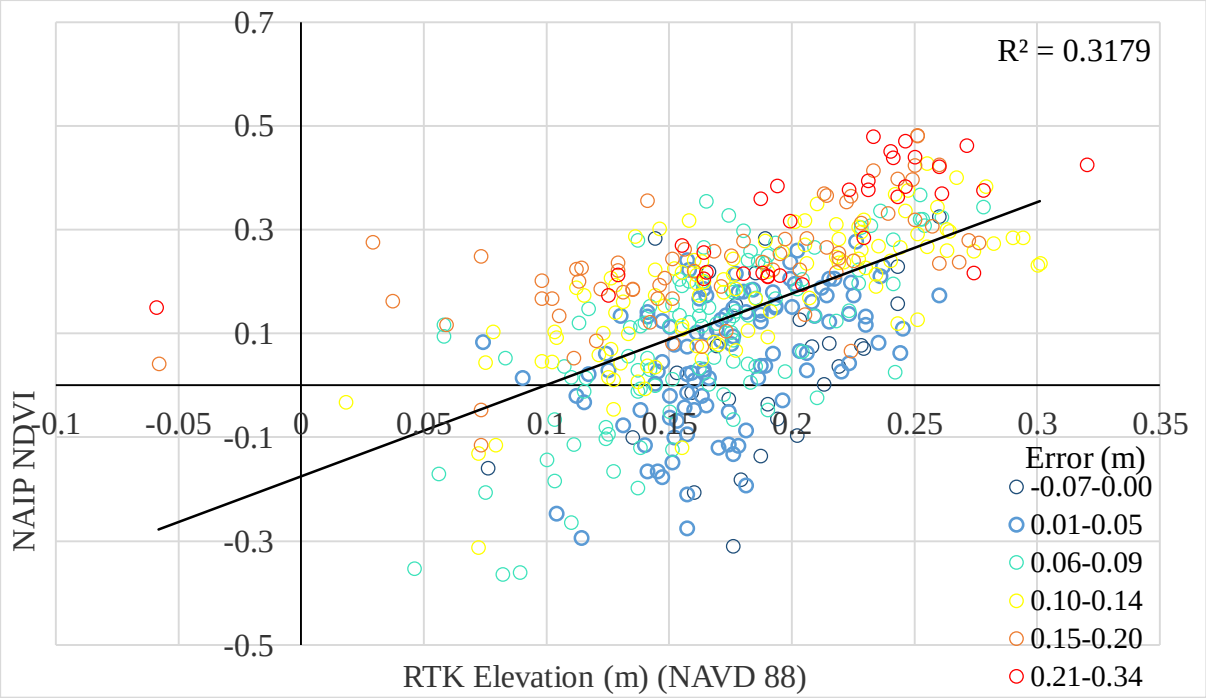

Figure 5.7. NAIP 2013 NDVI versus measured RTK elevation (m NAVD88) at Elmer's Island, fitted with a linear least squares (LLS) trend line for all points. Points are color coded based on the range of error associated with the RTK point.

It is interesting to note that despite error and NDVI having a significant correlation and NDVI with respect elevation having a significant correlation, the relationship between RTK elevation and error is does not translate (Figure 5.8). Even though peak error value is seen at the

higher elevations, there is barely a positive relationship between the two, receiving an R-squared value of 0.0085. Below the elevation of 0.07 meters where the NDVI values are equally positive and negative, errors approach the 75th percentile, averaging 0.138 m (Figure 5.8).This suggest a factor other than biomass is causing the DEM to be positively biased.

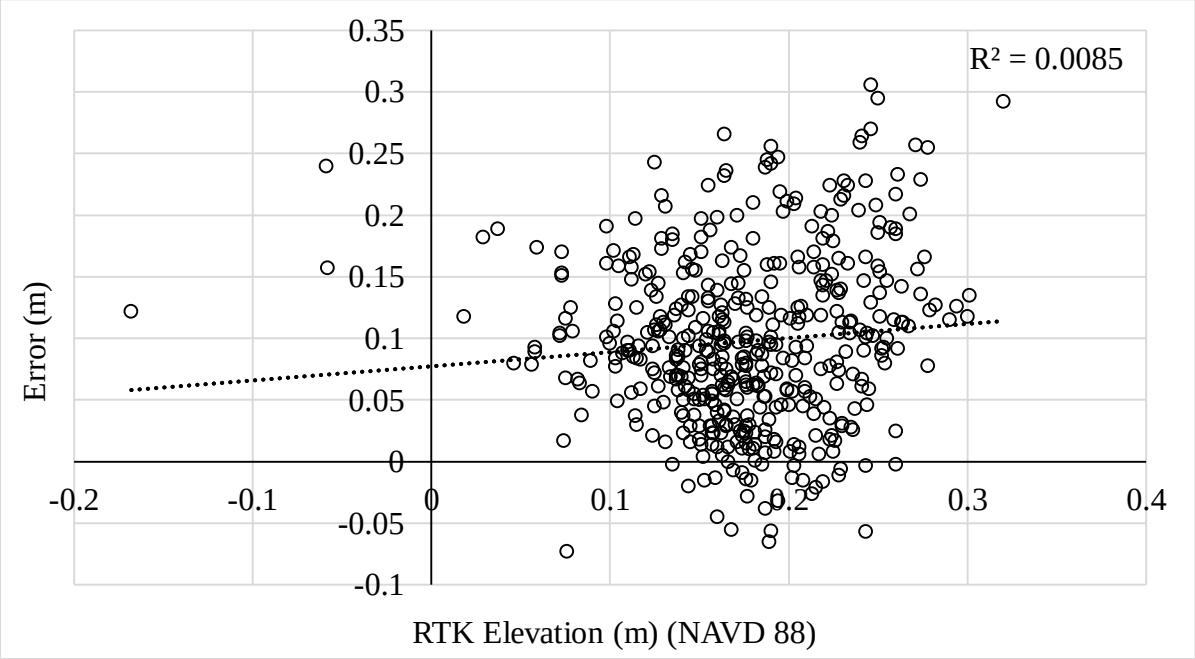

Figure 5.8. Plot showing DEM error (m) versus measured RTK elevation at Elmer's Island, fitted with a linear least squares (LLS) trend line.

5.2.2. CPRA Survey

The CPRA survey is located in a similar marsh to the Elmer's survey, however the error range extends from -1.0 to 0.90 m (Figure 5.9). This range is much larger than Elmer's Island survey 1. The error statistics also vary; the mean absolute error is 0.19 m (Table 5.3), which is 2 cm larger than the mean error. This difference indicates there is some negative error, but overall the DEM is positively biased. The RMSE of the extracted dataset is 0.25 m, which is over 4 times higher than the RMSE documented by the lidar dataset. Despite using the same DEM as the Elmer's Island calculations, error is nearly doubled for all statistical measures. A more

rigorous breakdown of this error can be seen in the next section.

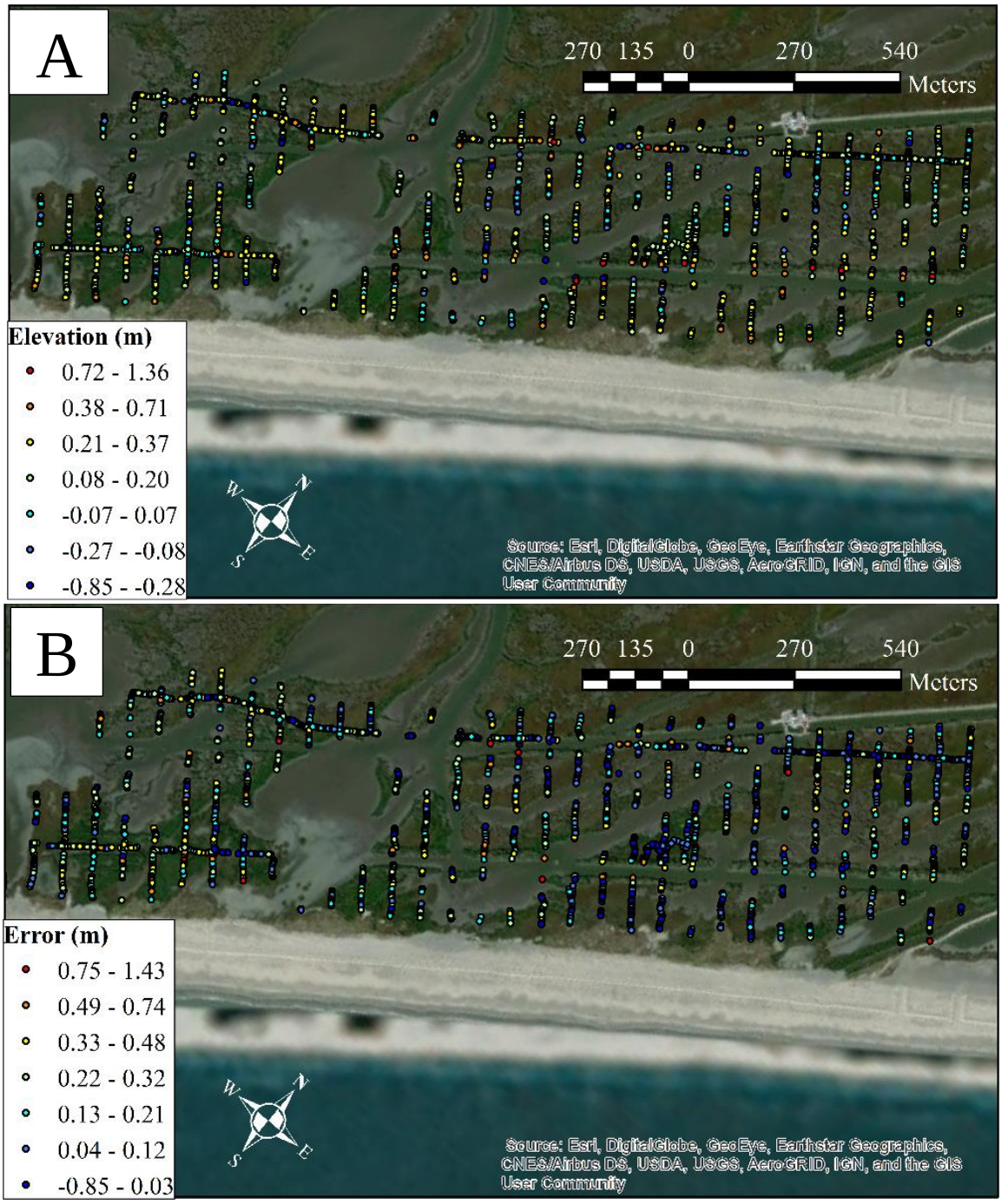

Figure 5.9. RTK elevation (A) and error (B) visualization of a part of the 2017 CPRA RTK survey at Elmer's Island. Error is calculated by subtracting the RTK elevation value from the DEM. Color codes distinguish seven natural breaks in the data.

Table 5.3. Summary of the error found at the Elmer's Island in the CPRA survey area, calculated as mean error (ME), mean absolute error (MAE) and root mean square error (RMSE).

DEM	ME (m)	MAE (m)	RMSE (m)	1st Quart. (m)	3rd Quart. (m)
2013 USGS: Jean Lafitte, LA	0.17	0.19	0.25	0.06	0.27

5.2.3. Elmer's Island Classification Map

The CPRA survey area was classified into 10 different ground cover classes (Figure 5.10). The separation of RTK points by class was performed so error statistics may be more comparable to Elmer's Island survey 1 (Table 5.4). The vegetation classes include classes 1, 2, 3, 5, and 8. These determinations were based on their proximity to marsh areas. Classes 4, 6, 7 and 9 mostly represent water pixels or wet pixels, and class 10 represents beach sand, road and buildings. It can be seen that some of the water pixels are unclassified (black). Classes 3 and 5 mostly represent marsh cover and class 8 represents black mangrove cover. Classes 1 and 2 are mostly found at the water's edge or in small ponds of interior marsh and mostly likely represent spectrally mixed pixels of water, mud and vegetation, and therefore, are not pure vegetation classes. Seen in Table 4, the error statistics of classes 1 and 2 are very similar, with RMSE values of 0.34 m and 0.31 m, respectively. RTK points classified as classes 1 and 2 also have very similar mean elevations of -0.03 and 0.00 m, respectively. Class 3 and 5 have similar error

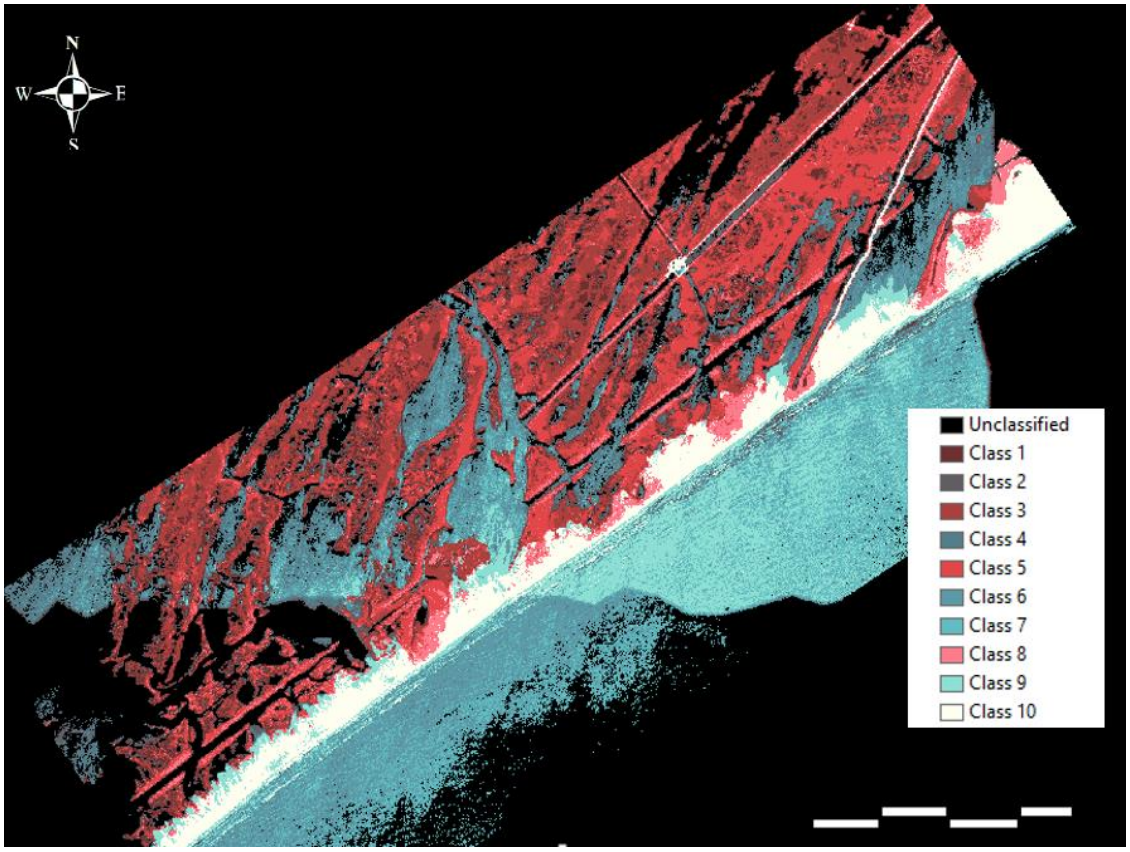

Figure 5.10. A 10 class land cover classification map of the 2017 CPRA RTK survey area. The marsh and mangrove classes are associated with classes 1, 2, 3, 5 and 8.

Table 5.4. Summary of the error found at the Elmer's Island survey area by land cover class. Error statistics are calculated as mean error (ME), mean absolute error (MAE) and root mean square error (RMSE). Mean RTK elevation calculated within each individual class.

Error Statistic	Class 1	Class 2	Class 3	Class 5	Class 8
ME (m)	0.23	0.19	0.15	0.17	0.19
MAE (m)	0.25	0.24	0.18	0.18	0.22
RMSE (m)	0.34	0.31	0.25	0.23	0.29
Mean RTK Elevation (m)	-0.03	0.00	0.12	0.17	0.33

statistics with mean errors of approximately 0.15 and 0.17 m and mean absolute errors of 0.18 and 0.18 m, respectively. Although it was not verified in-situ, inspection of the imagery suggests class 3 and 5 mostly represent various degrees of *Spartina alterniflora*, which is the dominant vegetation found in the Elmer's Island survey 1. The mean elevations for class 3 and 5 are 0.12

and 0.17 m, respectively. Despite being able to separate error statistics and elevations of RTK points, the classification map is not tested for accuracy against a target cover. The classification map merely gives insight to the performance of a broad correction technique and could possibly be used as a filter for DEM correction.

5.3. Cocodrie, LA Survey

The results from the RTK survey in a saline marsh in Cocodrie, LA, were compared to the latest DEM of the area (2015 USGS: LA South Terrebonne) and an older DEM (2011 USGS: LA Region 1). The DEM error is spatially variable and ranges from -0.15 to 0.17 m (Figure 5.11B). By zone, the DEM extracted at the furthest north grid consistently over predicts bare earth elevation, and the RTK elevations in this area were consistently lower than the other RTK points (Figure 5.11A), approximately 0.18 m. High error can also be found along the ridges, where this a slight increase in elevation. When comparing the two DEMs, the error statistics of the 2011 DEM are much larger than the 2015 statistics, with RMSE values of 0.24 and 0.07 m, respectively (Table 5.5). The RMSE values for the 2011 and 2015 lidar datasets are reported as 0.125 and 0.08 meters in the open terrain, which is 1.92 and 0.93 times less than the RMSE values derived from the survey. For both datasets the mean error and mean absolute error are nearly identical, suggesting most of the error is above zero and the DEM is positively offset.

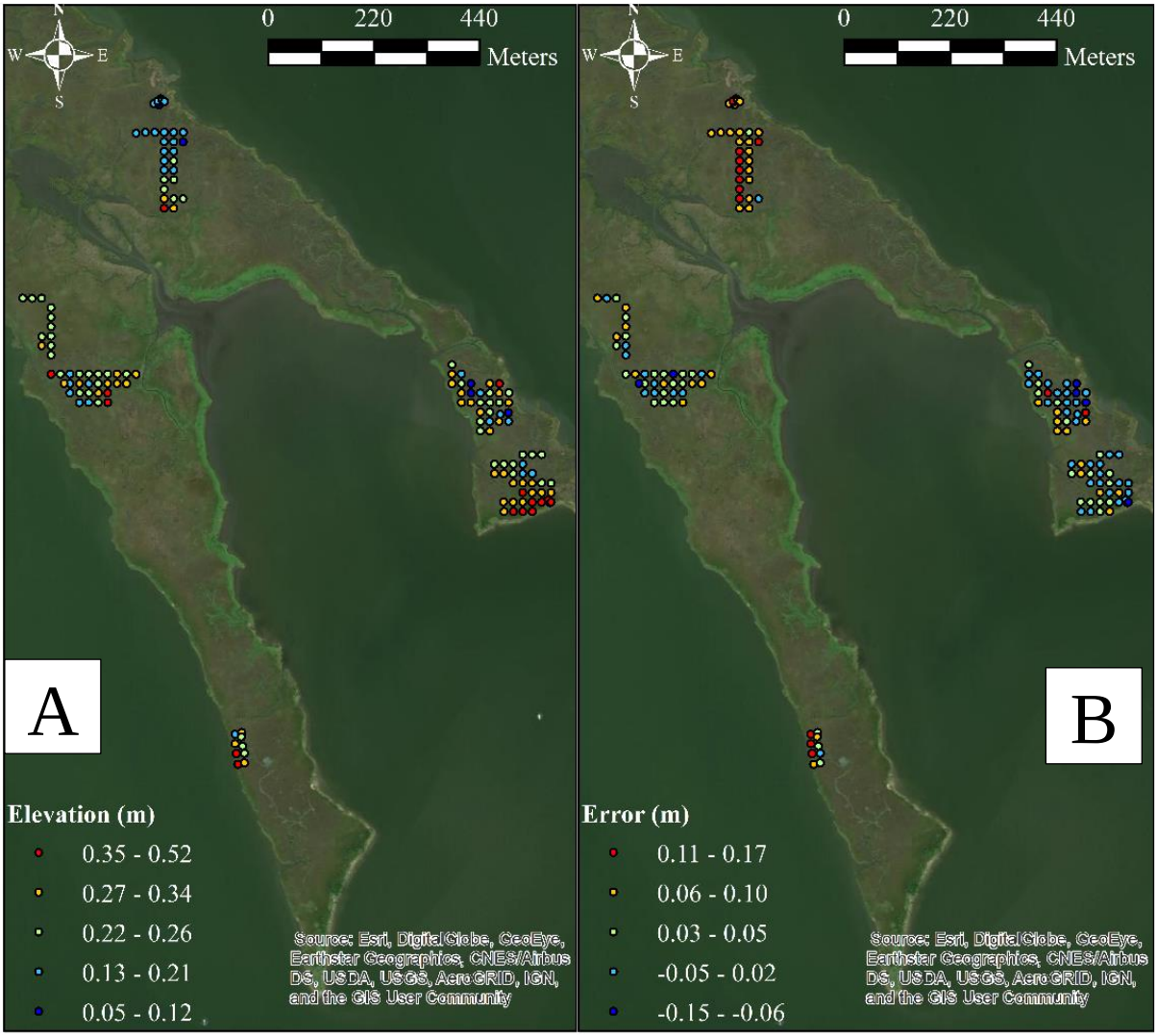

Figure 5.11. RTK elevation (A) and error (B) visualization of the 2017 RTK survey near Cocodrie, La. Error is calculated by subtracting the RTK elevation value from the DEM (2015 USGS: LA South Terrebonne, LA). Color codes distinguish six natural breaks in the data.

Table 5.5. Summary of the error found at the Cocodrie, LA Island survey area, calculated as mean error (ME), mean absolute error (MAE) and root mean square error (RMSE).

DEM	ME (m)	MAE (m)	RMSE (m)	1st Quart. (m)	3rd Quart. (m)
2011 USGS: LA Region 1	0.2	0.2	0.24	0.14	0.28
2015 USGS: LA South Terrebonne	0.03	0.04	0.07	0.006	0.07

The NAIP NDVI values from 2015 and 2011 are plotted with respect to RTK elevation in Figure 5.12. As seen in the graph, the NDVI derived from the 2015 NAIP imagery linearly correlates to elevation more than the 2011 NAIP imagery, explaining 42% of the variance. Generally, the 2015 NDVI increases approaching higher elevations. The bulk of the 2015 NDVI ranges from 0.2 to 0.4 with some extreme values breaching 0.5 at the higher elevations. On the other hand, RTK elevation only explains 6% of the 2011 NAIP NDVI variance and has barely positive relationship. Another notable difference between the NDVI datasets is the variability. Comparing the NDVIs from 2011 and 2015, the variances are 0.003 and 0.018, respectively.

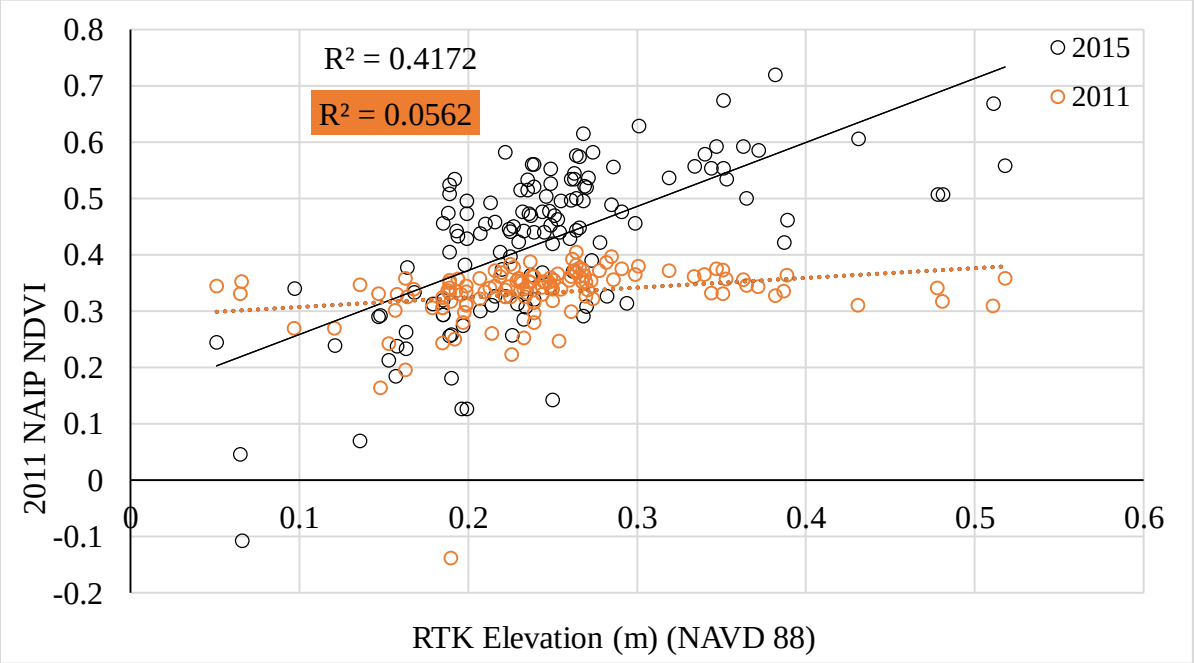

Figure 5.12. DEM error (m) versus 2011 and 2015 NAIP NDVI at the Cocodrie, LA survey site, fitted with a linear least squares (LLS) trend line.

Similar to Big Branch, DEM error in the 2015 USGS: LA South Terrebonne DEM generally decreases with increase elevation, receiving an R-squared value of 0.169 (Figure 5.13).

Most of the RTK survey is performed in the range of 0.2 to 0.3 m, and errors range from -0.07 to 0.13 m. From elevations of 0 to 0.2 m, error is above average and is positive.

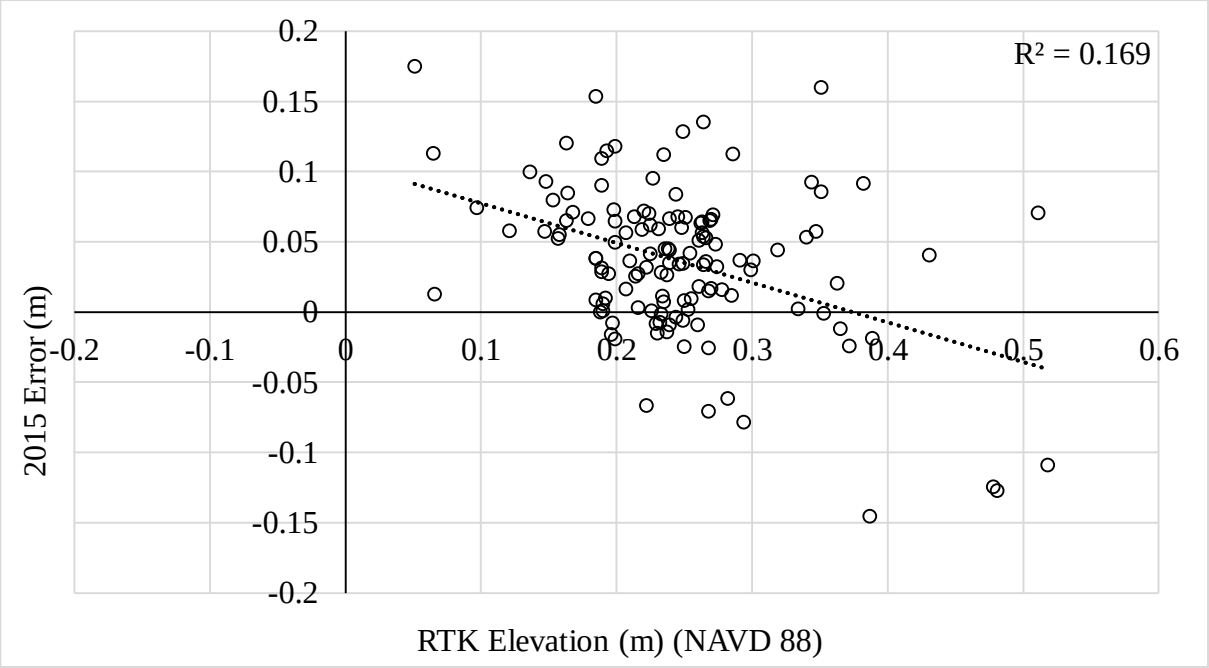

Figure 5.13. DEM error (m) versus measured 2015 RTK elevation at Cocodrie, La. Data is fitted with a linear least squares (LLS) trend line.

There is nearly no correlation between DEM error and 2015 NDVI and NDVI only explains 2% of the variance in error (Figure 5.14). Peak error occurs at an NDVI value of approximately 0.42, and most extreme negative errors occur in the range of 0.3 to 0.6. It is likely there are sources of error other than systematic vegetation offset. In this survey location, without a different data filter, it may not be possible to use NDVI as a predictor for DEM error, especially without other high resolution independent variables.

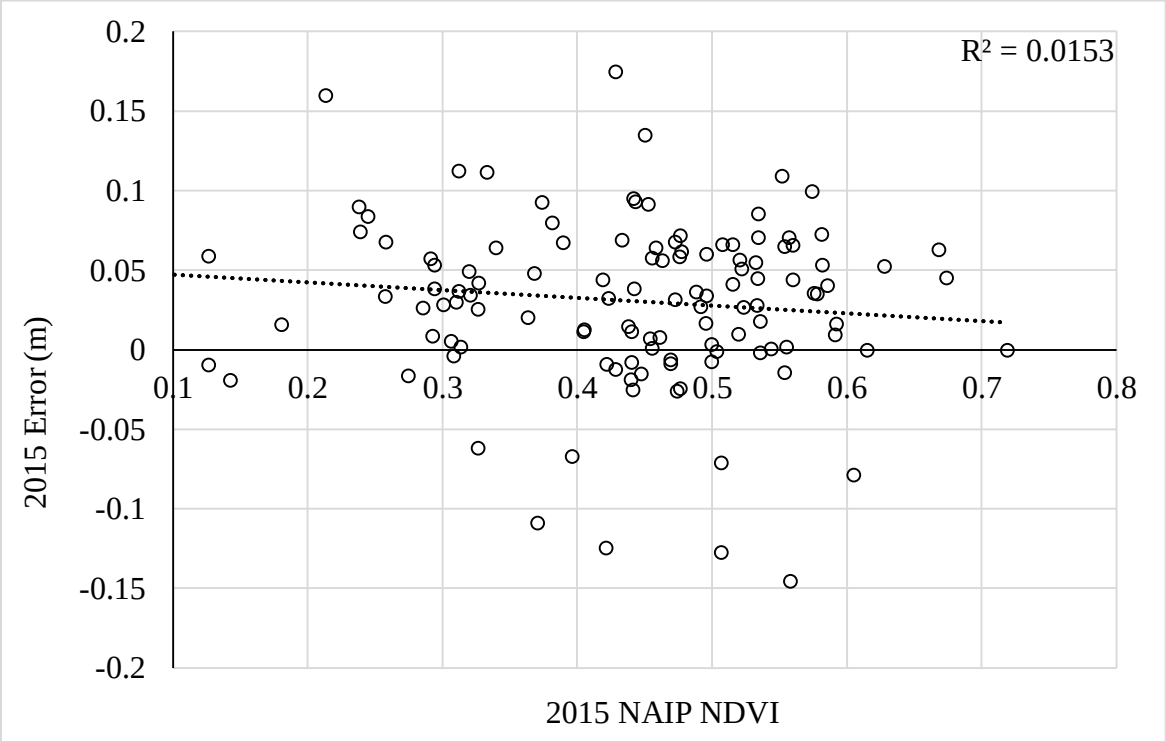

Figure 5.14. Plot showing 2015 DEM error (m) versus 2015 NAIP NDVI at the Cocodrie, La survey, fitted with a linear least squares (LLS) trend line.

5.4. Pearl River, LA Survey

DEM error at the Pearl River survey site does not show a clear spatial pattern and error ranges from -0.004 to 0.45 m (Figure 5.15). The imagery in Figure 5.15does not represent the same vegetative conditions of the time of the lidar acquisition, but the variety of colors and textures suggest this area has complex vegetative patterns which may result in complex error distributions. Larger errors are found at the south side of the survey grid 20 meters beyond the bank edge. Traversing inland, errors are less extreme but consistently stay in the range of 0.10 to 0.29 m. The mean error and mean absolute error are nearly identical, a value of 0.11 m, as only 4 points contained negative errors (Table 5.6). The root mean square error is 0.14 m, which is 2.9 times higher than the RMSE of the original lidar data set, a value of 0.049 m.

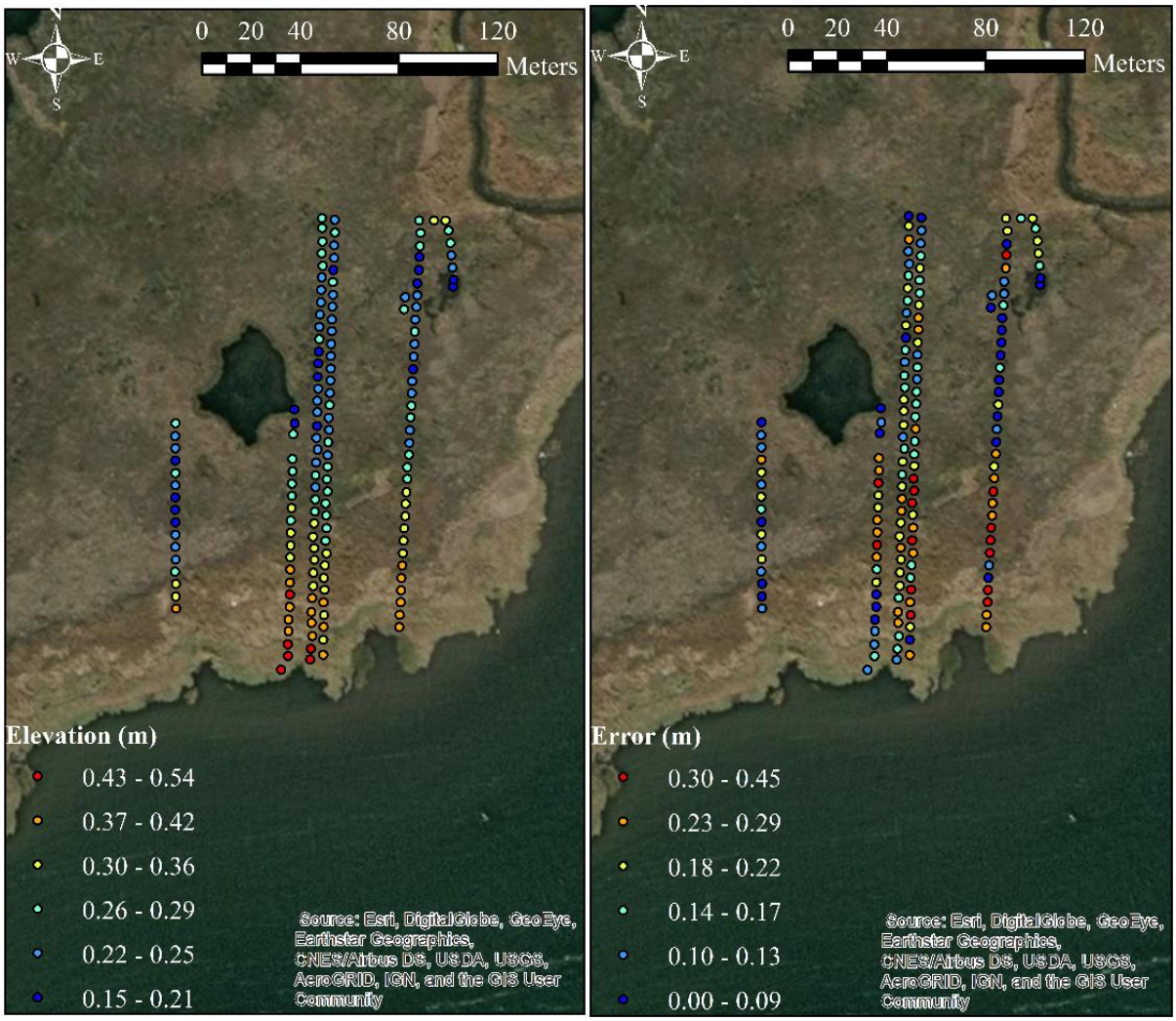

Figure 5.15. RTK elevation (left) and error (right) visualization of the 2018 RTK survey near Pearl River, La. Error is calculated by subtracting the RTK elevation value from the DEM. Color codes distinguish six natural breaks in the data.

Table 5.6. Summary of the error found at the Pearl River, La Island survey. Error statistics are calculated as mean error (ME), mean absolute error (MAE) and root mean square error (RMSE).

DEM	ME (m)	MAE (m)	RMSE (m)	1st Quart. (m)	3rd Quart. (m)
2017 USGS: Upper Delta Plain, LA	0.11	0.11	0.14	0.05	0.16

The majority of the survey occurs in vegetation whose NDVI values range from 0.4 to 0.7. Unlike the Elmer's Island survey, NAIP NDVIs do not explain very much variance with respect to error (Figure 5.16 and Figure 5.17). However, the 2016 NAIP NDVI outperforms the 2017 NAIP NDVI, and 10% of the variation is explained compared to 0.4% by the 2017 NAIP.

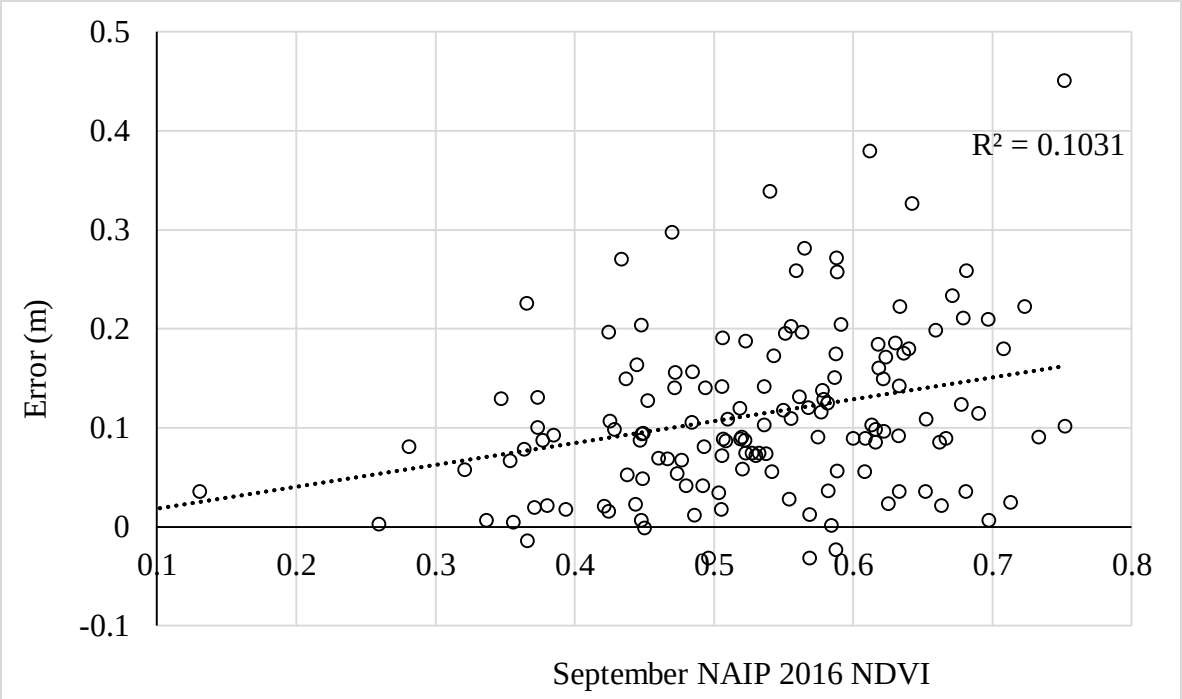

Figure 5.16. Scatter plot showing DEM error (m) at the Pearl River, La survey area versus 2016 NAIP NDVI. Data is fitted with a linear least squares (LLS) trend line.

Referencing the NAIP 2016 data, a positive relation can be found between NDVI and error. The peak error value occurs at an NDVI value of approximately 0.75, and error values decrease on average approaching the lower NDVI values.

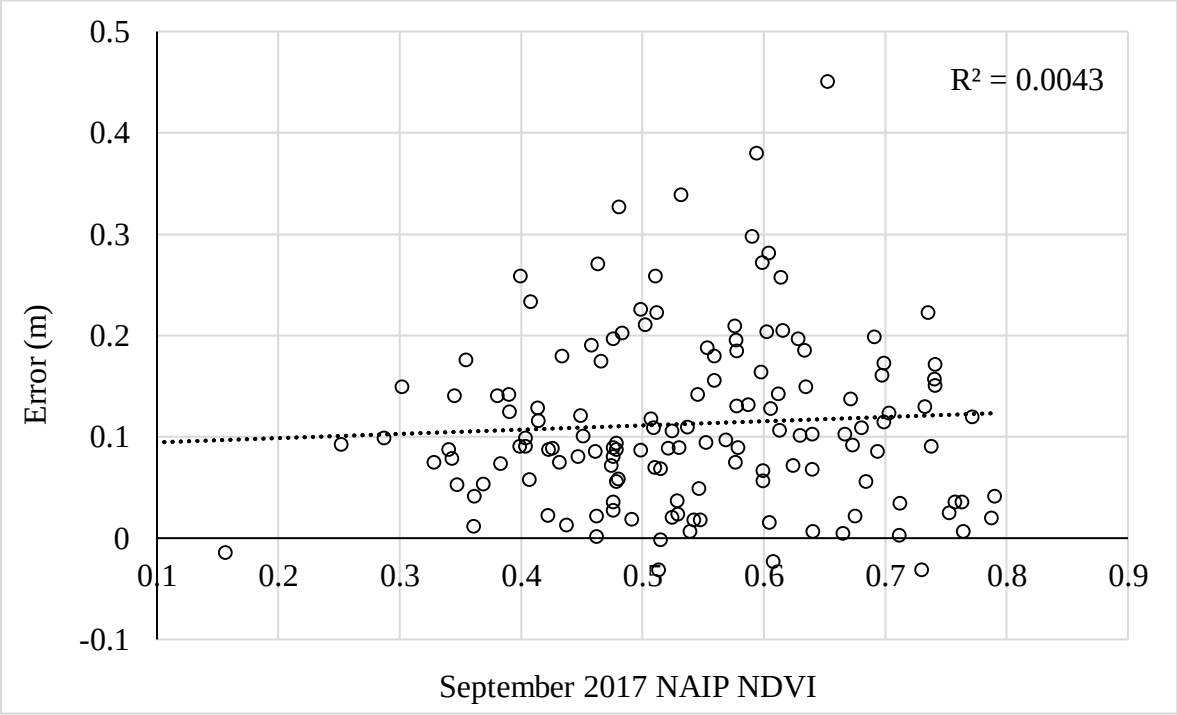

Figure 5.17. Scatter plot showing DEM error (m) at the Pearl River, La survey area versus 2017 NAIP NDVI. Data is fitted with a linear least squares (LLS) trend line.

In this intermediate marsh, RTK elevation explains 36% of the variance in the 2016 NAIP NDVI. On the other hand, 2018 RTK elevations only explains 22% of the variation in the 2017 NAIP NDVI (Figure 5.18). On average for both datasets, NDVI values of 0.4 and 0.68 correspond to elevations of 0.15 and 0.4 m, respectively. The variance of NDVI for 2016 and 2017 is similar with values of 0.015 and 0.017 m^2, respectively, using the entire dataset. At lower elevations the variance is 0.16 and 0.18 m^2. This variance is larger than variance of the entire dataset and much higher than the variance at the higher elevations, values of 0.005 and 0.01 m^2, respectively.

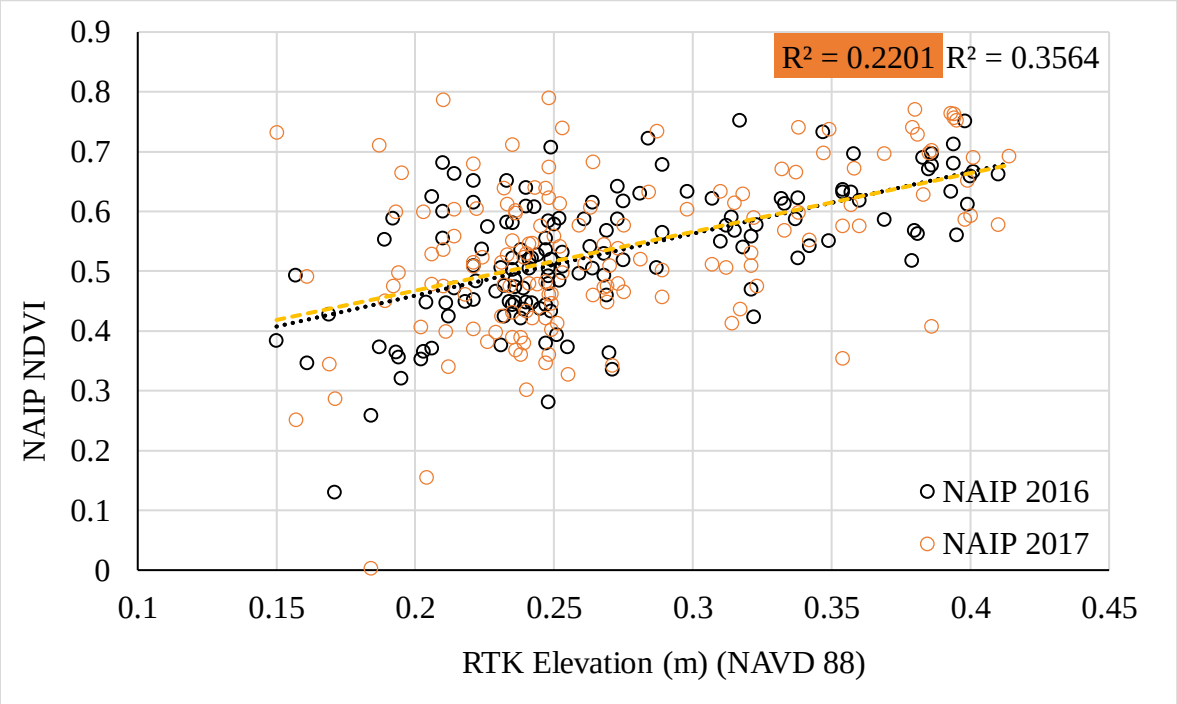

Figure 5.18. Scatter plot demonstrating the relation between 2016 NAIP NDVI (m) and measured RTK elevation (m) referencing NAVD 88 at the Pearl River survey site. Data is fitted with a linear least squares (LLS) trend line.

As expected from the NDVI and error plots, the error and elevation relationships for this site are complex. Figure 5.19 plots error with respect to RTK elevation and shows a positive correlation exists, receiving an R-squared value of 0.12. Peak error occurs at an elevation of 0.39 m. Errors in the range of 0.3 to 0.44 m are consistently above 0.10 m and average 0.16 m which is greater the average for the dataset. Error below 0.3 m elevation is within the random error range but also contains points of high error.

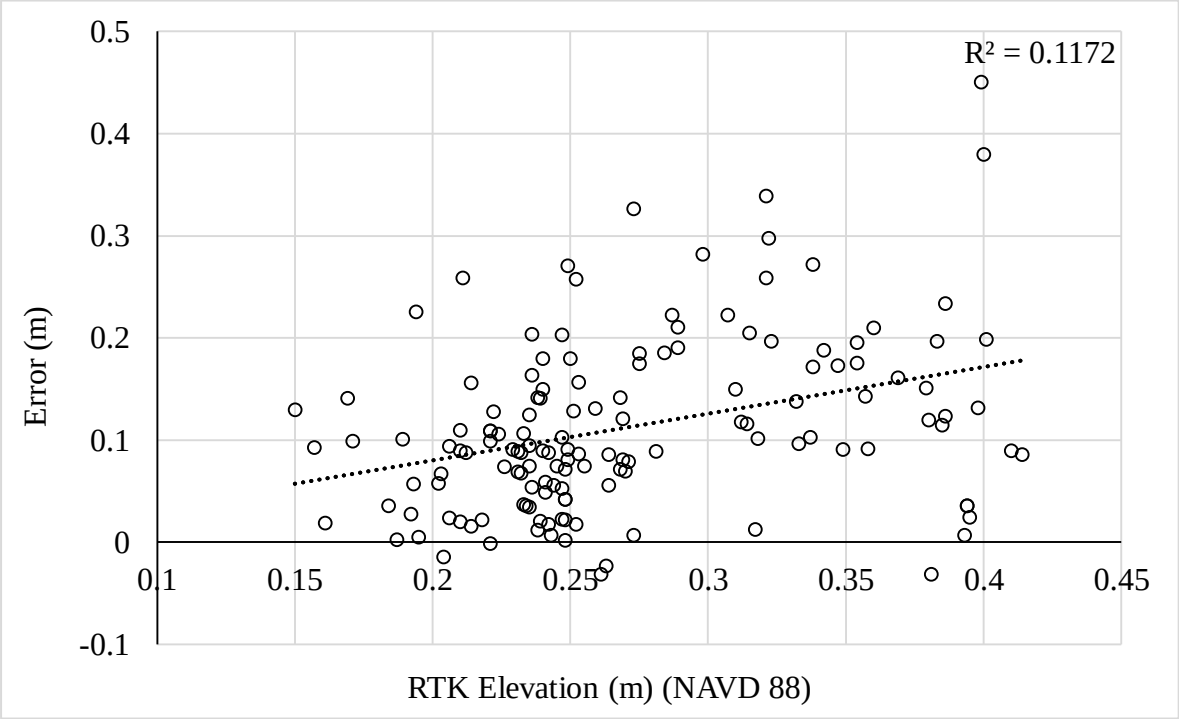

Figure 5.19. Scatter plot showing DEM error (m) versus measured RTK elevation at Pearl River, La. Data is fitted with a linear least squares (LLS) trend line.

6. Digital Elevation Model Correction

Systematic errors due to vegetation requires DEMs to be improved for accurate modeling results. As lidar accuracies have improved in both the vertical and horizontal directions, full corrections have become more achievable. This next chapter will apply three methods of DEM correction. First is optimal minimum binning; this method is the simplest and most user-friendly correction. Second is the LEAN method (discussed in Chapter 3), and the last method is a random forest error prediction model, which uses combinations of imagery-derived NDVI and lidar-derived metrics.

6.1. Optimal Minimum Binning

As discussed in Chapter 3.1, minimum binning requires a user defined grid size. In this work the target grid size is the resolution in which the root mean square error (RMSE) and/or absolute mean error is most reduced. The target grid size does not correspond to the optimal resolution of the DEM for a particular model, but rather, it is based only on the accuracy assessment with respect to the RTK measurements. Four different grid sizes were evaluated for each survey location, 2.5 m, 5 m, 7.5 m and 10 m. It is possible the most optimal grid size lies between these resolution but the differences are most likely minimal. Box and whiskers plots of the calculated error statistics for each minimum binning resolution at each survey site can be seen in Figures 6-1, 2, 3, 4 and Tables 6-1, 2, 3, 4.

6.1.1. Big Branch Wildlife Refuge

The optimal bin size at Big Branch is approximately 7.5 m. When using this resolution the positive bias (ME) is reduced to -0.01 m and the MAE is reduced to 0.04 m. The RMSE is reduced from 0.13 m to 0.05 m, which is a 62% improvement. However, as the user-defined window increases (7.5 and 10 m) more extreme negative and positive values occur (Figure 6.1). This may be due to blunders in the lidar dataset or bins being expanded beyond the marsh surface towards the water's edge.

Table 6.1. Error statistics of the minimum binning derived DEMs at Big Branch, calculated as mean absolute error (MAE), mean error (ME) and root mean square error (RMSE). The optimal bin size is highlighted in red.

	2.5 m	5.0 m	7.5 m	10.0 m	DEM
MAE (m)	0.07	0.05	0.04	0.04	0.11
ME (m)	0.07	0.03	-0.01	-0.01	0.11
RMSE (m)	0.09	0.06	0.05	0.06	0.13

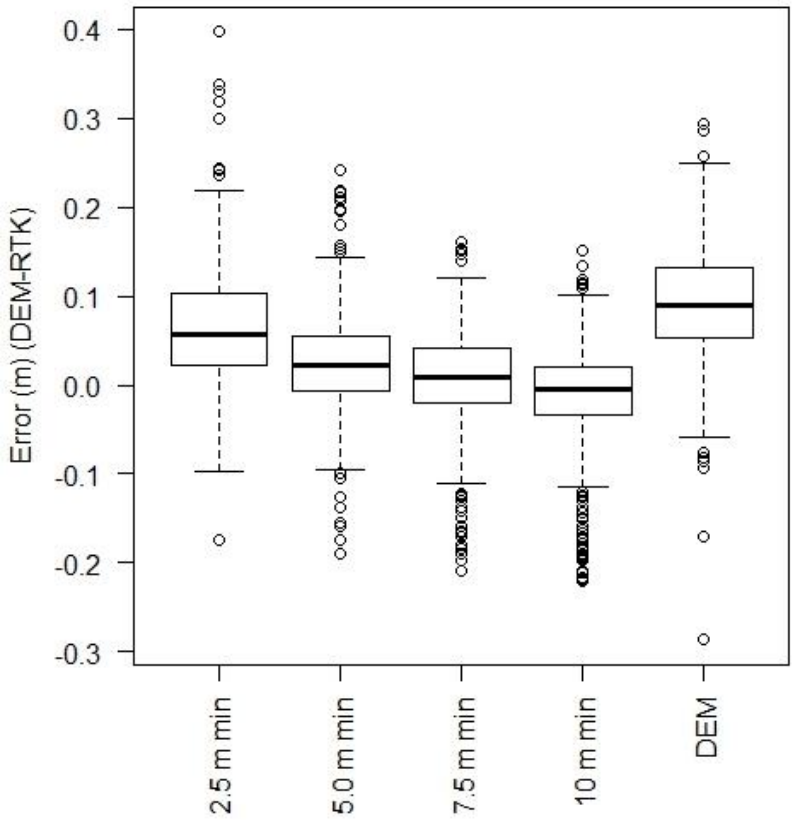

Figure 6.1. Box and whiskers plots of error at Big Branch when deriving the DEM using the minimum binning technique at resolutions of 2.5, 5.0, 7.0, and 10 m. The box represents the 25th, 50th and 75th quartiles and the whiskers (min and max) extend 1.5 times the interquartile range. The circles outside this range are beyond the 5th and 95th percentile of error.

6.1.2. Elmer's Island, LA

The optimal bin size at Elmer's Island, LA is 5.0 m (Table 6.2). When using this resolution, the positive bias (ME) is reduced to 0.01 m and the MAE is reduced to 0.06 m. The RMSE is reduced from 0.12 m to 0.09 m, which is a 25% improvement. However, as the user defined window increases to 7.5 m and 10 m, more extreme negative values occur (Figure 6.2). The negative values help reduce the mean error but decrease the accuracy for this DEM.

Table 6.2. Error statistics of the minimum binning derived DEMs at Elmer's Island, LA, calculated as mean absolute error (MAE), mean error (ME) and root mean square error (RMSE). The optimal bin size is highlighted in red.

	2.5 min	5.0 min	7.5 min	10.0 min	DEM
MAE (m)	0.08	0.06	0.07	0.08	0.1
ME (m)	0.07	0.01	-0.03	-0.05	0.1
RMSE (m)	0.11	0.09	0.1	0.12	0.12

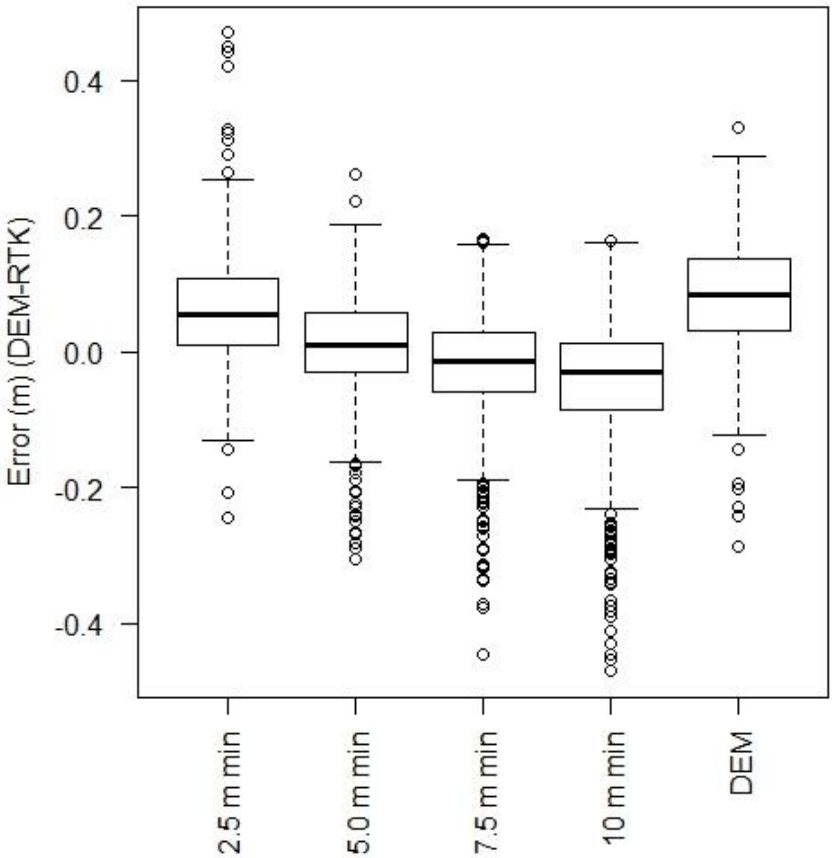

Figure 6.2. Box and whiskers plots of error at Elmer's Island when deriving the DEM using the minimum binning technique at resolutions of 2.5, 5.0, 7.0, and 10 m. The box represents the 25th, 50th and 75th quartiles and the whiskers (min and max) extend 1.5 times the interquartile range. The circles outside this range are the outliers.

6.1.3. Pearl River, LA

The optimal bin size at Pearl River, LA is 5.0 m (Table 6.3). When using this resolution, the positive bias (ME) is reduced to 0.01 m and the MAE is reduced to 0.04 m. The RMSE is reduced from 0.14 m to 0.05 m, which is a 65% improvement. The sampling of extreme values not as prevalent as compared to Elmer's Island (Figure 6.3). Considering the survey area is sloped, the introduction of negative errors is more likely because the predefined window extends to lower elevations.

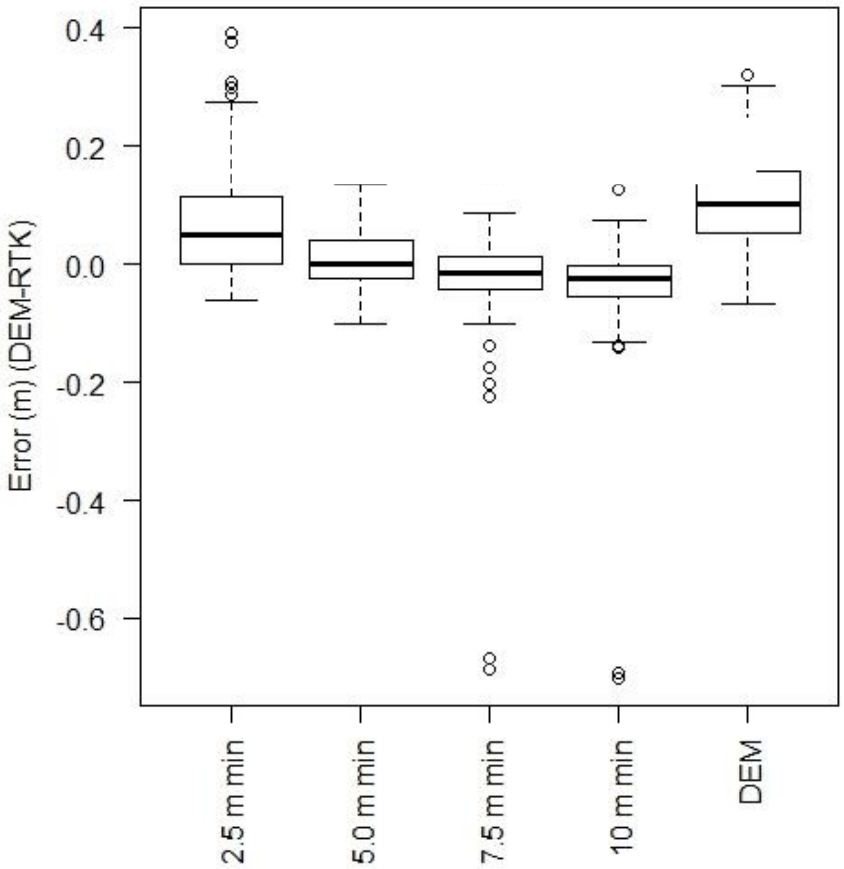

Figure 6.3. Box and whiskers plots of error at Pearl River, LA when deriving the DEM using the minimum binning technique at resolutions of 2.5, 5.0, 7.0, and 10 m. The box represents the 25th, 50th and 75th quartiles and the whiskers (min and max) extend 1.5 times the interquartile range. The circles outside this range are the outliers.

Table 6.3. Error statistics of the minimum binning derived DEMs at Pearl River, LA calculated as mean absolute error (MAE), mean error (ME) and root mean square error (RMSE). The optimal bin size is highlighted in red.

	2.5 min	5.0 min	7.5 min	10.0 min	DEM
MAE (m)	0.08	0.04	0.05	0.05	0.11
ME (m)	0.07	0.01	-0.02	-0.03	0.11
RMSE (m)	0.11	0.05	0.09	0.1	0.14

6.1.4. Cocodrie, LA

The optimal bin size at Cocodrie, LA is 2.5 m (Table 6.4). When using this resolution, the positive bias (ME) is reduced from 0.03 to 0.01 m, and the MAE is essentially the same. The RMSE is reduced from 0.07 m to 0.06 m, which is a 14% improvement. However, as the user defined window increases above 2.5 m, the error statistics began to suffer. The DEM becomes negatively biased and accuracy statistics increase. The extreme negative errors could be because of lidar points beyond the 95th percentile of certainty but are likely due to the slope of the terrain and binning points outside of the marsh platform (Figure 6.4).

Table 6.4. Error statistics of the minimum binning derived DEMs at Cocodrie, LA calculated as mean absolute error (MAE), mean error (ME) and root mean square error (RMSE). The optimal bin size is highlighted in red.

	2.5 min	5.0 min	7.5 min	10 min	DEM
MAE (m)	0.04	0.15	0.18	0.20	0.04
ME (m)	0.01	-0.15	-0.17	-0.20	0.03
RMSE (m)	0.06	0.16	0.20	0.23	0.07

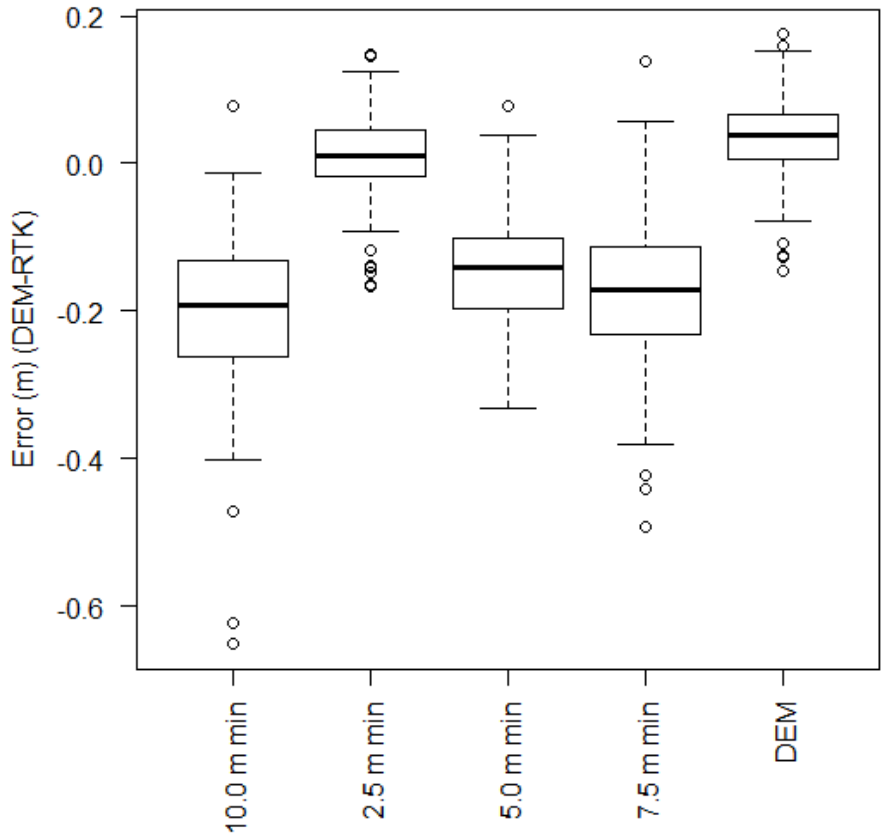

Figure 6.4. Box and whiskers plots of error at Pearl River, LA when deriving the DEM using the minimum binning technique at resolutions of 2.5, 5.0, 7.0, and 10 m. The box represents the 25th, 50th and 75th quartiles and the whiskers (min and max) extend 1.5 times the interquartile range. The circles outside this range are the outliers.

6.1.5. Optimal Minimum Binning Summary

Figure 6.5 clearly demonstrates that there is a positive offset caused by systematic error which could partly be due to vegetation. The histogram are fairly normal suggesting random error but small tails for all datasets can be seen on the right side of plot. Approaching 0 m error from the negative side there are also small tails for all the datasets. These tails suggest that extreme negative errors are not a result of random error. A histogram of the adjusted DEM using

the optimal minimum binning can be seen in Figure 6.6. Figure 6.6 shows that using the optimal minimum binning method, the positive bias of the DEM has been shifted to zero but the

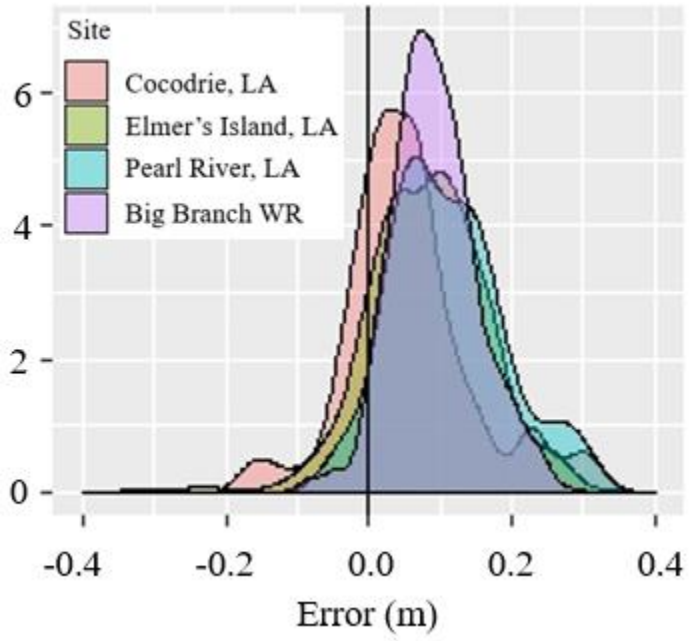

Figure 6.5. Error histograms of the unadjusted DEMs at the Cocodrie, LA, Elmer's, LA, Pearl River, LA and Big Branch survey sites.

distribution is still not normalized. For all DEMs, the MAE and RMSE have been improved; however, as a whole, a larger percentage of negative errors are introduced, and large positive errors have been reduced but still persist. Splitting the distribution below and above 0 m, the positive side of the distribution is less normally distributed as compared to the negative side. This distribution suggests that even using the lowest point within a defined grid size, systematic error caused by vegetation or other factors still influences the amount of error found and is irreducible using this technique. Using other approaches it may be possible to create a DEM that is not positively biased and more efficiently reduces the extreme positive and negative errors resulting in a distribution that is more random or normalized without the considerable tails.

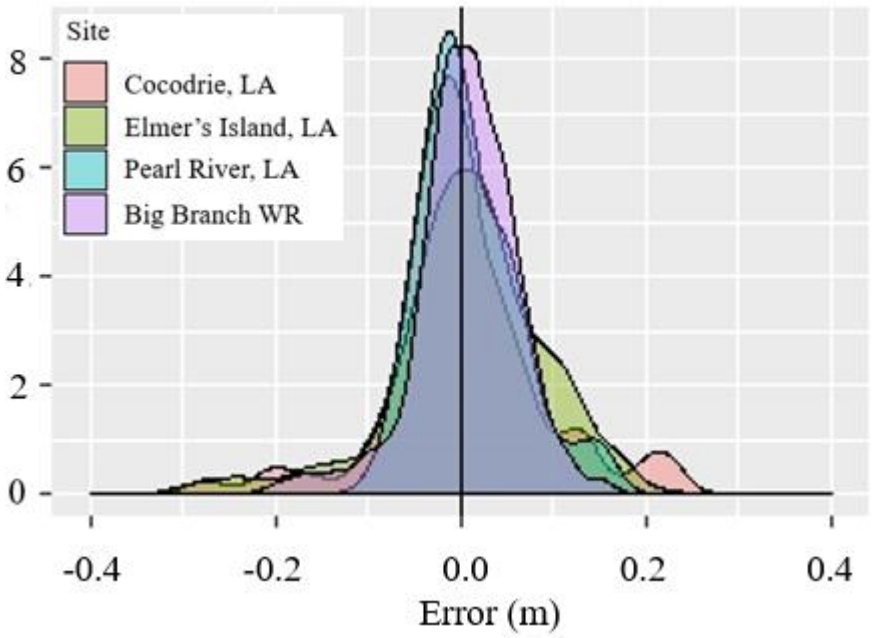

Figure 6.6. Error histograms of the optimal minimum binning DEMs at the Cocodrie, LA, Elmer's, LA, Pearl River, LA and Big Branch, LA survey sites.

6.2. Lidar Adjustment using NDVI

Elevation Adjustment with NDVI (named LEAN) uses a multi variable linear regression model to predict DEM error using NDVI and DEM elevation values as independent variables. The general equation is of the form:

$$Error = l + v + v^2 + l * v + l * v^2 + v^3 + l * v^3 \quad \text{Eq. 6.1}$$

Where l is the DEM elevation and v is the NDVI value. The Elmer's survey 1 data will be used to train a LEAN model that will be applied to the CPRA study area. This will shed light on the transferability and flexibility of the derived model and conclusions can be drawn to help determine if further steps should be used for an expansive correction in this marsh type. Also, the gridded RTK points north of Bayou Lacombe at Big Branch will be used to train a LEAN model and will be applied to the two grids south of Bayou of Lacombe. This will also give

insight to the transferability and flexibility of an error correction model but in an intermediate marsh.

6.2.1. Elmer's Island Survey 1

When applying the LEAN method to the entire Elmer's Island dataset the linear regression produced a multiple R-squared value of 0.703 and an adjusted R-squared value of 0.698, with a residual error of 0.038. The model is significant receiving a p-value of less than 2.2e-16. The significance of each independent variable can be seen in Table 6.5. The only independent variable with significance is *l*, the DEM. However, the other variables are significant when the DEM is removed from the regression, suggesting the DEM explains more variance but also a lot of the same variance in error as the other variables. Figure 6.7 shows the transformation of the unadjusted DEM to the adjusted DEM using the LEAN method. It can be seen at elevations below 0.15 m the new error adjustment under corrects the DEM, and

Table 6.5. A regression summary of the LEAN model. The independent variables are labeled as coefficients with corresponding estimates, standard error, t value, and the probability of finding any value larger or smaller than t.

Coefficients:	Estimate	Std. Error	t value	Pr(>|t|)
(Intercept)	-0.100	0.010	-9.628	<2e-16
l	0.715	0.037	19.352	<2e-16
v	-0.086	0.079	-1.091	0.276
(v^2)	-0.275	0.315	-0.872	0.383
$(l*v)$	0.027	0.304	0.090	0.928
$(l*v^2)$	0.556	0.812	0.684	0.494
(v^3)	-0.337	0.387	-0.870	0.385
$(l*v^3)$	0.594	2.141	0.277	0.782
$(l*v^3)$	0.594	2.141	0.277	0.782

at elevations above 0.2 m the DEM is over corrected. Since a linear squares regression is used for the model build, the mean error is very close to 0 m. The mean absolute error is 0.03 m and the RMSE is 0.04 m. The strong performance is only in-bag, meaning it is not likely to perform as well outside this dataset.

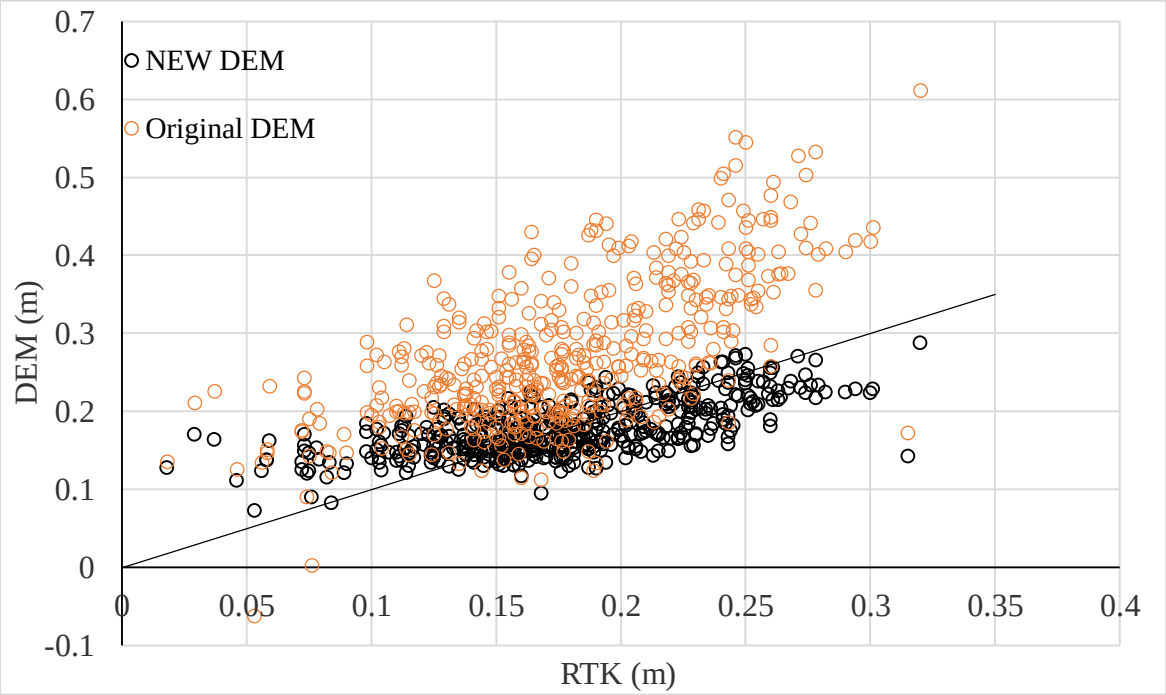

Figure 6.7. Plot of the original DEM and New DEM vs RTK values. The New DEM is the theoretical DEM produced by the correction method. A 1:1 line is indicated in black.

The model built at Elmer's Island survey 1 does not translate well to the CPRA survey site (Figure 6.8). In fact, similar to the other models, there is hard break between where the model consistently over predicts and under predicts. This break seems to be at an elevation of approximately 0.25 m. At RTK elevations beyond 0.4 m the DEM was overcorrected, creating a negative bias. Even with the over and under predictions, the accuracies of the DEM were improved (Table 6.6). The mean error was reduced from 0.17 m to 0.06 m. The mean absolute error and root mean square error were reduced to 0.13 m and 0.19 m, which is an improvement

of 33% and 25% respectively.

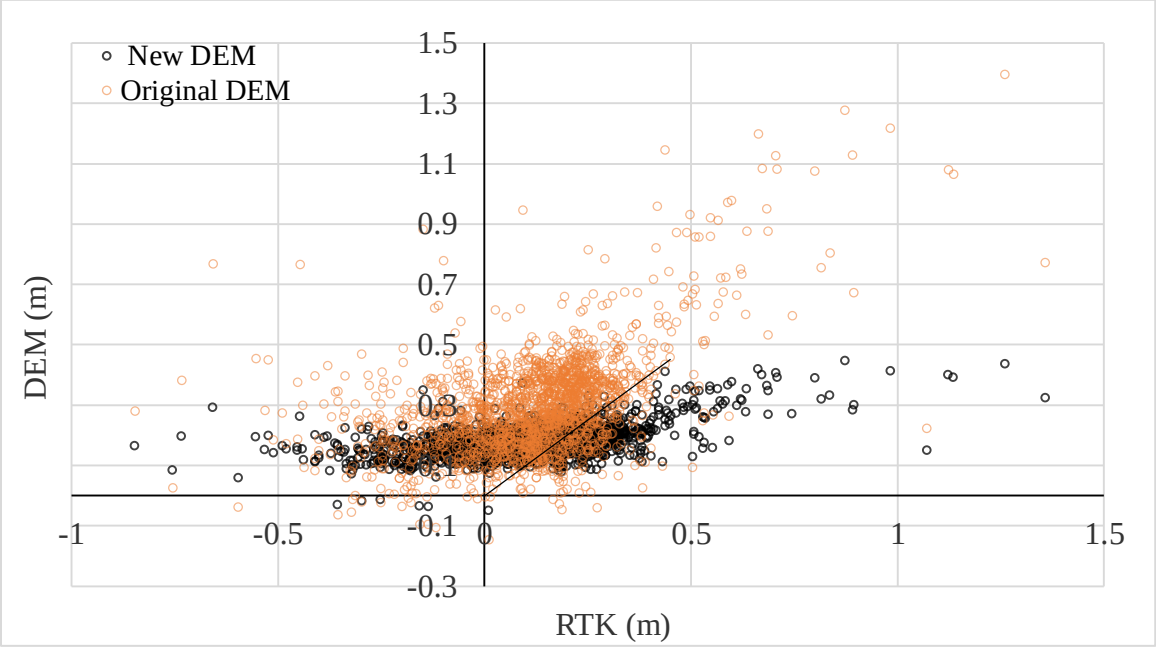

Figure 6.8. Plot of the original DEM and New DEM vs RTK values at the CPRA survey site. A 1:1 line is indicated in black.

Table 6.6. Overall error statistics of the new DEM at the CPRA RTK survey area. Statistics calculated as mean error (ME), mean absolute error (MAE) and root mean square error (RMSE). The percent improvement of the adjusted DEM can be seen in the last row.

	Mean Error (m)	MAE (m)	RMSE (m)
New DEM	0.06	0.13	0.19
Original DEM	0.17	0.19	0.25
% Improvement	--------	33%	25%

6.2.2. Elmer's Island Survey 1 error model applied to CPRA

The results were examined for each class individually. Filtering the RTK survey points using the NAIP imagery derived vegetation class, it can be seen where the LEAN method is performing the best (Table 6.7). For all classes, accuracies improved. Mean errors of all classes

were reduced for all classes, but class 8 was reduced too much, giving a mean error value of -0.17 m. As expected, the pure marsh classes (class 3 and 5) performed the best. The MAE and RMSE of class 3 were reduced by 0.05 m and 0.06 m, respectively. These are improvements of 34% and 27%, respectively. Class 5 performed the best with MAE and RMSE reaching percent improvements of 39% and 30%, respectively. It makes sense that LEAN model does not perform as well in these other classes because the correction model was not trained in those classes.

Table 6.7. Errors statistics based on the classes distinguished by the NAIP imagery, calculated as mean error (ME), mean absolute error (MAE) and root mean square error (RMSE). The percent improvement for each statistic of each class is highlighted in red.

Mean Error (m)	Class 1 (225 pts)	Class 2 (101 pts)	Class 3 (723 pts)	Class 5 (783 pts)	Class 8 (27 pts)
New DEM	0.17	0.13	0.06	0.04	-0.17
Original	0.23	0.19	0.15	0.17	0.19
MAE (m)	Class 1	Class 2	Class 3	Class 5	Class 8
New DEM	0.21	0.18	0.12	0.11	0.18
Old DEM	0.25	0.24	0.18	0.18	0.22
% Improvement	16%	25%	34%	39%	19%
RMSE (m)	Class 1	Class 2	Class 3	Class 5	Class 8
New DEM	0.27	0.25	0.17	0.16	0.24
Original	0.34	0.31	0.23	0.23	0.29
% Improvement	20%	20%	27%	30%	18%

6.2.3. Big Branch north survey grid

When applying the LEAN method to Big Branch (northern survey grid) the linear regression produced a multiple R-squared value of 0.502 with a residual error of 0.045. The independent variables and the significance of each variable can be seen in (Table 6.8). None of

the variables were considered significant however the overall model is significant with a p-value of less than 2.2e-16 (Table 6.8). When the independent variable (*l*), is removed from the regression other variables become significant, meaning there is multicollinearity between variables. Similar to the Elmer's Island model, the LEAN method consistently over estimates error beyond elevations of approximately 0.15 m and underestimates error at elevations below RTK elevations of 0.15 m (Figure 6.9). As expected the mean error is approximately 0 m. The mean absolute error is 0.034 m and the RMSE is 0.044 m.

Table 6.8. A regression summary of the LEAN model. The independent variables are labeled as coefficients with corresponding estimates, standard error, t value, and the probability of finding any value larger or smaller than t.

Coefficients:	Estimate	Std. Error	t value	Pr(>|t|)
(Intercept)	6.845	5.351	1.279	0.202
l	-13.506	15.96	-0.85	0.398
v	-48.405	34.349	-1.41	0.16
$l*v$	100.919	102.665	0.983	0.326
v^2	110.359	73.019	1.511	0.131
$l*v^2$	-232.33	218.619	-1.06	0.289
v^3	-82.283	51.418	-1.6	0.11
$l*v^3$	174.064	154.14	1.129	0.259

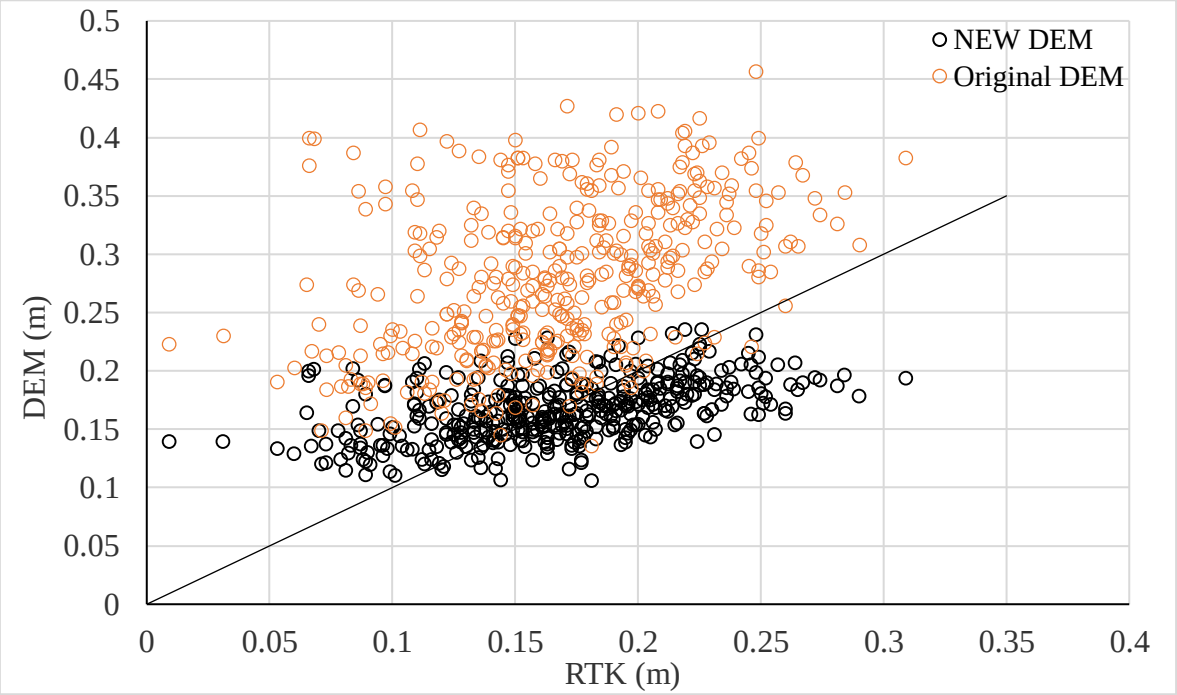

Figure 6.9. Plot of the original DEM and New DEM vs RTK values for Big Branch. A 1:1 line is indicated in black.

6.2.4. Extrapolation of Big Branch model

The model produced in section 6.2.2 is used to predict error at the two survey grids south of Bayou Lacombe. The new DEM versus the RTK elevations can be seen in Figure 6.10. Between the elevation ranges of 0.012 m and 0.2 m the model does a very good job at correcting the error. However, this portion of the dataset has the lowest amount of error. Between the elevations of 0.2 m and 0.3 m the model over predicts the error adjustment, leading to a negatively biased DEM. Beyond the elevation of 0.30 m the model performs very poorly. All errors are extremely overcorrected, leading to a negative-bias in the DEM. Overall, the model does reduce the ME, MAE and RMSE. The MAE and RMSE are reduced to 0.06 m and 0.12 m,

an improvement of 60% and 29%, respectively (Table 6.9).

Table 6.9. Overall error statistics of the new DEM at the two southern grids located at the Big Branch survey area. Statistics calculated as mean error (ME), mean absolute error (MAE) and root mean square error (RMSE). The percent improvement of the adjusted DEM can be seen in the last row.

	ME (m)	MAE (m)	RMSE (m)
New DEM	-0.02	0.06	0.12
Original DEM	0.14	0.15	0.17
% Improvement	----	60%	29%

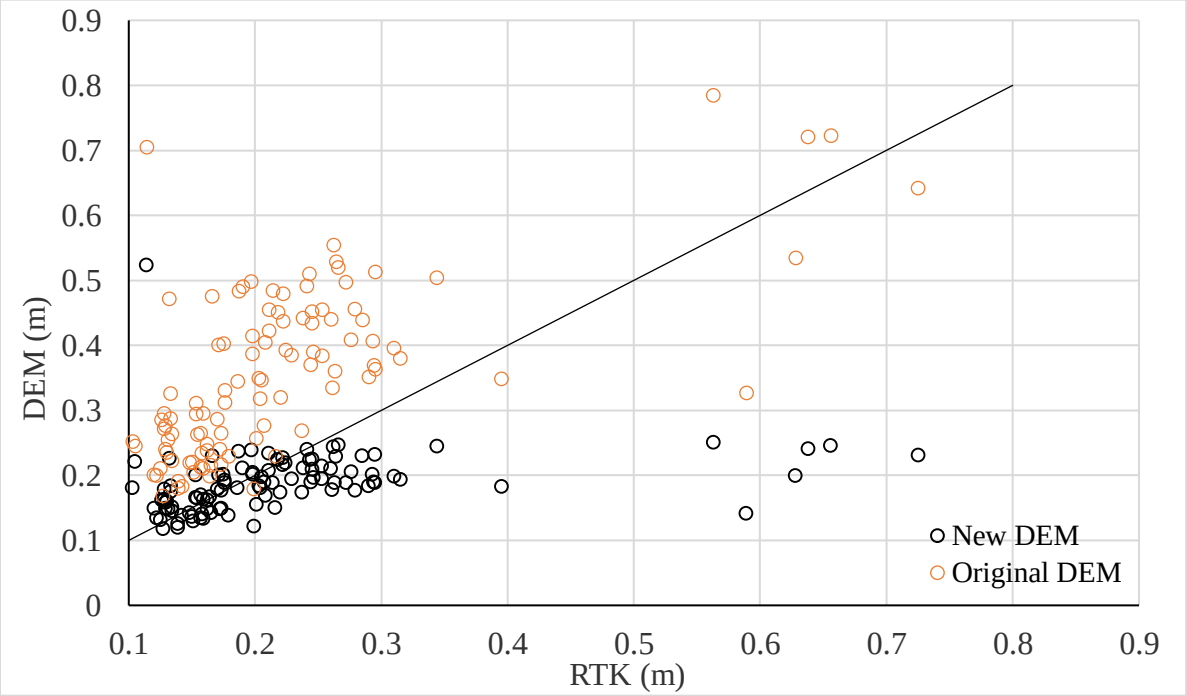

Figure 6.10. Plot of the original DEM and New DEM vs RTK values at the two southern grids located at Big Branch survey site. A 1:1 line is indicated in black.

6.2.5. Pearl River, LA

For Pearl River, LA site two error correction models were created. The first used the 2016 NDVI data (Figure 6.11), and the second used the 2017 NDVI data (Figure 6.12). Unexpectedly,

the two models performed very similar to each other. The 2016 model received in R-squared value of 0.8003, and the 2017 model received an R-squared value of 0.8301. For both models the mean error is very close to 0 m. The 2016 model has MAE and RMSE values of 0.029 m and 0.38 m. The 2017 model has MAE and RMSE values 0.027 m and 0.035 m, respectively. Both plots indicate that the extreme errors are reduced (e.g. orange dots above the 1:1 line), but the models under perform at the extremes of the RTK elevations. Above elevations of 0.3 m the error prediction is too high, resulting a DEM that is below the RTK value. On the other end, below the 0.25 m the model under predicts the error resulting in a positively biased DEM. Similar to the other models, the prediction power is spread amongst the independent variables (Table 6.10).

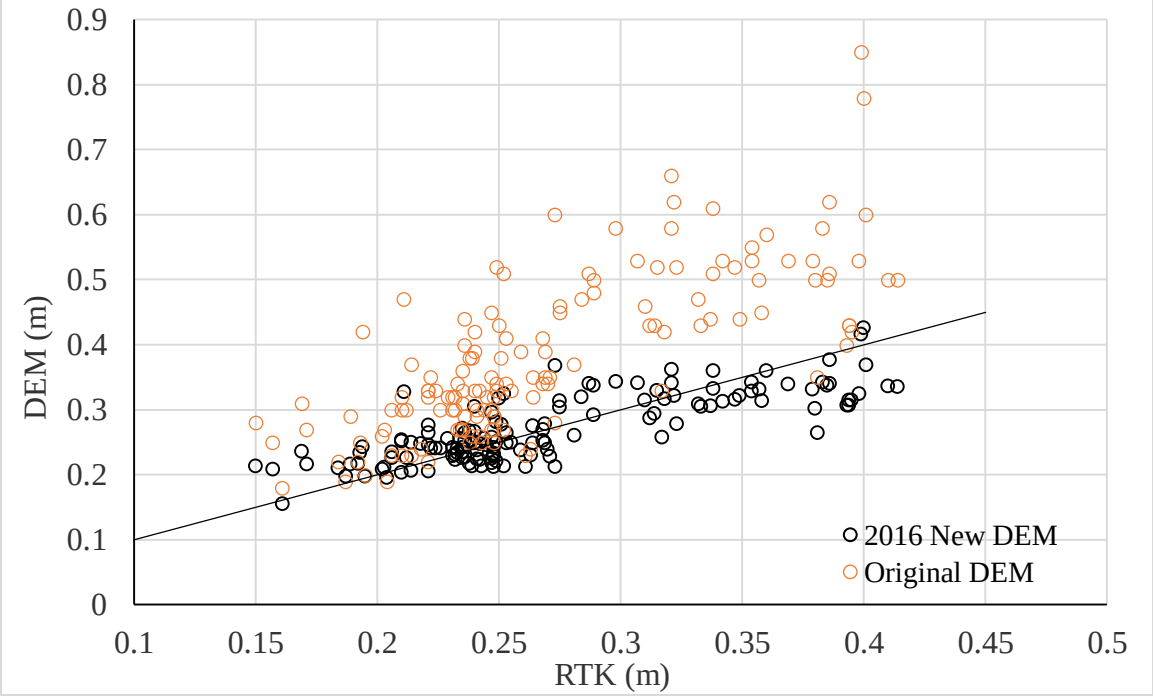

Figure 6.11. Plot of the original DEM and new 2016 derived DEM vs RTK values for Pearl River, LA. A 1:1 line is indicated in black.

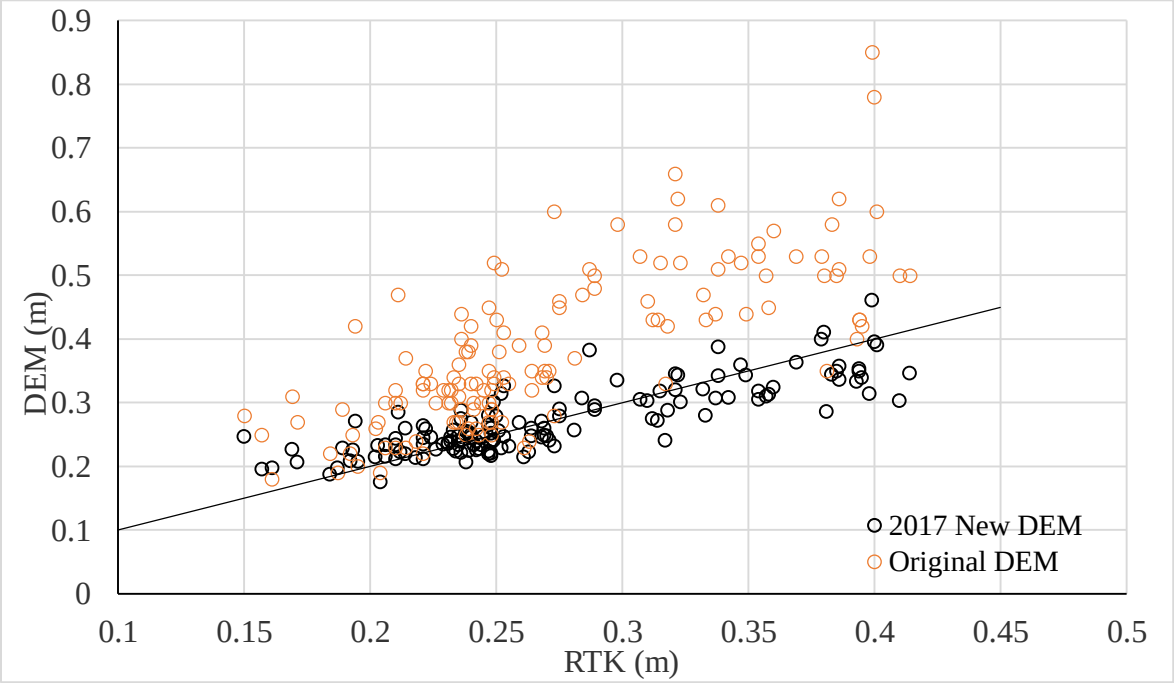

Figure 6.12. Plot of the original DEM and new 2017 derived DEM vs RTK values for Pearl River, LA. A 1:1 line is indicated in black.

Table 6.10. A regression summary of the 2017 LEAN model at Pearl River, LA. The independent variables are labeled as coefficients with corresponding estimates, standard error, t value, and the probability of finding any value larger or smaller than t.

Coefficients:	Estimate	Std. Error	t value	Pr(>|t|)
(Intercept)	-0.305	0.305	-1.000	0.319
l	1.533	1.382	1.109	0.269
v	1.645	1.755	0.937	0.350
*l*v*	-6.863	7.795	-0.880	0.380
v^2	-4.393	3.414	-1.287	0.200
$l*v^2$	17.030	14.496	1.175	0.242
v^3	3.495	2.210	1.581	0.116
*l*v*3*	-13.292	8.871	-1.498	0.136

6.2.6. Cocodrie, LA

The model build at Cocodrie, LA is not near as successful as the other model builds. The regression received an R-squared value of 0.16, only explaining 16% of the variance of the error. However, the model is significant receiving a p-value of 0.003 (Table 6.11). The DEM was the most significant independent variable with a p-value of 0.052. New error statistics are reduced with a ME, MAE and RMSE of 0.0 m, 0.035 m, and 0.047 m, respectively. As seen in Figure 6.13, the model under corrects the DEM up to the elevations of 0.2 m. At the extreme values, beyond 0.3 m, the negative errors are made worse using the LEAN correction.

Table 6.11. A regression summary of the 2017 LEAN model at Cocodrie, LA. The independent variables are labeled as coefficients with corresponding estimates, standard error, t value, and the probability of finding any value larger or smaller than t.

Coefficients:	Estimate	Std. Error	t value	Pr(>|t|)
(Intercept)	-0.177	0.105	-1.684	0.095
l	1.434	0.731	1.962	0.052
v	-0.253	0.439	-0.576	0.565
$l*v$	-2.691	3.978	-0.676	0.500
v^2	2.594	1.867	1.389	0.167
$l*v^2$	-2.170	8.753	-0.248	0.805
v^2	-3.217	2.239	-1.436	0.153
$l*v^3$	6.053	6.912	0.876	0.383

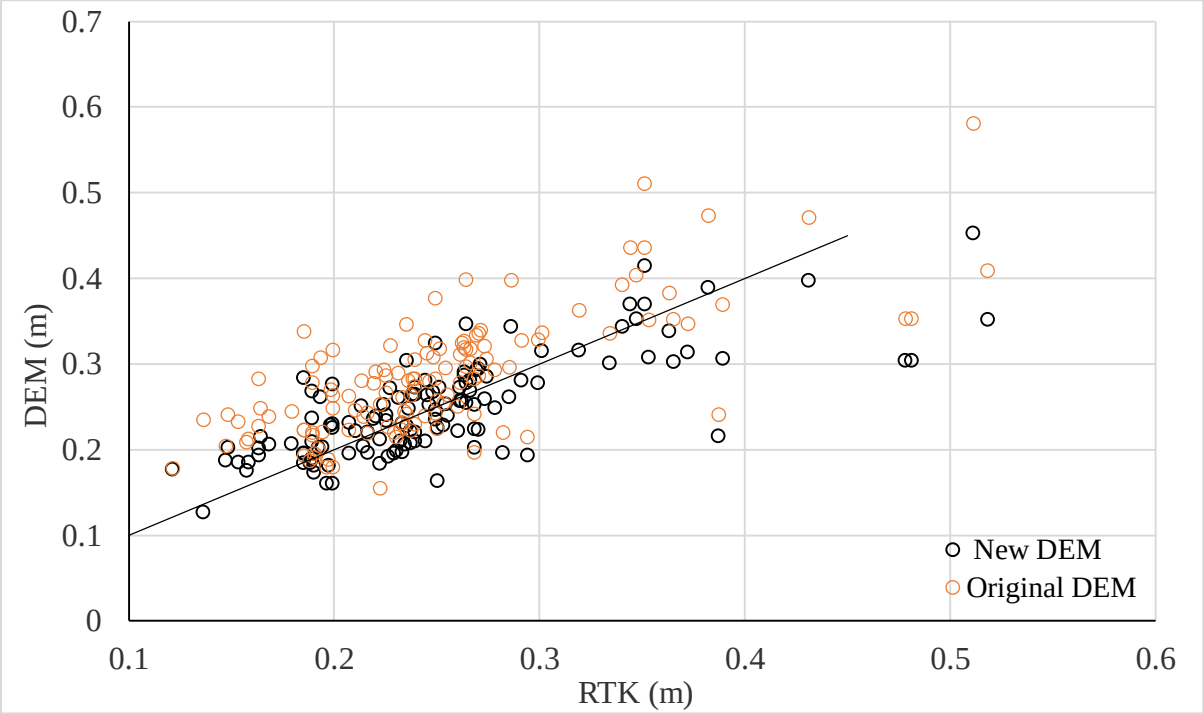

Figure 6.13. Plot of the original DEM and new derived DEM vs RTK values for Cocodrie, LA. A 1:1 line is indicated in black.

6.3. Random Forest Error Prediction Model

The random forest models use a combination of lidar-derived rasters, such as minimum, maximum and average elevation as well as remote sensing parameters, similar to the work by Cooper, Davis, and Troxler (2019). The first model was trained at Elmer's Island survey 1 and tested on the CPRA RTK survey area, similar to section 6.2.1.1. The other model was trained using the Big Branch north grid and tested on the two Big Branch grids south of Bayou Lacombe, similar to section 6.2.1.1. For both sites, a combination of variables were used to build a model that explains the highest percentage of variance. Once this model was established it was then applied outside of the training data.

6.3.1. Elmer's Island Random Forest

Five different model builds for Elmer's Island survey 1 can be seen in Table 6.12. Only three models outperformed the same combination of variables used for the LEAN method (model #2). Using a combination of lidar-derived metrics and NAIP-derived NDVI, higher variance could be explained, as in models #3, #4, and #5. The highest performing model is model #5, explaining 62.08% of the variance. This model is used to extrapolate relations to the CPRA survey area, which uses NDVI, (DEM*NDVI), minimum bin, maximum bin and average bin as independent variables. This is 8% less then what the LEAN method explained.

Table 6.12. A list of independent variables used in a random forest model build at Elmer's Island survey 1. The performance of the build is based on the mean square error (MSE) and the percentage of variance explained (% Var explained). Min, Max and Average (Avg.) rasters are derived using a resolution of 4 m.

Model #	Independent Variables	MSE	% Var explained
1	*LEAN*	0.007	58.21
2	*LEAN, Min, Max, Avg.*	0.002	59.45
3	*l*v, Min, Max, Avg.*	0.00197	60.92
4	*v, Min, Max, Avg.*	0.00192	61.83
5	*v, l*v, Min, Max, Avg.*	0.00191	62.08

The error statistics of the applied correction can be seen in Table 6.13. Overall, the accuracy of the DEM was improved. Mean absolute error and root mean square error were reduced by 0.07 m and 0.07 m, respectively. These are improvements of 36% and 28%, respectively. The mean error was also reduced from 0.17 m to 0.06 m. Classes 3, 5 and 8 performed the best receiving RMSE improvements of 29%, 37% and 33%. Class 1 and 2 still remain the most positively biased with mean errors of 0.16 m and 0.11 m, respectively. By percentage, Class 1 and 2 also have the least amount of RMSE improvement with values of 19% and 20%, respectively.

Table 6.13. Errors statistics based on the classes distinguished by the NAIP imagery, calculated as mean error (ME), mean absolute error (MAE) and root mean square error (RMSE). The percent improvement for each statistic of each class is highlighted in red. The overall statistics of the correction can be seen in the last column.

Mean Error (m)	Class 1	Class 2	Class 3	Class 5	Class 8	Overall
New DEM	0.16	0.11	0.05	0.04	0.01	0.06
Original	0.23	0.19	0.15	0.17	0.19	0.17
MAE (m)	Class 1	Class 2	Class 3	Class 5	Class 8	Overall
New DEM	0.20	0.18	0.11	0.10	0.13	0.12
Old DEM	0.25	0.23	0.18	0.18	0.22	0.19
% Improvement	21%	25%	39%	44%	41%	37%
RMSE (m)	Class 1	Class 2	Class 3	Class 5	Class 8	Overall
New DEM	0.27	0.24	0.16	0.14	0.20	0.18
Original	0.34	0.31	0.23	0.23	0.29	0.25
% Improvement	18%	23%	30%	39%	31%	28%

6.3.2. Big Branch Random Forest

Six different model builds can be seen in Table 6.14. Every model build outperforms the same combination of variables used for the LEAN method (model #1). Using a combination of lidar derived metrics and NAIP derived NDVI, higher variance could be explained, models #2, #3, #4 and #5. The final model uses a combination of lidar-derived metrics and LEAN parameters including: vegetation height (Hgt.), maximum, minimum and average rasters as well as the all the LEAN parameters derived with Sentinel 2 imagery. This model explains 58.27% of

the variance in error for the training set. This is 8% more then what the LEAN method explains using a linear regression.

Table 6.14. A list of independent variables used in a random forest model build at Big Branch's north survey grid. The performance of the build is based on the mean square error (MSE) and the percentage of variance explained (% Var. explained). Min, Max and Average (Avg.) rasters are derived using a resolution of 4 m. **Parameter is derived with Sentinel imagery (9/10/16)

Model #	Independent Variables	MSE	% Var. Explained
1	*LEAN*	0.0022	44.03
2	*LEAN, Max, Min, Avg.*	0.0019	52.8
3	*lv, v^2, v^3, Max, Avg.*	0.0018	53.9
4	*Avg., Min, lv, v^2, v^3, Max*	0.0018	55.33
5	*LEAN, v**, Hgt., Max, Min, Avg.*	0.0017	57.46
6	*LEAN**, Hgt., Max, Min, Avg.*	0.0017	58.27

The performance of model #6 applied to the southern survey grids can be seen in Table 6.15. Overall, the accuracy of the DEM is improved. Mean absolute error and root mean square error were reduced by 0.09 m and 0.08 m, respectively. These are improvements of 60% and 47%, respectively. The mean error was reduced to -0.01 m, meaning some negative bias was introduced in the new DEM. For marshes whose vegetation can change drastically year to year and the variance in error is not well explained by NDVI, it may be necessary to use other metrics to correct DEMs.

Table 6.15. Overall error statistics of the new DEM at the two southern grids located at the Big Branch survey area using random forest model #6. Statistics are calculated as mean error (ME), mean absolute error (MAE) and root mean square error (RMSE). The percent improvement of the adjusted DEM can be seen in the last row.

	ME (m)	MAE (m)	RMSE (m)
New DEM	-0.01	0.06	0.09
Old DEM	0.14	0.15	0.17
% Improvement	---	60%	47%

The LEAN method and random forest model can be further broken down by vegetation classes at the CPRA site as seen in Table 6.16. The optimal random forest model outperforms LEAN in both accuracy statistics for all cover classes. However, the mean error for both classes 1 and 2 is better for the LEAN method. The major improvements from the LEAN to the random forest model are in classes 5 and 8. Both statistical accuracy assessments are improved and the mean error is also improved.

Table 6.16. A comparison of the LEAN method and optimal random forest (RF) model extrapolated to the CPRA RTK survey area. The statistics are broken down by the cover classes. The percent improve for each statistics is colored red.

		Class 1		Class 2		Class 3		Class 5		Class 8	
Stat		LEAN	RF	LEAN	RF	LEAN	RF	LEAN	RF	LEAN	RF
ME (m)	New Dem	0.07	0.16	0.03	0.11	-0.05	0.05	-0.06	0.04	-0.17	0.01
	Original	0.23	0.23	0.19	0.19	0.15	0.15	0.17	0.17	0.19	0.19
RMSE (m)	New Dem	0.27	0.27	0.25	0.24	0.17	0.16	0.16	0.14	0.24	0.20
	Original	0.34	0.34	0.31	0.31	0.23	0.23	0.23	0.23	0.29	0.29
	% Imp	**18%**	**18%**	20%	23%	**26%**	**30%**	30%	39%	**17%**	**31%**
MAE (m)	New Dem	0.21	0.20	0.18	0.18	0.12	0.11	0.11	0.10	0.18	0.13
	Original	0.25	0.25	0.24	0.24	0.18	0.18	0.18	0.18	0.22	0.22
	%Imp	**16%**	**21%**	25%	25%	**33%**	**39%**	39%	44%	**19%**	**41%**

7. Discussion and Recommendations

7.1. Ecological Influences of Error

As discussed in section 2.2.1, the intensity of a lidar beam reflection can depend on many factors, one of which is the type of surface the beam is encountering. Since most discrete lidar systems use wavelengths in the near infrared zone, which is known to be highly reflected by healthy vegetation (Slaton, Raymond Hunt Jr, & Smith, 2001), the intensity of reflectance should change depending on vegetative characteristics (Merzlyak, Chivkunova, Melø, & Naqvi, 2002). These characteristics tend to vary across the marsh surface as a function of edaphic conditions (nutrients, salinity, sulfide concentrations, lower redox potential), all of which can be temporally variable (Bertness & Ellison, 1987; Byrd & Kelly, 2006; Mendelssohn, McKee, & Patrick, 1981; Mitsch & Gosselink, 1993). In theory these conditions should maximize the uniqueness of a waveform return (Rogers, Parrish, Ward, & Burdick, 2018). This logic supports the work by (Rosso, Ustin, & Hastings, 2006; Schmid et al., 2011), who roughly estimate lidar error as half the vegetation height and have shown that lidar errors are generally larger with increasing vegetation height and vegetation density. Counterintuitively, the results from the four surveys presented here have very similar accuracy assessments, despite inhabiting different vegetation types. Some of this similarity may be due to averaging errors across RTK points and the number of points measured within the varying vegetation types. When parsing the survey by certain vegetation characteristics and errors beyond the 3rd quartile, it can be determined that many of these similarities can be explained by the variations in plant structure, height and biomass. It also shows that the capabilities of lidar technology minimize the window in which errors may exist, producing a more common outcome.

7.1.1. Homogeneous stands

When comparing the Elmer's Island site to the Big Branch site, the errors at the 3rd quartile are exactly the same, a value of 0.14 m. At Elmer's Island the majority of errors beyond the 3rd quartile are associated with very productive *Spartina alterniflora* and black mangrove and are in the range of 0.14-0.32 m. At Big Branch, the errors beyond the 3rd quartile are associated with *Spartina patens* located at the higher elevations. Despite being a shorter plant, usually in the range of 30-60 cm, *Spartina patens* produces proportionally as much error as the much taller species *Spartina alterniflora* (heights of >100 cm). Comparing the error range to the height of *Spartina patens*, it can be determined that very little penetration occurs in Spartina patens as compared to Spartina alterniflora. It has been documented that *Spartina patens* in Louisiana usually has higher biomass levels than *Spartina alterniflora*, but these levels can vary depending on the time of year and marsh type. Some studies have shown that *Spartina patens* can have nearly twice the biomass as *Spartina alternifora* with total above ground biomasses levels of 2276 and 1223 g/m^2, respectively (Hopkinson, Gosselink, & Parrando, 1978). A different study at Pearl River, LA shows, that the total biomasses can be very similar, values of 1150 and 900 g/m^2 for *Spartina patens* and *Spartina alterniflora*, respectively (Taylor, Grace, Guntenspergen, & Foote, 1994). Even though the levels of biomass can be very similar, the structure of the plant determines the distribution of the biomass. *Spartina alternifora* and *Spartina patens* are both erect vertically but *Spartina patens* can become matted down as seen in Figure 7.1. This means the biomass density is not only different per square meter but that the biomass is more concentrated per contained volume of the vegetation. Therefore, the biomass that the laser

footprint would encounter once reaching the surface of the vegetation is even greater for *Spartina patens*. Similar to other documented instances, it is not only the biomass per square meter or only the plant height that is determining the amount of error, but it is also the distribution of the biomass vertically. Since *Spartin alternifora* is a taller plant but *Spartina patens* is denser per contained volume, the error responses for these two species are quite similar.

The other monospecific stands surveyed in this study are Roseau cane and *Bolboschoenus robustus* at the Pearl River site. Similar to *Spartina alterniflora*, the Roseau cane structure is erect vertically but is a much taller species, reaching heights of up to 2.5 m. In the winter months, the leaves fall off, and a tall slender stalk remains. If following the general rule of thumb that error is half the vegetation height, a conservative estimate of error in this vegetation would

Figure 7.1. Image of dense matted *Spartina patens* approximately 15-20 cm above the ground surface at the Big Branch site. Photo: M. Foster-Martinez

be 1.0 m, but this is not the case. This particular species had errors ranging from 0 to 0.45 m. When applying the 5-meter minimum binning method, errors were highly reduced with a maximum error of 0.09 m in this area. This result suggests that the lidar is filtering multiple returns below the two meter mark, and extreme high canopy returns are not being used for DEM generation. Also, the high performance of minimum binning shows there is an adequate amount of laser penetration to or near the ground. The same is true for the *Bolboschoenus robustus* despite there being some large errors in the original DEM. The minimum binning was able to reduce a significant amount of the error, even though the stand was homogenous and patches did not occur.

7.1.2. Heterogeneous stands

The introduction of species mixing makes justifying error relations more difficult. This is most evident at the Big Branch site. At Big Branch, there is mixing of *Schoenoplectus americanus* and *Spartina patens*. On average, areas of higher elevation were dominated by *Spartina patens*. As elevations decreased, more *Schoeneplectus americanus* was present. At even lower elevations (<0.10 m), the vegetation became patchy, resulting in an overall decrease in biomass based on the NDVI. Within in these patchy areas, the *Spartina patens* no longer grew as a mat, but grew vertically, competing with the *Schoeneplectus americanus*. The error in these mixed areas is on average lower than the mats of *Spartina patens*, but spontaneous spots of high error still occur. Since *Schoenoplectus americanus* was never found as a homogeneous stand, it is hard to determine the root cause of the error. When using the minimum binning, errors were highly reduced, especially in the patchy areas. This result suggests that the lidar does not penetrate the mixed areas more, but rather due to the patchiness, exposed areas aid this type of DEM generation.

7.1.3. High error at low NDVIs

In this work, high DEM errors at low elevation commonly correspond with very low NDVI. The best example is demonstrated at the Big Branch survey area. There are multiple reasons for this behavior. The first cause is due to the wetness of the survey area at lower elevations. Airborne lidar systems are known to suffer from poor or null returns from certain materials such as water, asphalt, tar, clouds and fog (Finkl & Makowski, 2014). This results in fewer returns, reducing the resolution of the point cloud used for DEM generation.

The second reason is dense vegetation. Although the vegetation in these areas is scattered, the vegetation patches remain dense, preventing the lidar from fully penetrating the ground and creating a positive bias. During the TIN generation, steep large planes are then created from connecting biased wet areas with much fewer returns to points with even greater bias due to the vegetation. This results in large errors at low elevations with corresponding with low NDVIs.

7.2. Ecological Limitation of Error Solutions

A majority of published error corrections have been performed in saline marshes rather than fresh, intermediate, or brackish marshes. This is for good reason. Saline marshes in particular are usually disconnected from a freshwater source such as a river. In Louisiana, the salt marshes usually reside on the seaward side of a basin, such as in Terrebonne and Barataria Basins. These types of marshes are less prone to major fluctuations in salinity and water levels on an annual basis. Therefore, the distribution and composition of species remains relatively constant from growing season to growing season (Odum, 1988). Since there is less variability of vegetation from year to year, the temporal alignment between the lidar acquisition and imagery

is not as important. It is possible to use imagery from the growing season after acquisition versus the imagery before the growing season begins. There are also not as many vegetative species that inhabit saline marshes compared to fresh marshes (Chabreck, 1970). Less species variety means it is plausible to use high resolution imagery with limited spectral differentiation to classify land cover (Carle, Wang, & Sasser, 2014; Gallant, 2015). Further, the error distributions of the lidar with respect vegetative parameters will be less complex because of the limited number of species and species mixing. Lastly, due to the tides and salinity, biomass has a notable relation to elevation (Morris, Sundareshwar, Nietch, Kjerfve, & Cahoon, 2002). This self-organization limits the number variables needed for the adjustment of the lidar-derived DEM. This is not as easily accomplished in fresh or intermediate marshes.

More similar to fresh marshes, intermediate marshes, such as Big Branch, the systematic error due to vegetation is highly variable, temporally and spatially because plant communities are not severely limited by salinity stress (Johnson, Sasser, & Gosselink, 1985; Odum, 1988). From year to year, species distributions and compositions are likely to change because of changing water levels and salinities during the growing season. An example can be seen in Figure 7.2, which shows that the distribution of *Spartina patens* (white hues) and *Schoenoplectus americanus* (green hues) can change year to year. It should be noted that the coloration may have shifted between images due to external factors (*e.g.* illumination, sensor specifications and processing) and that vegetative changes were not confirmed in-situ. However even with this uncertainty in discriminating the vegetation, there are distinct differences. In 2015, it appears the *Spartina patens* is much more prominent, appearing homogeneously in some of the lower areas of the survey, and *Schoenoplectus americanus* is less dominant overall. This change could be driven by differing water levels during the growing season. The MWL was approximately 0.1 m

lower in 2015 than 2017. Major differences occurred during the months of May and June; the 2017 levels were 0.25-0.46 m higher. This trend is problematic when using independent data (*i.e.* NAIP 2017) at nearly a full growing season after the lidar acquisition date. It is very unlikely the spatial distribution of vegetation will remain the same, and parameters derived for correction

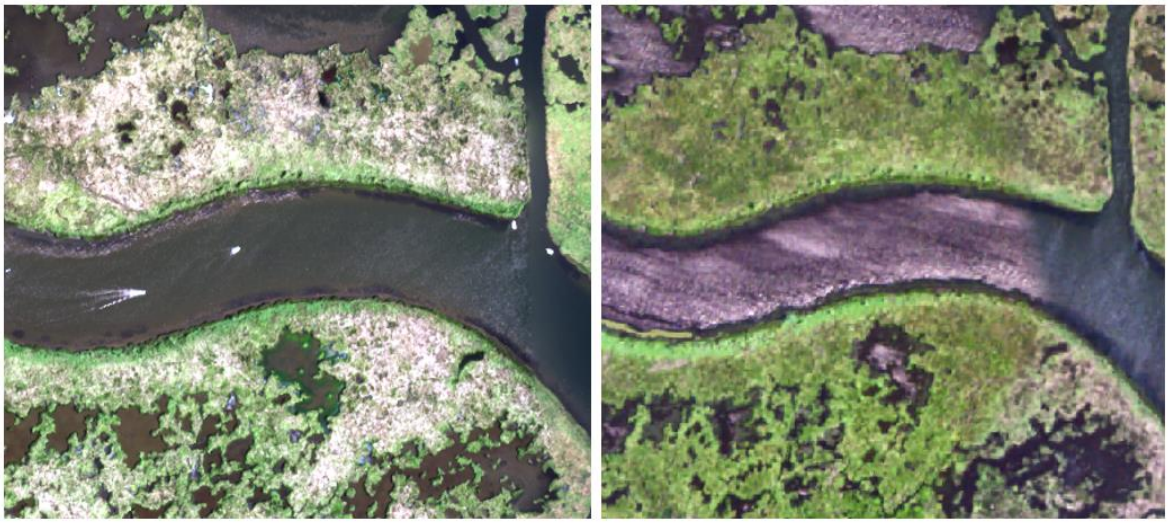

Figure 7.2. 2015(A) and 2017 (B) NAIP images of the Big Branch survey area. Both images were photographed in September.

will not be as helpful. Also, in response due to increasing sea level, many plant communities in fresh and intermediate marshes are shifting to more salt tolerant species, especially during years of less than normal precipitation (Jarrell, Kolker, Campbell, & Blum, 2016). This shift is apparent in Louisiana by examining the change in acreage for each marsh type; the salt marsh acreage has decreased due to land loss, and the intermediate and brackish marsh acreage has increased due to wetland conversion (C. Sasser et al., 2014; C. E. Sasser, Visser, Mouton, Linscombe, & Hartley, 2008; Visser, Sasser, Chabreck, & Linscombe, 1998; Visser, Sasser, Linscombe, & Chabreck, 2000).

7.3. Model Performance

A summary of all correction methods and improvements can be seen in Table 7.1. The optimal minimum binning improves the DEMs the most at the Pearl River, LA and Big Branch North sites but the resolution is sacrificed. LEAN models created at Pearl River, LA and Elmer's Survey 1 sites had the best fit to the training data, R-squared values of 0.8003 and 0.703, respectively. When models are extrapolated outside of their training data, the optimal random forest model outperforms the LEAN method and optimal minimum binning.

Table 7.1. Summary of the statistics and improvements of different methods at the survey sites. * Indicates model was trained and tested with the exact same dataset.

Method	**Stats**	Big Branch North	Big Branch South	Elmer's Survey 1	CPRA RTK	Cocodrie, LA	Pearl River, LA
Optimal Min Bin	MAE	64%	42%	40%	16%	0%	64%
	RMSE	**62%**	**21%**	**25%**	**11%**	**14%**	**65%**
	Resolution (m)	7.5	7.5	5	5	2.5	5
LEAN	**MAE**	**69% ***	**60%**	**70% ***	**33%**	**25% ***	**76% ***
	RMSE	66% *	29%	67% *	25%	33% *	73% *
	R-squared	**0.502**	**---**	**0.703**	**---**	**0.16**	**0.8003**
	Resolution (m)	1	1	1	1	1	1
Random Forest	**MAE**	**--**	**60%**	**--**	**36%**	**---**	**---**
	RMSE	--	47%	--	28%	---	---
	R-squared	**0.58**	**---**	**0.62**	**---**	**---**	**---**
	Resolution (m)	4	4	1	1	---	---

7.3.1. Big Branch South

The LEAN method was not as successful as the random forest model at Big Branch. This difference was likely caused by two reasons. First, the LEAN method relies on predictive power of different combinations of NDVI and the DEM. Since there are two species generating different error distributions at various DEM elevations, the error pattern with respect to NDVI is almost random. The timing of the imagery used in the LEAN model is also off; the imagery was taken the growing season after the lidar acquisition data. Therefore, the NDVIs may not represent the same distribution of vegetation from the previous growing season.

On the other hand, the random forest model uses LEAN variables derived from Sentinel 2 imagery from the previous growing season and uses lidar-derived metrics. These metrics are valuable information considering they are derived from very high resolution data (0.7 m) and have the exact temporal alignment of the DEM. This may be why the highest performing variable other than the DEM is the "lidar minimum." For the most part, the models perform very similar to each other between the elevations of 0.09 m - 0.4 m. The linear regression scored an R-squared value of 0.12 for the random forest model and a value 0.09 for the LEAN model with respect to RTK elevation. The largest difference between the two models are seen at the extreme positive values, where the LEAN method over predicts the error. The random forest model at Big Branch demonstrates that lidar metrics are helpful for predicting error in an intermediate marsh and are less sensitive to extreme values.

7.3.2. CPRA site

At the CPRA survey site, the LEAN model has a higher R-squared value than the random forest model within the training dataset. Suggesting the LEAN model produces a tighter fit.

However, the random forest model at the CPRA site demonstrates that the model is less sensitive to extreme values and can also fit prescribed classes as well as the LEAN model. At Elmer's Island, the random forest model proved to be not only a better predictor in Classes 3 and 5 but a better predictor across the whole dataset. The main improvements were found in class 5 and class 8 whose RMSE improved by 9% and 14%, respectively compared to LEAN. In class 8, the mean error produced was much better than the LEAN method. The LEAN method was designed to be used in saline marshes, and yet, was outperformed on all fronts by the random forest model.

It is likely the flexibility of the random forest model is what makes it a great model for this type of work. Both random forest models fared better against extreme values not seen in the training dataset. Unlike a linear regression, random forest picks the best variable of a subset of random variables for every decision node. This randomness creates hundreds of models all designed to predict error. When random forest encounters extreme inputs, such as in Class 8 of the 2013 Barataria DEM (Table 6.16), the regression has numerous models where the DEM is not the sole weight of the prediction. When all decision tree models are averaged, it is more likely the error prediction is not an extreme value, producing a less rigid result. On the other hand, when a linear model encounters an extreme variable, such as the DEM, the model is forced to use the heavily weighted DEM coefficient for the prediction. This usually results in an extreme value for DEM generation.

7.4. Model Implications

Sea level rise (SLR) has caused a migration of coastal habitats, some of which are limited by anthropogenic barriers or the necessary sediment input to survive. In this light, scientists and engineers have developed robust, expansive models to predict coastal and wetland evolution for the upcoming decades (Alizad et al., 2018; Alizad, Hagen, Morris, Medeiros, et al., 2016; Hagen,

Morris, Bacopoulos, & Weishampel, 2012). The complexity of sedimentation relationships in evolution models can range from course elevation models with uniform accretion relationships like Sea Level Affecting Marsh Model (SLAMM) to more site specific approaches like the work by Morris et al. (2002) who use biological feedback models to generate non-uniform accretion rates. Nonetheless, no matter the complexity and level of description attained, accurate initial elevations are paramount to achieve the highest quality result. The vertical elevation relative to mean sea level is considered a very important variable for classifying coastal covers and performing accretion calculations in the intertidal zone.

NOAA demonstrates the importance of accurate initial elevations by using SLAMM to predict land cover change in a coastal environment (NOAA, 2010). SLAMM is a land cover prediction model that assigns cover types based on elevation. Wetland types are categorized by minimum and maximum elevation ranges defined with water level parameters that are shifted by sea level rise for a given time step. In this study, a base 5-meter lidar DEM derived from a TIN and a 5 m minimum-bin (5-min bin) derived DEM were used as initial elevations for two different model runs projected to the year 2050. The 5-min bin derived DEM was previously proven to be less biased and had a lower RMSE than the original DEM. For comparison, land cover conversion parameters were kept constant for both model runs. The difference of the results show that salt marshes and tidal flats had the most significant errors of the cover classes. There was a -11% change of salt marsh area using the base lidar DEM and a -22% change of salt marsh area using the corrected DEM, a difference of 101%. The percent change of area covered by tidal flats increased from -6% to 54% when adjusting the DEM. The change in sign of this result suggests mud flats would be created by 2050 but were actually diminished using the unaltered DEM. For this sea-level rise scenario, the original mudflats were converted to open

water and the marshes with overestimated elevation never reached the relative water level criteria for the program to reclassify marshes as mudflats.

Other more advanced models than SLAMM, such as biomass dependent biologic feedback models or complex coupled models may be used to predict marsh evolution, but they are still sensitive to relative elevation. For example, the coupled hydrodynamic and marsh elevation model (Hydro-MEM) concurrently simulates the hydroperiod of the marsh surface driven by tides and platform topography, as well as the biological feedback of non-uniform platform accretion rates induced by Spartina alterniflora (Alizad, Hagen, Morris, Bacopoulos, et al., 2016). The addition of a hydrodynamic model to the biologic model captures the non-linear tidal responses within the marsh domain and more accurately describes the evolution of the marsh's complex topographies during long-term increases in water levels.

The marsh elevation model (MEM) component uses depth dependent organic and inorganic accretion rates to calculate total accretion at a particular location for a given time step (Morris et al., 2002). New elevations are calculated by adding an incremental increase in elevation due to accretion to the elevation value of the previous time step. This generates a new, current elevation to be used as the input for the next iteration. The incremental accretion equation is of the form:

$$\frac{dY}{dt} = (q + kB)D \qquad \text{Eq. 7.1}$$

Where dY is the increment of total accretion, dt is the time interval, q represents the rate of sediment loading, k represents the efficiency of the vegetation as a trap, B represents the productivity and D is a non-dimensional depth. In this formula, q and k are constants fitted from previous work, but B and D are variables that depend on the relative elevation of the marsh

Since, topography, water level, and bottom frictions are changing in every time step, the next iteration is updated with new tidal datums (*i.e.* mean high water and mean low water) derived from Advanced Circulation (ADCIRC) results. The datums are interpolated across the marsh surface and are used as inputs for the biomass and non-dimensional depth calculations.

A couple scenarios may occur if the elevation of the marsh platform is initially overestimated during individual time steps: 1) Areas that should be tidally inundated are modelled as dry and will have no accretion. 2) Areas that are overestimated but situated below MHW and above the hypoxia limitation will result in inorganic and organic accretion, but the incorrect rates will be used for the total accretion calculation. From the start of the model run there will be a time lag of the marsh evolution depending on the magnitude of elevation error, which is usually overestimated but will vary across the marsh surface. The initial errors will begin to compound, distorting the evolution of the marsh surface. Depending on the length of the model run and the SLR scenario used, model results will likely be skewed and misrepresent future marsh conditions.

Similar to MEM, the Wetland Accretion Rate Model For Ecosystem Resilience (WARMER) uses both biological and physical processes of vertical marsh accretion to project marsh evolution during SLR scenarios (Swanson et al., 2014). This model has been extensively used on the Pacific coast of the US in a variety of salt marshes. Using adjusted and unadjusted DEMs as model inputs, results show that 30-50% of the variations in marsh projection was due to initial elevations (Thorne, Buffington, Elliott-Fisk, & Takekawa, 2015). The variation was especially significant in marshes that were inundated with lower SLR scenarios.

As a general rule, USGS suggests that the accuracy of the initial DEM (1.96*RMSE) must be twice as large as the increment of SLR modeled (2*1.96*RMSE) to minimize the error

in the results (Gesch, 2018). With respect to the marshes in Louisiana, the smallest SLR scenario that could be modeled is 0.28 m at Cocodrie, LA. The most difficult marsh to project would be the saline marsh at Elmer's Island because of the high errors found in the DEM. Using only the marsh classes from the classified image, the smallest SLR scenario that could be accurately modeled is an increase of 0.90 m. However, if the random forest correction was applied to the marsh classes, a SLR increment of 0.59 m would provide projection results of equal confidence.

7.5. Recommendations

Choosing a method to correct DEMs depends on resolution criteria, marsh type, and available independent data. Minimum binning is best in terrain with low slope, where the canopy is sparse and some laser penetration is possible. This method is more convenient because it requires no field work to apply. However in some areas, such as the Pacific coast and Florida coast, minimum binning does not reduce a significant amount of error (Medeiros et al., 2015). On the other hand, correction methods that rely on remote sensing data are generally subjected to resolution problems, temporal mismatches or issues with independent data availability. In marshes where the vegetation is homogenous and the terrain has a low slope, such as saline marshes, high resolution and temporal matches of the independent variables is less necessary. In other marsh types, such as fresh or intermediate marshes, it is necessary to have higher resolution data, such as hyperspectral imagery with high spatial resolution to account for the high variability in spatial density and plant species. For these marsh types, it is very important that there is the proper temporal match between the independent data and the lidar acquisition date. Overall, by using independent variables with higher spatial resolutions, corrections can be applied at finer resolutions. In theory, this will produce a DEM with less stair-stepped adjustments and less smoothing of the important micro-topographies.

8. Conclusion

Fortunately, the observed errors in some of the marshes of Louisiana are lower than other published marsh errors, but they are likely to result in misleading hydrodynamic and wetland modeling outcomes. This work shows that the correction of DEMs in the marshes of coastal Louisiana is made more complex by the variety of marsh types and the temporal and spatial variability of the vegetation. It was determined that using lidar-derived metrics for correction is beneficial because this data is high resolution and temporally aligned. The temporal mismatch of high resolution independent data is a large hurdle if attempting to correct all of Louisiana's DEMs, especially in non-saline marshes. Lastly, this research shows that model corrections have better results by not limiting solutions to parametric relations but by implementing non-parametric regressions as well.

Future work may include techniques similar to Cooper et al. (2019), who use an object approach to distinguish cover patterns from multispectral drone imagery and correct error within these specified objects. If this technique has the flexibility to scale up to 1 m imagery, it would be extremely beneficial to to aquire imagery at the time of the lidar acquisition. It may be prudent to start acquiring full wave form data for DEM generation. Correcting DEMs by deriving vegetative parameters using the entire waveform can produce very accurate DEMs (Rogers et al., 2018) . In any case, these accuracies depend on the predictability of lidar encountering the biogeographical realm, making ground surface solutions merely approachable; for only in abstraction does the perfect surface exist.

References

Alizad, K., Hagen, S. C., Medeiros, S. C., Bilskie, M. V., Morris, J. T., Balthis, L., & Buckel, C. A. (2018). Dynamic responses and implications to coastal wetlands and the surrounding regions under sea level rise. *PloS one, 13*(10), e0205176.

Alizad, K., Hagen, S. C., Morris, J. T., Bacopoulos, P., Bilskie, M. V., Weishampel, J. F., & Medeiros, S. C. (2016). A coupled, two-dimensional hydrodynamic-marsh model with biological feedback. *Ecological Modelling, 327*, 29-43.

Alizad, K., Hagen, S. C., Morris, J. T., Medeiros, S. C., Bilskie, M. V., & Weishampel, J. F. (2016). Coastal wetland response to sea-level rise in a fluvial estuarine system. *Earth's Future, 4*(11), 483-497.

Allain, L. Guide to Plants of Louisiana. Retrieved from https://warcapps.usgs.gov/PlantID

Barras, J., Beville, S., Britsch, D., Hartley, S., Hawes, S., Johnston, J., . . . Porthouse, J. (2003). *Historical and projected coastal Louisiana land changes: 1978-2050*: United States Geological Survey.

Bertness, M. D., & Ellison, A. M. (1987). Determinants of Pattern in a New England Salt Marsh Plant Community. *Ecological monographs, 57*(2), 129-147. doi:doi:10.2307/1942621

Breiman, L. (2001). Random forests. *Machine learning, 45*(1), 5-32.

Buffington, K. J., Dugger, B. D., Thorne, K. M., & Takekawa, J. Y. (2016). Statistical correction of lidar-derived digital elevation models with multispectral airborne imagery in tidal marshes. *Remote Sensing of Environment, 186*, 616-625. doi:https://doi.org/10.1016/j.rse.2016.09.020

Butzeck, C., Eschenbach, A., Gröngröft, A., Hansen, K., Nolte, S., & Jensen, K. (2015). Sediment deposition and accretion rates in tidal marshes are highly variable along estuarine salinity and flooding gradients. *Estuaries and Coasts, 38*(2), 434-450.

Byrd, K. B., & Kelly, M. (2006). Salt marsh vegetation response to edaphic and topographic changes from upland sedimentation in a Pacific estuary. *Wetlands, 26*(3), 813-829.

Cahoon, D. R., & Reed, D. J. (1995). Relationships among marsh surface topography, hydroperiod, and soil accretion in a deteriorating Louisiana salt marsh. *Journal of Coastal Research*, 357-369.

Campbell, J. B. (1996). *Introduction to remote sensing*. New York: Guilford Press.

Carle, M. V., Wang, L., & Sasser, C. E. (2014). Mapping freshwater marsh species distributions using WorldView-2 high-resolution multispectral satellite imagery. *International Journal of Remote Sensing, 35*(13), 4698-4716.

CARMS, B. (2006). LiDAR—Overview of Technology, Applications, Market Features and Industry. In: Centre for Applied Remote Sensing, Modelling and Simulation, University of Victoria Victoria, BC.

Carter, J., Schmid, K., Waters, K., Betzhold, L., Hadley, B., Mataosky, R., & Halleran, J. (2012). Lidar 101: An introduction to lidar technology, data, and applications. *National Oceanic and Atmospheric Administration (NOAA) Coastal Services Center, Charleston, South Carolina, coast. noaa. gov/digitalcoast/_/pdf/lidar101. pdf. Last accessed December, 30*, 2015.

Chabreck, R. H. (1970). Marsh zones and vegetative types in the Louisiana coastal marshes.

Coco, D. S., Coker, C., Dahlke, S. R., & Clynch, J. R. (1991). Variability of GPS satellite differential group delay biases. *IEEE Transactions on Aerospace and Electronic Systems, 27*(6), 931-938.

Commitee, A. L. (2004). ASPRS Lidar Guidelines - Vertical Accuracy Reporting. Retrieved from https://www.asprs.org/a/society/committees/standards/Vertical_Accuracy_Reporting_for_Lidar_Data.pdf

Cooper, H. M. Z., Caiyun, Davis, S. E., & Troxler, T. G. (2019). Object-based correction of LiDAR DEMs using RTK-GPS dat and machine learning modeling the coastal Everglades. *Enviromental Modeling and Software*.

Couvillion, B. R., Barras, J. A., Steyer, G. D., Sleavin, W., Fischer, M., Beck, H., . . . Heckman, D. (2011). Land area change in coastal Louisiana from 1932 to 2010.

Couvillion, B. R., & Beck, H. (2013). Marsh collapse thresholds for coastal Louisiana estimated using elevation and vegetation index data. *Journal of Coastal Research, 63*(sp1), 58-67.

Datta-Barua, S., Doherty, P., Delay, S., Dehel, T., & Klobuchar, J. A. (2003). *Ionospheric scintillation effects on single and dual frequency GPS positioning.* Paper presented at the Proceedings of ION GPS/GNSS.

Duda, T., & Canty, M. (2002). Unsupervised classification of satellite imagery: choosing a good algorithm. *International Journal of Remote Sensing, 23*(11), 2193-2212.

Finkl, C. W., & Makowski, C. (2014). *Remote sensing and modeling: Advances in coastal and marine resources* (Vol. 9): Springer.

Flood, M. (2004). *ASPRS guidelines vertical accuracy reporting for LiDAR data*.

Gallant, A. L. (2015). The challenges of remote monitoring of wetlands. In: Multidisciplinary Digital Publishing Institute.

Geosystems, L. (2011). Leica ALS70 Airborne Laser Scanners. In.

Gesch, D. B. (2018). Best practices for elevation-based assessments of sea-level rise and coastal flooding exposure. *Frontiers in Earth Science, 6*, 1-19. doi:10.3389/feart.2018.00230

Gilmore, S., Saleem, A., & Dewan, A. (2015). Effectiveness of DOS (Dark-Object Subtraction) method and water index techniques to map wetlands in a rapidly urbanising megacity with Landsat 8 data. *Research@ Locate'15*, 100-108.

Hackney, C. T., Brady, S., Stemmy, L., Boris, M., Dennis, C., Hancock, T., . . . Barbee, E. (1996). Does intertidal vegetation indicate specific soil and hydrologic conditions. *Wetlands, 16*(1), 89-94.

Hagen, S. C., Morris, J. T., Bacopoulos, P., & Weishampel, J. F. (2012). Sea-level rise impact on a salt marsh system of the lower St. Johns River. *Journal of Waterway, Port, Coastal, and Ocean Engineering, 139*(2), 118-125.

Hladik, C., & Alber, M. (2012). Accuracy assessment and correction of a LIDAR-derived salt marsh digital elevation model. *Remote Sensing of Environment, 121*, 224-235.

Hopkinson, C. S., Gosselink, J. G., & Parrando, R. T. (1978). Aboveground production of seven marsh plant species in coastal Louisiana. *Ecology, 59*(4), 760-769.

Jarrell, E. R., Kolker, A. S., Campbell, C., & Blum, M. J. (2016). Brackish Marsh Plant Community Responses to Regional Precipitation and Relative sea-Level Rise. *Wetlands, 36*(4), 607-619. doi:10.1007/s13157-016-0769-0

Johnson, W., Sasser, C., & Gosselink, J. (1985). Succession of vegetation in an evolving river delta, Atchafalaya Bay, Louisiana. *The Journal of Ecology*, 973-986.

Kaplan, E., & Hegarty, C. (2005). *Understanding GPS: principles and applications*: Artech house.

Kidwell, D. M., Dietrich, J. C., Hagen, S. C., & Medeiros, S. C. (2017). An Earth's Future Special Collection: Impacts of the coastal dynamics of sea level rise on low-gradient coastal landscapes. *Earth's Future, 5*(1), 2-9.

Kim Sun, G. O., & Gibbings, P. (2005). How well does the virtual reference station (VRS) system of GPS base stations perform in comparison to conventional RTK? *Journal of Spatial Science, 50*(1), 59-73.

Kursinski, E., Hajj, G., Schofield, J., Linfield, R., & Hardy, K. R. (1997). Observing Earth's atmosphere with radio occultation measurements using the Global Positioning System. *Journal of Geophysical Research: Atmospheres, 102*(D19), 23429-23465.

Lefsky, M. A., Cohen, W. B., Parker, G. G., & Harding, D. J. (2002). Lidar Remote Sensing for Ecosystem StudiesLidar, an emerging remote sensing technology that directly measures the three-dimensional distribution of plant canopies, can accurately estimate vegetation

structural attributes and should be of particular interest to forest, landscape, and global ecologists. *BioScience, 52*(1), 19-30. doi:10.1641/0006-3568(2002)052[0019:LRSFES]2.0.CO;2

Lemmens, M. (2007). Airborne lidar sensors. *GIM international, 21*(2), 24-27.

Liaw, A., & Wiener, M. (2002). Classification and regression by randomForest. *R news, 2*(3), 18-22.

Liu, X. (2008). Airborne LiDAR for DEM generation: some critical issues. *Progress in Physical Geography, 32*(1), 31-49.

Lohani, B., & Ghosh, S. (2017). Airborne LiDAR technology: a review of data collection and processing systems. *Proceedings of the National Academy of Sciences, India Section A: Physical Sciences, 87*(4), 567-579.

Martimor, P., Arino, O., Berger, M., Biasutti, R., Carnicero, B., Del Bello, U., . . . Spoto, F. (2007). *Sentinel-2 optical high resolution mission for GMES operational services.* Paper presented at the Geoscience and Remote Sensing Symposium, 2007. IGARSS 2007. IEEE International.

McClure, A., Liu, X., Hines, E., & Ferner, M. C. (2016). Evaluation of Error Reduction Techniques on a LIDAR-Derived Salt Marsh Digital Elevation Model. *Journal of Coastal Research*, 424-433. doi:10.2112/jcoastres-d-14-00185.1

Mckee, K. L., & Patrick, W. (1988). The relationship of smooth cordgrass (Spartina alterniflora) to tidal datums: a review. *Estuaries, 11*(3), 143-151.

Medeiros, S., Hagen, S., Weishampel, J., & Angelo, J. (2015). Adjusting Lidar-Derived Digital Terrain Models in Coastal Marshes Based on Estimated Aboveground Biomass Density. *Remote Sensing, 7*(4), 3507.

Mendelssohn, I. A., McKee, K., & Patrick, W. (1981). Oxygen deficiency in Spartina alterniflora roots: metabolic adaptation to anoxia. *Science, 214*(4519), 439-441.

Mengel, M., Nauels, A., Rogelj, J., & Schleussner, C.-F. (2018). Committed sea-level rise under the Paris Agreement and the legacy of delayed mitigation action. *Nature Communications, 9*(1), 601. doi:10.1038/s41467-018-02985-8

Merzlyak, M. N., Chivkunova, O. B., Melø, T., & Naqvi, K. R. (2002). Does a leaf absorb radiation in the near infrared (780–900 nm) region? A new approach to quantifying optical reflection, absorption and transmission of leaves. *Photosynthesis Research, 72*(3), 263-270.

Mitsch, W. J., & Gosselink, J. G. (1993). Wetlands. In: Van Nostrand Reinhold.

Montané, J. M., & Torres, R. (2006). Accuracy assessment of lidar saltmarsh topographic data using RTK GPS. *Photogrammetric Engineering & Remote Sensing, 72*(8), 961-967.

Morris, J. T., Barber, D. C., Callaway, J. C., Chambers, R., Hagen, S. C., Hopkinson, C. S., . . . Troxler, T. (2016). Contributions of organic and inorganic matter to sediment volume and accretion in tidal wetlands at steady state. *Earth's Future, 4*(4), 110-121.

Morris, J. T., Sundareshwar, P., Nietch, C. T., Kjerfve, B., & Cahoon, D. R. (2002). Responses of coastal wetlands to rising sea level. *Ecology, 83*(10), 2869-2877.

NOAA. (2010). *Lidar Data Collected In Marshes: It's Error and Application for Sea Level Rise Modeling*. Retrieved from https://coast.noaa.gov/data/digitalcoast/pdf/lidar-marshes-slamm.pdf

Odum, W. E. (1988). Comparative ecology of tidal freshwater and salt marshes. *Annual review of ecology and systematics, 19*(1), 147-176.

Ogaja, C. A. (2011). *Applied GPS for engineers and project managers*.

Partners, O. (2013). *2013 USGS Lidar: Jean Lafitte and Barataria, LA*. Retrieved from NCEI: https://inport.nmfs.noaa.gov/inport/item/49766

Partners, O. (2017). *2017 USGS Lidar: Upper Delta Plain, LA*. Retrieved from NCEI: https://inport.nmfs.noaa.gov/inport/item/52981

Passeri, D. L., Hagen, S. C., Medeiros, S. C., Bilskie, M. V., Alizad, K., & Wang, D. (2015). The dynamic effects of sea level rise on low-gradient coastal landscapes: A review. *Earth's Future, 3*(6), 159-181.

Penland, S., & Ramsey, K. E. (1990). Relative sea-level rise in Louisiana and the Gulf of Mexico: 1908-1988. *Journal of Coastal Research*, 323-342.

Rogers, J. N., Parrish, C. E., Ward, L. G., & Burdick, D. M. (2018). Improving salt marsh digital elevation model accuracy with full-waveform lidar and nonparametric predictive modeling. *Estuarine, Coastal and Shelf Science, 202*, 193-211.

Rosso, P., Ustin, S., & Hastings, A. (2006). Use of lidar to study changes associated with Spartina invasion in San Francisco Bay marshes. *Remote Sensing of Environment, 100*(3), 295-306.

Sasser, C., Visser, J., Mouton, E., Linscombe, J., & Hartley, S. (2014). Vegetation Types in Coastal Louisiana in 2013 (No. SIM-3290). *United States Geological Survey*.

Sasser, C. E., Visser, J. M., Mouton, E., Linscombe, J., & Hartley, S. B. (2008). Vegetation types in coastal Louisiana in 2007. *Estuaries, 21*, 818-828.

Schmid, K. A., Hadley, B. C., & Wijekoon, N. (2011). Vertical accuracy and use of topographic LIDAR data in coastal marshes. *Journal of Coastal Research, 27*(6A), 116-132.

Shan, J., & Toth, C. K. (2018). *Topographic laser ranging and scanning: principles and processing*: CRC press.

Slaton, M. R., Raymond Hunt Jr, E., & Smith, W. K. (2001). Estimating near-infrared leaf reflectance from leaf structural characteristics. *American Journal of Botany, 88*(2), 278-284.

Swanson, K. M., Drexler, J. Z., Schoellhamer, D. H., Thorne, K. M., Casazza, M. L., Overton, C. T., . . . Takekawa, J. Y. (2014). Wetland accretion rate model of ecosystem resilience (WARMER) and its application to habitat sustainability for endangered species in the San Francisco Estuary. *Estuaries and Coasts, 37*(2), 476-492.

Taylor, K. L., Grace, J. B., Guntenspergen, G. R., & Foote, A. L. (1994). The interactive effects of herbivory and fire on an oligohaline marsh, Little Lake, Louisiana, USA. *Wetlands, 14*(2), 82-87.

Thorne, K. M., Buffington, K. J., Elliott-Fisk, D. L., & Takekawa, J. Y. (2015). Tidal marsh susceptibility to sea-level rise: Importance of local-scale models. *Journal of Fish and Wildlife Management, 6*(2), 290-304.

Trimble. (2013). Trimble R8 GNSS System Datasheet.

USGS. Earth Explorer. Retrieved from https://earthexplorer.usgs.gov/

USGS. (2016). *USGS Lidar Point Cloud LA So Terrebonne 2015*. Retrieved from United States Geological Survey:

Ussyshkin, V., & Theriault, L. (2011). Airborne lidar: advances in discrete return technology for 3D vegetation mapping. *Remote Sensing, 3*(3), 416-434.

Visser, J. M., Sasser, C. E., Chabreck, R. H., & Linscombe, R. (1998). Marsh vegetation types of the Mississippi River deltaic plain. *Estuaries, 21*(4), 818-828.

Visser, J. M., Sasser, C. E., Linscombe, R., & Chabreck, R. H. (2000). Marsh vegetation types of the Chenier Plain, Louisiana, USA. *Estuaries, 23*(3), 318-327.

Vollath, U., Buecherl, A., Landau, H., Pagels, C., & Wagner, B. (2000). *Multi-base RTK positioning using virtual reference stations.* Paper presented at the Proceedings of ION GPS.

Wang, C., Menenti, M., Stoll, M.-P., Feola, A., Belluco, E., & Marani, M. (2009). Separation of ground and low vegetation signatures in LiDAR measurements of salt-marsh environments. *IEEE Transactions on Geoscience and Remote Sensing, 47*(7), 2014-2023.

Wang, F. C., Lu, T., & Sikora, W. B. (1993). Intertidal marsh suspended sediment transport processes, Terrebonne Bay, Louisiana, USA. *Journal of Coastal Research*, 209-220.

Webster, T. L., & Dias, G. (2006). An automated GIS procedure for comparing GPS and proximal LiDAR elevations. *Computers & Geosciences, 32*(6), 713-726.

Wuebbles, D. J., Fahey, D. W., & Hibbard, K. A. (2017). Climate science special report: fourth national climate assessment, volume I.

Zedler, J. B., & Kercher, S. (2005). Wetland resources: status, trends, ecosystem services, and restorability. *Annu. Rev. Environ. Resour., 30*, 39-74.

VITA

Ryan Lauve was raised on a family rice farm in Woodworth, Louisiana. He spent a majority of his childhood concurrently daydreaming, fishing or exploring the wilderness with his dog. He graduated from Alexandria Senior High in 2011 and enrolled at LSU to later complete a Bachelor of Science degree in Petroleum Engineering. Detached from his roots and taunted by a nihilistic outlook, he decided to apply for the Coastal and Ecological Engineering Master's program. After a long three years and much knowledge gained he plans to graduate spring of 2019. He has experience in topographic surveying and remote sensing and understands the benefits and services ecological systems can provide. He has no plans for the immediate future, and that's fine by him.